Damping loss factor characterization of complex structures using correlation method

Muhammad Najib Bin Fazail

Par **Muhammad Najib BIN FAZAIL**

Caractérisation de l'amortissement des structures complexes par la méthode de corrélation

Thèse présentée en cotutelle
pour l'obtention du grade
de Docteur de l'UTC

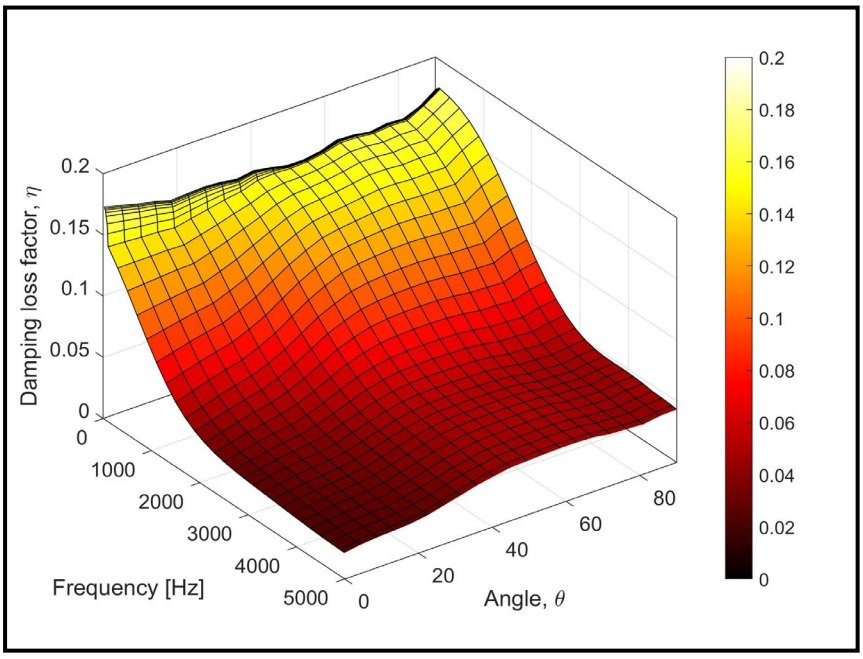

Soutenue le 16 janvier 2023
Spécialité : Acoustique et Vibrations : Unité de recherche en Mécanique - Laboratoire Roberval

D2718

THÈSE DE DOCTORAT

en co-totutelle entre

l'**Université de Technologie de Compiègne (UTC), France**
Laboratoire Roberval
Mécanique, énergie et électricité

et

l'**Université de Sherbrooke (UDS), Québec, Canada**
Faculté de génie
Département de génie mécanique

pour obtenir le grade de Docteur

par Muhammad Najib BIN FAZAIL

Spécialité : Acoustique et Vibrations

Caractérisation de l'amortissement des structures complexes par la méthode de corrélation

Soutenue le 16 janvier 2023

Membres du jury UTC :

Mohamed ICHCHOU, Professeur, École Centrale Lyon, France	Rapporteur
Kerem EGE, Maître de conférences, HDR, INSA Lyon, France	Rapporteur
Stéphane MOREAU, Professeur, Univ. de Sherbrooke, Canada	Examinateur
Emeline SADOULET-REBOUL, Maître de conférences, HDR, Univ. de Franche-Comté, France	Examinatrice
Charles PÉZERAT, Professeur, Univ. du Maine, France	Examinateur
Nicolas DAUCHEZ, Professeur, Univ. de Technologie de Compiègne, France	Examinateur
Jean-Daniel CHAZOT, Maître de conférences, HDR, Univ. de Technologie de Compiègne, France	co-directeur
Noureddine ATALLA, Professeur, Univ. de Sherbrooke, Canada	co-directeur
Gautier LEFEBVRE, Maître de conférences, Univ. de Technologie de Compiègne, France	invité

Damping loss factor characterization of complex structures using correlation method

Muhammad Najib BIN FAZAIL

Defended on January 16, 2023

Résumé

Le travail de thèse porte sur la caractérisation de l'amortissement des structures complexes par la méthode de corrélation. Dans le premier chapitre, un état de l'art rassemblant de nombreuses méthodes de caractérisations locales et globales est présenté. Dans la deuxième partie du chapitre, les méthodes de mesures expérimentales de l'amortissement et un modèle analytique de référence sont abordés.

Dans le deuxième chapitre, la methode Inhomogeneous Wave Correlation (IWC) qui calcule la corrélation entre le champ de déplacement mesuré et une onde plane inhomogène est revisitée. Une nouvelle variante qui considère la décroissance exponentielle avec la distance du point d'excitation dans la formulation d'onde inhomogène est introduite. L'introduction de cette variante a pour but d'améliorer l'estimation de l'amortissement. La validité de la méthode proposée est étudiée numériquement sur des structures planes avec différents degrés de complexité. Les performances de la méthode en fonction la position du point d'excitation et de la taille de la fenêtre d'observation sont également étudiées.

Un nouveau modèle de corrélation basé sur la fonction de Green permettant d'estimer les paramètres élastiques équivalents des structures complexes en fonction de l'angle de propagation est détaillé dans le troisième chapitre. Contrairement à la méthode IWC mentionnée ci-dessus, le champ de déplacement mesuré est désormais corrélé avec un modèle basé sur la fonction de Green. Cette dernière est plus adaptée pour décrire le champ proche du point d'excitation et offre plus de stabilité sur l'estimation de l'amortissement comparée aux méthodes précédentes. Plusieurs résultats, avec des données simulées et mesurées, sont comparés au modèle analytique et montrent la précision de cette technique pour estimer précisément l'amortissement des structures complexes en fonction de la fréquence et de l'angle de propagation des ondes. Dans la deuxième partie du chapitre, la performance de la méthode sur l'estimation de l'amortissement en fonction des différents points d'excitation est également étudiée et un filtre angulaire spatial est introduit pour améliorer le résultat.

Dans le quatrième chapitre, la méthode des sources images qui a pour objectif d'améliorer l'estimation de l'amortissement en basses fréquences des structures faiblement amorties est introduite. Cette approche prend en compte les réflexions des ondes de flexion aux frontières. La performance de la méthode est étudiée sur deux types de conditions limites : bords simplement appuyés et bords libres. Le résultat est comparé à la méthode introduite dans le troisième chapitre ainsi qu'au modèle analytique GLM.

Mots-clés: amortissement, méthode de corrélation, fonction de Green, méthode des sources images, nombre d'onde

Abstract

The thesis presents inverse correlation techniques able to measure accurately the damping loss factor of complex plane structures. In the first chapter, the state of the art gathering numerous local and global characterization methods is presented. In the second part of the chapter, various topics of direct interest to the thesis such as classical damping loss factor measurement techniques and the analytical solution based on the discrete general laminate model (GLM) are briefly discussed.

In the second chapter, the inhomogeneous wave correlation (IWC) method based on the maximization of the correlation between an inhomogeneous wave and the measured displacement field as a function of the wave heading angle is revisited. A new variant that considers the exponential decay with distance from the excitation point in the inhomogeneous wave formulation is introduced. The purpose of introducing this variant is to improve the estimation of the damping loss factor. The validity of the proposed method is investigated numerically on flat thin structures and sandwich damped structures. The performance of the method related to the excitation point location and the size of the observation window are also investigated.

A new Green's function-based model correlation (GFC) method able to estimate the equivalent elastic parameters of complex structures at different propagation angles is detailed in the third chapter. Contrary to the IWC method, the measured displacement field is correlated with a Green's function-based model. This approach is more adapted to describe the field near the excitation point and offers more stability in estimating the damping loss factor compared to previous methods. Several results, with simulated and measured data, are compared with an analytical discrete laminate model and show the accuracy of this technique to recover the damping loss factor of complex structures as function of the frequency and the heading angle. In the second part of the chapter, the impact of different excitation location on the estimation of the wavenumber and the damping loss factor is investigated. A spatial angular filter to rectify the estimation of the damping loss factor is introduced.

In the fourth chapter, the image source method with an objective of improving the previous GFC method in the low frequency range and for lightly damped structures is introduced. The proposed method takes into account the reflection at boundaries which is ignored in the free field Green's function used in the previous chapter. The performance of the method is investigated for two types of boundary conditions: simply supported and free edges. The identified parameters of the numerical simulations are compared to the previous GFC method and to the analytical discrete laminate model.

Keywords: damping, inverse method, viscoelastic, Green's function, image source method, wavenumber

Acknowledgements

I would like to express my deepest gratitude to my supervisors, Jean-Daniel Chazot, Noureddine Atalla and Gautier Lefebvre for the continuous guidance, scientifically and humanly, throughout the PhD project. I have benefited greatly from your knowledge and sharing.

I would like to thank the Hauts-de-France Region, the Natural Sciences and Engineering Research Council of Canada (NSERC) and the Consortium for Aerospace Research and Innovation of Québec (CRIAQ) for their financial support.

Thank you to my dear colleagues at Université de Technologie de Compiègne: Christophe Langlois, Alexandre Berthet, Youcef Medelfef, Yackine Tadjou, Amine Benamar, Fares Naccache, Cyril Calmettes, Carlos Garcia, Yorick Buot De l'Epine, Li Ke, Alexandre Wilkinson, Grégoire Markey, Matthieu Duroyon, Simon Rampnoux, Camille Leblanc and Silouane De Reboul for sharing these years together. Thank you as well to Nicolas Dauchez, Mabrouk Ben Tahar, Solène Moreau, Emmanuel Perrey-Debain, Valérie Duquenne, Nathalie Barrast and all the members of Laboratoire Roberval.

Thank you to my dear colleagues at Université de Sherbrooke: Xukun Feng, Wafaa El Khatiri, Oumayma Othmen, Dongze Cui and all the members of the Groupe Acoustique Université de Sherbrooke (GAUS) for sharing these years together.

My sincere thanks go to all the people that I've met during these years especially at Université de Technologie de Compiègne and Université de Sherbrooke.

I wish to extend my special thanks to my parents, Che Gayah and Fazail, and my siblings, Nabilah, Nasyrah and Idham for supporting me with every means throughout these years.

Finally, to my wife: Amira, thank you for always being there through my ups and downs. I am blessed to share this moment with you and I am grateful for your unconditional, unequivocal and loving support.

Contents

Introduction

Context

Companies are creating new technological solutions to satisfy client demands and, on the other hand, to respect the rules established by the local and global authorities on noise pollution. The creation of complex structures like sandwich and composite panels is crucial to meet these requirements.

Most industries, including the aviation business, the building industry, the automotive industry, the railroad industry, and the armaments industry, use these materials. For instance, the aircraft body in the aviation sector is roughly 50% constructed of composite materials, as shown in Fig. 1. These materials make it possible to reduce body weight, which in turn lowers fuel consumption. However, the usage of these materials significantly impacts the acoustic performance of the aircraft. As a result, numerous studies have been carried out to improve the design of the structure to overcome this limitation, with the objective of increasing passenger comfort.

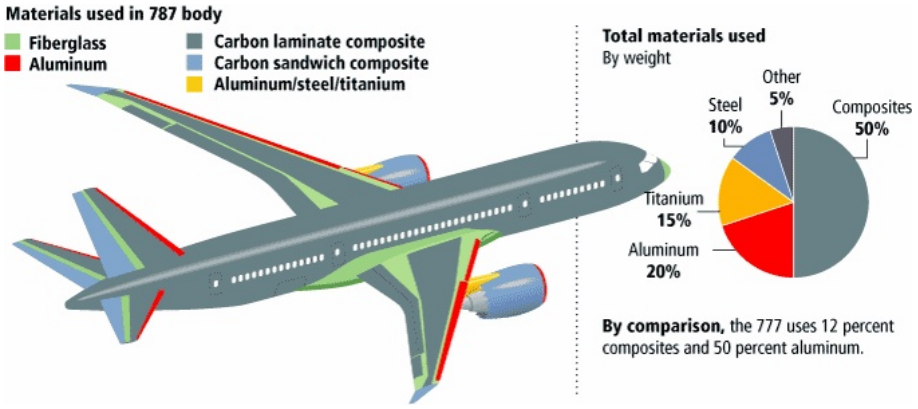

Figure 1: Usage of various materials in the Boeing 787 [44].

In the construction sector, the use of thick concrete is no longer privileged in the economic point of view due to the weight of the wall that is proportional to the acoustic performance. The usage of curtain wall or in french *mur-rideau* is more often adopted because this wall can achieve similar or even superior performance acoustically and thermally compared to the conventional materials with reduced thickness and cost.

Sandwich and composite materials are very practical because of their lightness and their flexible mechanical properties compared to classical homogeneous materials. An illustration of a sandwich with a lightweight thick honeycomb core and two thick stiff skins is shown in Fig. 2. The anisotropic behavior of the panel makes it very challenging to develop a robust predictive model.

The windshield of a car made up of glass skins and a viscoelastic core is another

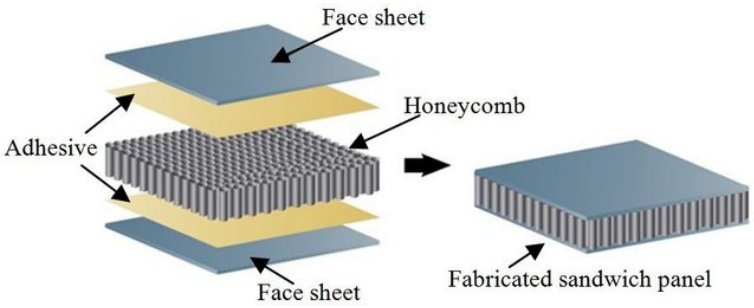

Figure 2: Illustration of a sandwich with a honeycomb core panel [64].

example of complex structures. The frequency dependent behavior of the viscoelastic core makes the estimation of equivalent material properties and in particular, the damping loss factor very difficult.

Numerous characterization methods have been developed throughout the years to feed numerical models with accurate input data. However, a robust method able to estimate the damping loss factor remains an open issue. In this context, the main focus of the thesis is to develop a robust predictive model able to characterize the damping loss factor of these structures.

Research objectives

The flowchart of the inverse characterization method is shown in Fig. 3. The normal displacement field is considered as an input. The scope of the thesis is to develop a model predicting accurately the wavenumber and in particular, the damping loss factor as a function of the frequency and the wave propagating angle of complex structures via correlation technique.

The wavenumber k can be defined as the number of complete wave cycles per unit length: $k = 2\pi/\lambda$, where λ represents the wavelength. The wavenumber is usually expressed in a complex form, with the imaginary part containing information about the attenuation per unit distance and can be related to the damping loss factor. Accurate estimation of these two fundamental parameters is extremely useful for predicting the acoustic performance of a structure.

To reach this objective, the advantages and the drawbacks of precedent works are investigated. Amongst the existing tools are the modal analysis, the McDaniel's approach, the discrete Fourier transform, Force Analysis Technique (FAT), the Inhomogeneous Wave Correlation (IWC) method and the Green's function correlation method.

In the low frequency range, the modal analysis is widely used to characterize the material properties. In the mid and the high frequency range, this approach is no longer applicable due to the high modal density and the high modal overlap of the vibrating structure. The McDaniel's approach based on the plane wave propagation allows the characterization of one-dimensional structures in narrow frequency bands. The discrete spatial Fourier Transform (DFT) has also been used widely to determine the wavenumber of two dimensional structures. The rapidity of the method presents major advantages but

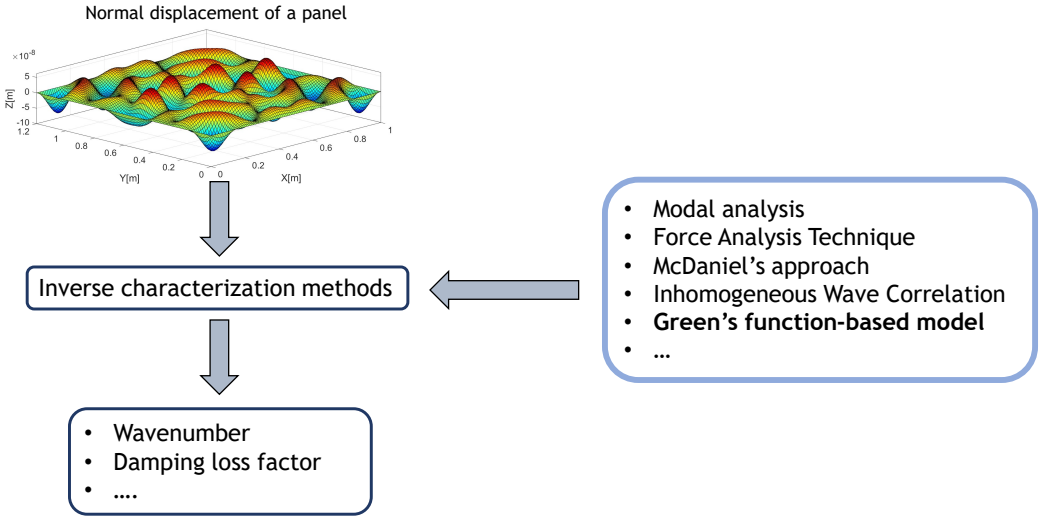

Figure 3: Flowchart of the characterization process.

is limited to equally spaced measurement points and is not able to estimate the damping loss factor.

The inhomogeneous wave correlation (IWC) method is the extension of the McDaniel's approach to two dimensional structures. This approach is based on the maximization of the correlation between an inhomogeneous wave and the spatial field as a function of the wave heading angle. However, the IWC method is based on the plane wave hypothesis and is limited due to the nature of the plane wave itself. Indeed, the vibrational field near the excitation point cannot be compared with a plane wave. Therefore the measurements must be done over an observation area sufficiently far from the excitation point. In reality, this condition is difficult to obtain due to the finite dimensions of the panel.

Another wave fitting approach based on the Green's function which is more adapted to describe the vibrational field near the excitation point has been developed recently. This method has been successfully applied to isotropic structures and to orthotropic elliptic structures. To our knowledge, this method has never been applied to anisotropic structures.

Our first objective is to revisit the IWC method and introduce a new variant to improve the estimation of the damping loss factor. The second objective is to develop a new Green's function correlation method able to estimate the damping loss factor of anisotropic structures as a function of the frequency and the wave propagating angle. The third objective is to develop a method overcoming the limitations of the free field Green's function and improving the estimation of the damping loss factor for lightly damped structures and for the low frequency range.

Outlines

The thesis is divided into four chapters. In the first chapter, the state of the art gathering numerous local and global characterization methods is presented. The advantages and limitations of each methods are presented. Classical experimental damping loss factor measurement methods such as the 3dB method, the power input method and the decay rate method are also presented in this chapter. Finally, the analytical solution based on discrete general laminate model (GLM) [36] used as a reference for validation of the estimated wavenumber and damping is briefly discussed.

The second chapter introduces a new variant of the inhomogeneous wave correlation(IWC) method. This method is based on the maximization of the correlation function between the measured displacement field and the inhomogeneous plane wave. The new variant of the method that explicitly accounts the exponential decay of the wave amplitude with the distance from the source is introduced. The validity of the proposed method is investigated numerically on aluminium isotropic panel and anisotropic 7 layers epoxy resin panel. The effect of the excitation point position and the size of the observation window are also studied.

A new Green's function-based model correlation (GFC) able to estimate the equivalent elastic parameters of complex structures at different propagation angles is detailed in the third chapter. Contrary to the IWC method, the measured displacement field is correlated with a Green's function-based model. This approach is more adapted to describe the field near the excitation point. This technique offers more stability and reduces computation time in estimating the damping loss factor compared to previous methods. The validity of the proposed method is investigated numerically using the Finite Element Method (FEM) on several sandwich panels and is tested experimentally on a non-isotropic thick sandwich composite panel with a honeycomb core. The identified parameters of the numerical simulations are compared to an analytical discrete general laminate model (GLM). The experimental damping loss factor estimation is compared with reference methods such as the power input method, the 3dB method and the decay rate method.

In the fourth chapter, the image source method is explored. Compared to the previous method, this approach takes into account the reflection at boundaries of the panels. Combining this method with GFC improves the estimation of the damping loss factor for low damping structures and for the low frequency range. The identified parameters of the numerical simulations are compared to the previous GFC method and to the GLM.

Chapter I

Literature review and state of the art

I.1 Introduction

In the domain of transportation industry, noise control requires robust simulation tools to predict the vibratory and acoustic levels inside and outside vehicles such as airplanes, cars and trains. Numerous global [21, 86, 41, 42, 43, 7, 59, 60] and local [71, 72, 1, 57, 76, 5] characterization methods have been developed throughout the years to feed the numerical models with accurate input data.

One of the local approaches that has been widely used is the Force Analysis Technique (FAT) [71, 72, 70, 1, 2, 57]. This method uses the equation of motion and a spatial finite different scheme to estimate the elastic parameters. The Corrected Force Analysis Technique (CFAT) [49, 48, 58, 55] extends the method to reduce the bias error of the finite different scheme by adding correction factors. The main advantage of this method is the ability to be applied without any knowledge outside of the studied area such as the boundary conditions or sources. However, this method is sensitive to measurement uncertainties due to the fourth-order derivatives of the measured deflections of the finite difference scheme.

On the other hand, the global wave fitting approach which is less sensitive to measurement uncertainties is adopted in this thesis. More often, the measured displacement field is fitted with an inhomogeneous wave. McDaniel et al. [61, 62] applied the wave fitting method to estimate the flexural wavenumber and the damping loss factor of one dimensional structures. This approach is based on the error minimisation between a wave model and the measured responses.

The discrete spatial Fourier Transform (DFT) [50, 42, 33] has also been widely used to determine the wavenumber of two dimensional structures. The rapidity of the method using the fast Fourier transform algorithm presents a major advantage but is limited to equally spaced measurement points and is not able to estimate the damping loss factor.

The Inhomogeneous Wave Correlation (IWC) developed by Berthaut et al. [7] extends the McDaniel method for two-dimensional structures and the DFT method for the identification of the damping loss factor. This approach is based on the maximization of the correlation between an inhomogeneous wave and the spatial field as a function of the wave heading angle. The method has been applied to one-dimensional structures [73, 45], two-dimensional sandwich structures with honeycomb cores [41], stiffened panels [42, 43] and panels with distributed resonators [87].

Cherif et al. [21] applied the IWC method to estimate the damping loss factor of orthotropic structures using an iterative refinement process. Tufano et al. [86] applied this approach to curved structures with resonators. However, the IWC method which is based on the plane wave hypothesis is limited due to the nature of the plane wave itself. Indeed, the vibrational field near the excitation point cannot be compared with a plane wave. Therefore the measurements must be done over an observation area sufficiently far from the excitation point. In reality, this condition is difficult to obtain due to the finite dimensions of the panel.

To overcome this last limitation, Tufano [83] replaced the inhomogeneous wave function by the Green's function of the isotropic infinite plate. This method combines advantages of the IWC and the Green's function. Compared to the IWC method, the Green's

function is more adapted to describe the vibrational field near the excitation point. Tufano applied this method to isotropic laminated plate and isotropic homogeneous plate with tuned mass damper (TMD).

Another wave fitting approach has been introduced by Cuenca et al. [27, 26, 28]. In this approach, the harmonic displacement field model is constructed by using a linear combination of the Green's function of an infinite plate and its image sources, which represent the successive reflections of waves on the boundaries [27]. This model is then fitted with the measured displacement field to estimate the material properties. Roozen et al. [75] applied the method experimentally to estimate the wavenumber and the damping loss factor of a thin isotropic plate by adding a Bayesian regularisation to increase the accuracy of the method. Recently, Marchetti et al. [57] extended the method to characterize elliptical orthotropic structures based on the analytical expression developed by Berthaut [6] in the appendix of his thesis.

This chapter represents a general overview of these methods with a brief discussion of their advantages and limitations. In the second part, various topics of direct interest to this thesis will be briefly discussed. In Section I. 4, classical methods such as the 3dB method, the decay rate method, the power input method and the spatial damping loss factor are presented. Then, the image source method is presented in Section I. 6. Finally as the discrete general laminate model (GLM) [36] will be used throughout this thesis as a reference for validation of the estimated wavenumber and damping, a brief description will be given in Section I. 7.

I. 2 Local characterization method: Force Analysis Technique

The Force Analysis Technique (FAT) also known in French as *Résolution Inverse Filtrée Fenêtrée* (RIFF) has been developed first by Pézerat and Guyader for localization of external sources on a beam [71] and on a panel [72] and has been adapted to estimate other elastic parameters such as the Young's modulus and the damping loss factor. This method is based on the estimation of the equation of motion by means of a finite difference scheme.

The principle of the method is detailed here through the example of determining the Young's modulus E and the damping loss factor η of a thin isotropic panel [1]. The equation of motion of an isotropic panel within an area without external force (i.e., $f(x,y)=0$) is written as:

$$\frac{D}{\rho h\omega^2}\left(\frac{\partial^4 w}{\partial x^4}+2\frac{\partial^4 w}{\partial x^2\partial y^2}+\frac{\partial^4 w}{\partial y^4}\right)=w(x,y) \quad , \tag{I.1}$$

where D is the bending stiffness, ρ is the mass density, h is the thickness and $w(x,y)$ is the displacement. The complex bending stiffness writes:

$$D=\frac{E(1+\mathrm{i}\eta)h^3}{12(1-\nu^2)} \quad , \tag{I.2}$$

with $E(1+\mathrm{i}\eta)$ the complex Young's modulus, η the loss factor and ν the Poisson's coefficient. Eq. I.1 expresses the fact that the bilaplacian $\nabla^4 w(x,y)$ equals the displacement $w(x,y)$ up to a constant multiplier [1]. Assuming that the displacement $w(x,y)$ is known, the quantity $D/\rho h$ is quantifiable at any frequency without any knowledge of the location and the amplitude of the force and the boundary conditions.

In reality, the displacement at any location is easily measured by using an accelerometer or laser vibrometer but the fourth-order partial derivatives in Eq. I.1 is not direct. To overcome this difficulty, the displacement $w_{i,j}$ can be measured at discrete abscissas (x_i,y_i) over a regular mesh grid in order to approximate the partial derivatives using a finite difference scheme. The discretization of the equation of motion using finite difference scheme writes:

$$\frac{D}{\rho h\omega^2}\left(\delta_{i,j}^{4x}+2\delta_{i,j}^{2x2y}+\delta_{i,j}^{4y}\right)=w_{i,j} \quad , \tag{I.3}$$

where $\delta_{i,j}^{4x}$, $\delta_{i,j}^{2x2y}$ and $\delta_{i,j}^{4y}$ are the fourth-order partial derivatives of the displacement field. These derivatives write:

$$\frac{\partial^4 w}{\partial x^4}\approx\delta_{i,j}^{4x}=\frac{1}{\Delta_x^4}\left(w_{i+2,j}-4w_{i+1,j}+6w_{i,j}-4w_{i-1,j}+w_{i-2,j}\right) \quad , \tag{I.4}$$

$$\frac{\partial^4 w}{\partial y^4}\approx\delta_{i,j}^{4y}=\frac{1}{\Delta_y^4}\left(w_{i,j+2}-4w_{i,j+1}+6w_{i,j}-4w_{i,j-1}+w_{i,j-2}\right) \quad , \tag{I.5}$$

$$\frac{\partial^4 w}{\partial x^2 \partial y^2} \approx \delta_{i,j}^{2x2y} = \frac{1}{\Delta_x^2 \Delta_y^2}(w_{i+1,j+1} - 2w_{i+1,j} + w_{i+1,j-1} - 2w_{i,j+1} + 4w_{i,j} - 2w_{i,j-1} + w_{i-1,j+1} - 2w_{i-1,j} + w_{i-1,j-1}) \quad . \tag{I.6}$$

The identification of the loss factor η and the Young's modulus E can then be performed. First, the displacement field $w_{i,j}$ is measured or simulated. Then, the discrete bilaplacian $\nabla_{i,j}^4 = \delta_{i,j}^{4x} + \delta_{i,j}^{2x2y} + \delta_{i,j}^{4y}$ is calculated with the finite difference scheme and Eq. I.7 is solved in a least square sense.

$$\begin{bmatrix} \delta_1^{4x} + 2\delta_1^{2x2y} + \delta_1^{4y} \\ \vdots \\ \delta_N^{4x} + 2\delta_N^{2x2y} + \delta_N^{4y} \end{bmatrix} \frac{D}{\rho h \omega^2} = \begin{bmatrix} w_1 \\ \vdots \\ w_N \end{bmatrix} \quad . \tag{I.7}$$

The method has been applied numerically to a simply supported isotropic thin plate (Length $L_x = 0.5$ m, width $L_y = 0.4$ m, thickness $h = 5$ mm, density $\rho = 1500$ kg/m^3, Poisson's ratio $\nu = 0.3$, Young's modulus $E = 5$ GPa and loss factor $\eta = 0.05$). The geometry and the observation area of the simulation is shown in Fig. I.1.

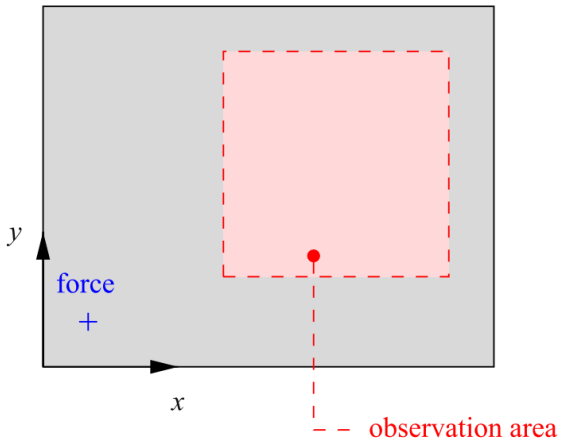

Figure I.1: Geometry of the panel used for numerical simulation [1].

The method predicts precisely the Young's modulus and the damping loss factor from an exact displacement field without noise as shown in Fig. I.2a-b respectively. However when the noise is added (Signal to noise ratio (SNR) = 40dB), the identification of the Young's modulus and the damping properties become erroneous.

In fact, the finite difference scheme is very sensitive to the noise. In order to overcome this limitation, each field is windowed by a bi-dimensional Tukey window $\Psi_{i,j}^{2D}$ to replace the truncation of the field at the edges by a smooth variation from zero amplitude.

The windowed field is then convoluted by the finite spatial response $h_{i,j}$ of a low-pass filter with cut-off wavenumber $k_c = \alpha k_f$, where k_f corresponds to the natural wavenumber and the coefficient α is chosen between 1 and 4 depending on the signal-to-noise ratio [1]. The complete expression of the Tukey window and the wavenumber filter can be obtained in [1, 49, 48]. The summary of the procedure is shown in Fig. I.3.

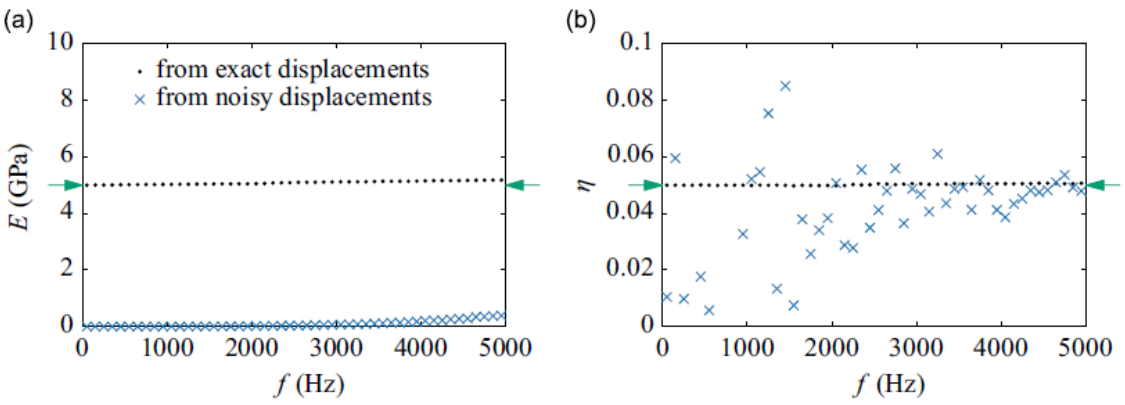

Figure I.2: Estimation of the Young's modulus and the loss factor from the exact displacement field and the noisy displacement field. (a) Young's modulus E and (b) loss factor η. The arrows shows the input values of E and η [1].

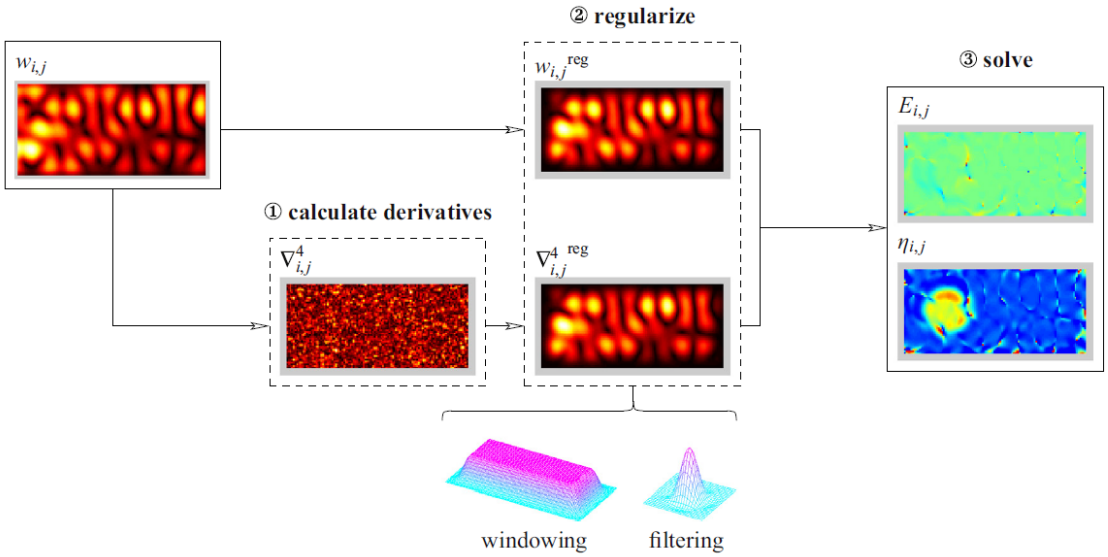

Figure I.3: Procedure to identify the properties of the structure. The derivatives $\nabla^4_{i,j}$ is determined from the displacement field $w_{i,j}$. Both fields are then regularized and solved based on the wanted criteria [1].

The results in Figs. I.4a-b show the identification of the Young's modulus and the damping loss factor after being windowed and filtered. The Young's modulus is well identified in Fig. I.4a and the relative error is almost the same for all the noise levels. However, the relative error on loss factor is highly dependent on the level of noise especially in the low frequency range [1].

The Force Analysis Technique has been extensively developed to determine material properties of a Timoshenko beam [90], an isotropic plate [1, 30], an orthotropic plate [2] and an anisotropic plate [58]. However, this local method is sensitive to measurement uncertainties due to the fourth-order derivatives of the measured deflections. A careful definition of the regularization (windowing + filtering) is needed to estimate accurately the material properties.

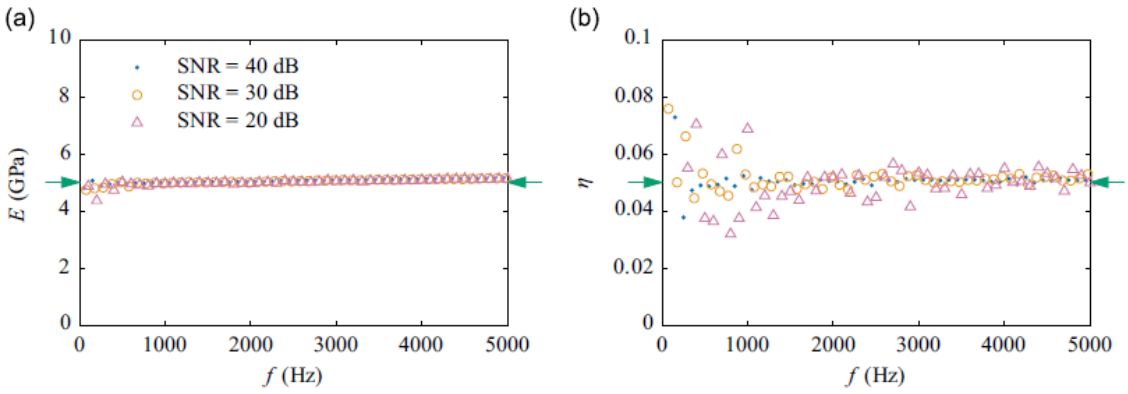

Figure I.4: (a) Young's modulus E and (b) loss factor η estimated from windowed and filtered signal [1].

I. 3 Global characterization methods

I. 3. 1 McDaniel's approach

McDaniel et al. [61, 62] presented a method estimating the complex wavenumbers of one dimensional structures. This approach is based on a nonlinear optimization algorithm that minimizes the error between the measured response and the wave model by adjusting the complex wavenumbers and amplitudes.

The principle of the method is detailed in this section. The solution of the homogeneous equation of a beam is defined as [62]:

$$Y_w(x,\omega) = c_1(\omega)e^{\mathrm{i}kx} + c_2(\omega)e^{-\mathrm{i}kx} + c_3(\omega)e^{kx} + c_4(\omega)e^{-kx} \quad , \tag{I.8}$$

where $Y_w(x,\omega)$ is the measured displacement field and $c_n(\omega)$ are the constants depending on the boundary conditions and k is the wavenumber. The wavenumber of a beam k is defined as:

$$k = \sqrt[4]{\frac{\rho A \omega^2}{E(\omega)(1-\mathrm{i}\eta(\omega))I}} \quad , \tag{I.9}$$

where ρ is the mass density, A is the cross-sectional area, I is the area moment of inertia, E is the Young's modulus and η is the damping loss factor. The method has been applied experimentally by placing accelerometers along the beam for each measurement points $\{x_1, x_2, x_3, ..., x_n\}$. Eq. I.8 can then be defined in the matrices form:

$$\begin{bmatrix} Y_{\mathrm{w}}(x_1,\omega) \\ Y_{\mathrm{w}}(x_2,\omega) \\ \vdots \\ Y_{\mathrm{w}}(x_n,\omega) \end{bmatrix} = \begin{bmatrix} \mathrm{e}^{\mathrm{i}kx_1} & \mathrm{e}^{\mathrm{i}kx_1} & \mathrm{e}^{-kx_1} & \mathrm{e}^{-kx_1} \\ \mathrm{e}^{\mathrm{i}kx_2} & \mathrm{e}^{-\mathrm{i}kx_2} & \mathrm{e}^{kx_2} & \mathrm{e}^{-kx_2} \\ \vdots & \vdots & \vdots & \vdots \\ \mathrm{e}^{\mathrm{i}kx_n} & \mathrm{e}^{-\mathrm{i}kx_n} & \mathrm{e}^{kx_n} & \mathrm{e}^{-kx_n} \end{bmatrix} \begin{bmatrix} c_1(\omega) \\ c_2(\omega) \\ c_3(\omega) \\ c_4(\omega) \end{bmatrix} . \tag{I.10}$$

The complex wavenumber, $k(\omega) = k_R(\omega) + \mathrm{i}k_I(\omega)$ and the amplitudes $c_1(\omega)$, $c_2(\omega)$,

$c_3(\omega)$ and $c_4(\omega)$ can be estimated using a non-linear optimization algorithm [62]. In this particular case, the normalized square, ε, is defined by:

$$\varepsilon = \sqrt{\left(\sum_{i=1}^{n} \left|Y_w(x_i,\omega) - Y_a(x_i,\omega)\right|^2\right) / \left(\sum_{i=1}^{n} \left|Y_a(x_i,\omega)\right|^2\right)} \quad , \tag{I.11}$$

where $Y_a(x_i,\omega)$ is the actual displacement field. Given the values of $k(\omega)$ that minimize the error, the damping loss factor can be estimated by the following relation [24]:

$$\eta(\omega) = \left|\frac{\mathrm{Im}(k)^4}{\mathrm{Re}(k)^4}\right| \quad . \tag{I.12}$$

The proposed method was applied to a beam and compared to the analytical solution. The real part of normalized wavenumber and normalized frequency is shown in Fig. I.5 and the estimated loss factor is represented in Fig. (I.6). A good correlation between the estimated values and the actual values demonstrates the robustness of the method.

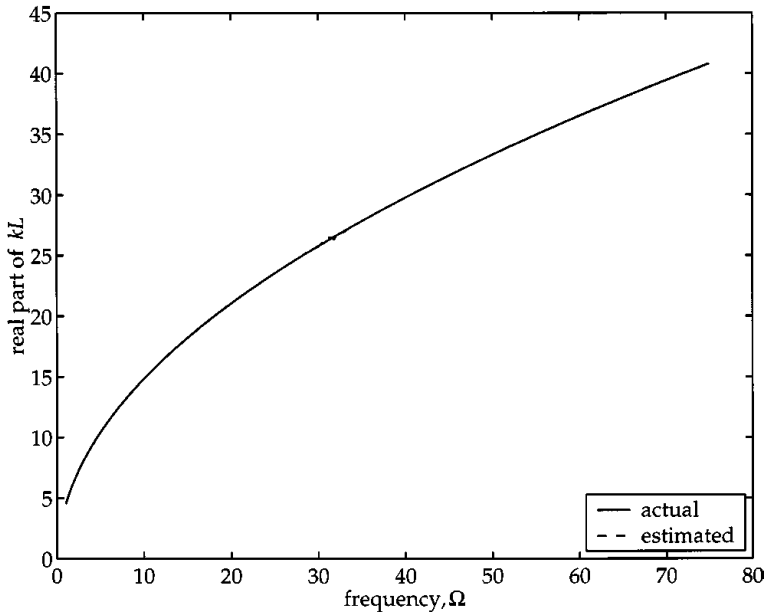

Figure I.5: Real part of the normalized wavenumber and the normalized frequency [62].

The global wave approach method introduced by McDaniel shows a good approximation of the dispersion relation and the damping loss factor from a small number of measured response amplitudes. The absence of any hypotheses about the boundary conditions and the material properties represent major advantages of the method. However, this method is limited to one dimensional structures.

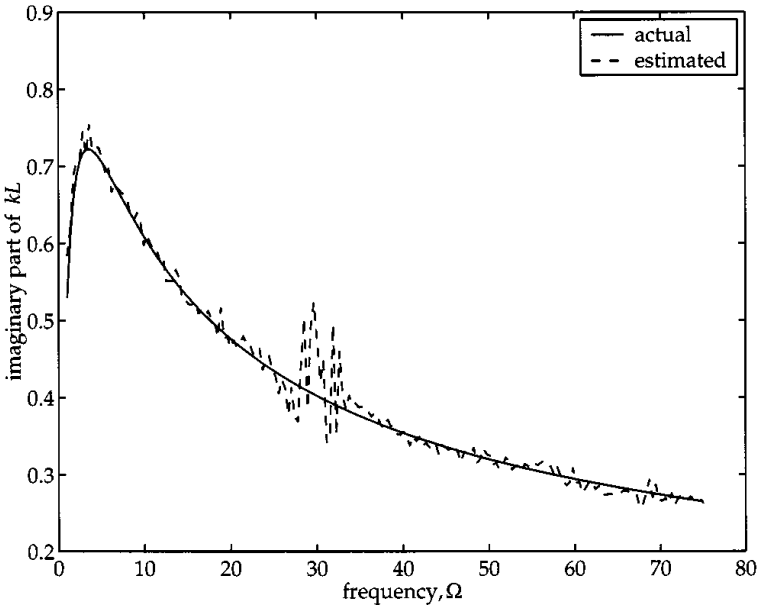

Figure I.6: Loss factor of the normalized wavenumber and the normalized frequency [62].

I. 3. 2 Discrete spatial Fourier transform

Discrete spatial Fourier transform is one of the most widely used method to determine the flexural wavenumber of structures from the measured harmonic displacement field [88, 82, 81]. The main advantage of this method is the computational efficiency due to the existing fast Fourier transform (FFT) algorithm compared to other methods. To better understand the spatial Fourier Transform, the temporal Fourier transform is described in this section. The equivalent variables time-space will be described later to apply the spatial-wavenumber Fourier Transform.

Temporal Fourier transform

Using the time convention $e^{\mathrm{i}\omega t}$, the temporal Fourier Transform and its inverse can be described as [40]:

$$F(\omega) = \int_{-\infty}^{+\infty} f(t) e^{-\mathrm{i}\omega t} dt \quad , \tag{I.13}$$

$$f(t) = \frac{1}{2\pi} \int_{-\infty}^{+\infty} F(\omega) e^{\mathrm{i}\omega t} d\omega \quad , \tag{I.14}$$

where Eq. I.13 is the temporal Fourier transform and Eq. I.14 is the inverse temporal Fourier transform. An example of the temporal Fourier transform is shown in Fig. I.7.

Spatial Fourier transform

Analogous to the temporal Fourier transform in Eq. I.13 and in Eq. I.14, the spatial Fourier transform writes:

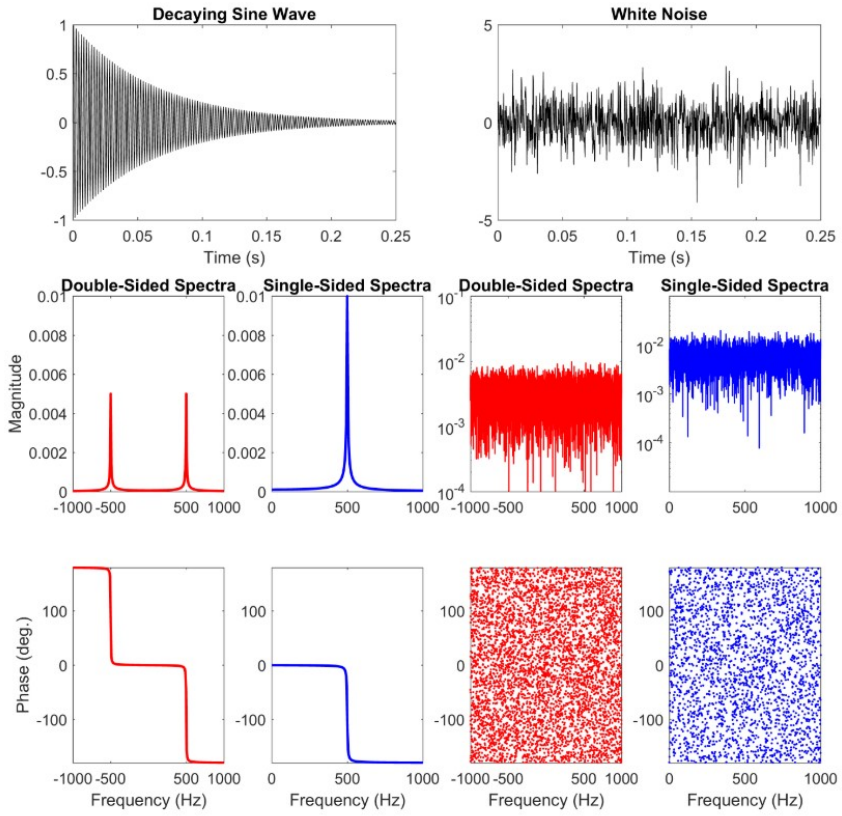

Figure I.7: Time and frequency representation of a 500 Hz decaying sine wave and random noise [40].

$$F(k) = \int_{-\infty}^{+\infty} f(r) e^{\mathrm{i}k.r} dr \quad , \tag{I.15}$$

$$f(r) = \frac{1}{2\pi} \int_{-\infty}^{+\infty} F(k) e^{-\mathrm{i}k.r} dk \quad , \tag{I.16}$$

where Eq. I.15 is the spatial Fourier transform and Eq. I.15 is the inverse spatial Fourier transform. The main difference between the temporal Fourier transform and the spatial Fourier transform is the operating variables that have changed from ωt to kr. However, the spatial Fourier transform is more complex than the temporal Fourier transform because the transforms are over two dimensions, in some cases three dimensions, and negative wavenumber terms are important [40]. The parallel between both Fourier transforms is presented in Table I.1 [31].

The spatial Fourier transform has been extensively used in determining the flexural wavenumber of 2D planar structures. This method assumes the harmonic displacement of the form:

$$w(x, y, t) = \frac{1}{2\pi} \int_{-\infty}^{+\infty} \hat{w}(x, y) e^{\mathrm{i}\omega t} d\omega \quad , \tag{I.17}$$

where $\hat{w}(x, y)$ is the frequency dependent displacement field. In the discrete domain, the displacement field of Eq. I.17 can be described as:

Temporal Fourier Transform		Spatial Fourier Transform	
Time (s)	Frequency (Hz)	Space (m)	Wavenumber (rad/m)
Number of points: N		Number of points: N	
Acquisition time: T	$f_e = \frac{1}{dt} = \frac{N}{T}$	Measurement length: L	$K_e = \frac{2\pi N}{L}$
$dt = \frac{T}{N}$	$df = \frac{1}{T}$	$dL = \frac{L}{N}$	$dK = \frac{2\pi}{L}$
	$f_{max} = \frac{f_e}{2}$		$K_{max} = \frac{\pi N}{L}$

Table I.1: Parallel between the temporal Fourier transform and spatial Fourier transform. f_e is the sampling frequency, K_e is the sampling wavenumber, dt is the time resolution, df is the frequency resolution, dL is the length resolution, dK is the wavenumber resolution, f_{max} is the maximum frequency and K_{max} is the maximum wavenumber [31].

$$\hat{w}(x_i, y_j) = \frac{1}{2\pi} \sum_{p=0}^{N_1-1} \sum_{q=0}^{N_2-1} \widehat{\hat{w}}(k_{xp}, k_{yq})\, \mathrm{e}^{-\mathrm{i}(k_{xp}x_i + k_{yq}y_j)} \quad , \tag{I.18}$$

where N_1 and N_2 are the number of measured data along axes x and y. The exponential terms k_{xp} and k_{yq} writes:

$$k_{xp} = p\Delta k_x \quad \text{and} \quad k_{yq} = q\Delta k_y \quad , \tag{I.19}$$

where $\Delta k_x = \frac{2\pi}{N_1 \Delta x}$ and $\Delta k_y = \frac{2\pi}{N_1 \Delta y}$ are the discrete wavenumbers along axes x and y. The Discrete Fourier transform $\hat{w} \longrightarrow \widehat{\hat{w}}$ writes [42]:

$$\widehat{\hat{w}}(k_{xp}, k_{yq}) = \frac{1}{N_1 N_2} \sum_{i=0}^{N_1-1} \sum_{j=0}^{N_2-1} \hat{w}(x_i, x_j)\, e^{\mathrm{i}(k_{xp}x_i + k_{yq}y_j)} \quad . \tag{I.20}$$

Ichchou et al. [42, 43] applied the DFT to identify the guided waves in a ribbed plate. The characteristic of the panel with an area of 1.2 x 0.9 m^2 is described in Table. I.2. The multi-modes dispersion curve of the ribbed panel have been experimentally identified and the result is shown in Fig. I.8. For the identification of the guided waves, the filtering of the signal and the inverse discrete Fourier transform are applied. The summary of the method is shown in Fig. I.9.

The rapidity and bijectivity of the method present major advantages compared to other methods. The bijectivity means that the DFT can be inversed and filtering of the

	ρ	E	ν	G	h		
Plate	2800 kg m^{-3}	75 GPa	0.33	28 GPa	1.25 mm		
	ρ	E	ν	G	a	b	p
Ribs	2800 kg m^{-3}	75 GPa	0.33	28 GPa	10 mm	10 mm	10 cm

Table I.2: Characteristics of the ribbed plate with a and b are the width and the height of the ribs respectively and p is the spacing between two ribs [43].

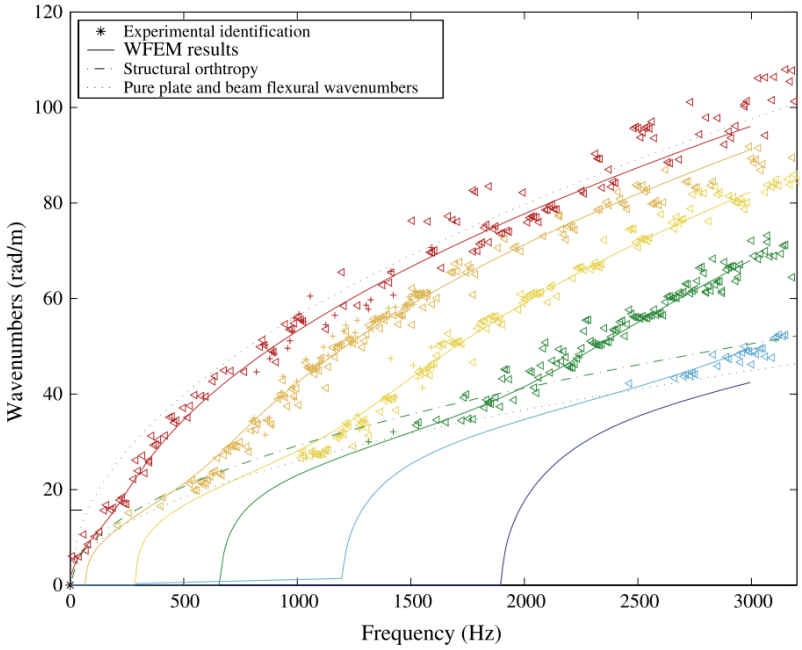

Figure I.8: Experimental identification of the multi-modes dispersion curve. The result is compared to the Wave Finite Elements Method (WFEM), the homogenized orthotropy model and the pure plate and beam flexural wavenumber. Remark: The marker $*$ is represented by the marker $\triangleleft$ with different colours in the figure [43].

signal is possible. The rapidity of the method can be achieved by using a Fast Fourier Transform (FFT) algorithm.

However, the DFT presents few major drawbacks such as aliasing, leakage and poor resolution. The aliasing is due to the field discretization of the form:

$$\widehat{\hat{w}}\left(k_x, k_y\right) = \widehat{\hat{w}}\left(k_x + \frac{2\pi}{\Delta x}, k_y\right) = \widehat{\hat{w}}\left(k_x, k_y + \frac{2\pi}{\Delta y}\right) \quad . \tag{I.21}$$

The DFT is $\frac{2\pi}{\Delta x}$-periodic. This property implies erroneous treatment outside the domain $[-\frac{\pi}{\Delta x}, \frac{\pi}{\Delta x}]$ or $[-\frac{\pi}{\Delta y}, \frac{\pi}{\Delta y}]$. The leakage is due to the finite space of the field. A singular wavenumber (k_x, k_y) appears as a cardinal sine shape instead of a Dirac distribution.

The wavenumber resolution depends on the k-space grid where the poor resolution may be induced. The DFT is also limited to the real part of the wavenumber only, thus making it impossible to estimate the damping loss factor using this method. The method has been successfully applied to complex structures such as a sandwich carbon fiber panel

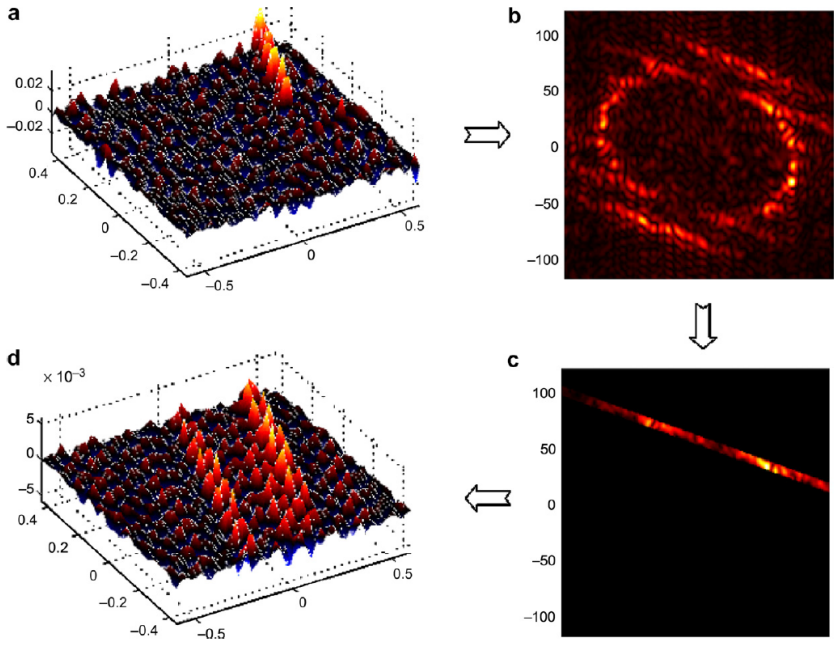

Figure I.9: Process to distinguish the multi-mode dispersion curve. a) The spatial velocity a ribbed panel at 2400 Hz. b) The wavenumber of the ribbed panel by applying the DFT. c) Filtering of the propagation segment to identify the guided wave. d) Inverse DFT of the progagation segment of the guided wave [42].

with a honeycomb core [20] and a ribbed aircraft panel [31]. In the next section, the Inhomogeneous Wave Correlation method that overcomes the limitation of the DFT is presented.

I. 3. 3 Inhomogeneous Wave Correlation method

The Inhomogeneous Wave Correlation (IWC) developed by Berthaut et al. [6, 7] extends the McDaniel method for two-dimensional structures and the Fourier transform for the identification of the damping loss factor. This approach calculates the correlation between the measured displacement field $\hat{w}(x, y)$ and an inhomogeneous wave defined as:

$$\hat{\sigma}_{k,\gamma,\theta}\left(x_i, y_i\right) = \mathrm{e}^{-\mathrm{i}k(\theta)(1+\mathrm{i}\gamma(\theta))(x_i\cos\theta + y_i\sin\theta)} \quad , \tag{I.22}$$

where k is the wavenumber, γ is the attenuation factor, θ is the propagation angle and (x_i, y_i) are the coordinates of the point i. The correlation function is given by:

$$\mathrm{IWC}(k,\gamma,\theta) = \frac{\left|\int\int_s \hat{w}.\hat{\sigma}^*_{k,\gamma,\theta}\mathrm{d}x\mathrm{d}y\right|}{\sqrt{\int\int_S |\hat{w}|^2\mathrm{d}x\mathrm{d}y.\int\int_S |\hat{\sigma}_{k,\gamma,\theta}|^2\mathrm{d}x\mathrm{d}y}} \quad , \tag{I.23}$$

where * denotes the complex conjugate. In practice, it is assumed that the measured displacement field $\hat{w}(x_i, y_i)$ is known on arbitrary data points (x_i, y_i). The integration over the complete surface S in Eq. I.23 are replaced by a finite weighted sum of the form [7]:

$$\int\int_S \mathrm{d}x\mathrm{d}y \longleftrightarrow \sum^N \rho_i S_i \quad , \tag{I.24}$$

where ρ_i is a surface integration weight at point i ($\rho_i = 1$ if the surface is divided into equal surface patches and the integrand is assumed constant over each patch) , S_i is an estimation of the surface around the point i and N is the total number of acquisition points [7]. Thus, the correlation function in the discrete form can be defined as:

$$\mathrm{IWC}(k,\gamma,\theta) = \frac{\left|\sum_{i=1}^N \hat{w}(x_i, y_i)\sigma^*_{k,\gamma,\theta}(x_i, y_i)\rho_i S_i\right|}{\sqrt{\sum_{i=1}^N |\hat{w}(x_i, y_i)|^2\rho_i S_i \sum_{i=1}^N |\sigma_{k,\gamma,\theta}(x_i, y_i)|^2\rho_i S_i}} \quad . \tag{I.25}$$

The algorithm first defines the angle θ into a discrete set of values (θ_j). For each of these angles, the value of (k_i, γ_i) that maximizes the IWC function is determined [7]. The schematic presentation of the application of the IWC method is shown in Fig. I.10.

Ichchou et al. [41] applied the method experimentally to determine the wavenumber and the bending rigidities of an orthotropic sandwich honeycomb panel. A view of the panel is presented in Fig. I.11 and the characteristic of the panel is described in Table. I.3.

The θ-dependence wavenumbers at four different frequencies (496 Hz, 1000 Hz, 2000 Hz and 3320 Hz) are shown in Fig. I.12 and the orthotropic behavior of the panel is clearly visible. A good agreement of the dispersion curve along the k_x direction and along the k_y direction compared to the model of Nilsson [65, 66] is visible on the left hand side of Fig. I.13. On the right hand side, the dynamic stiffness of the panel is well identified above 1000 Hz in Fig. I.13.

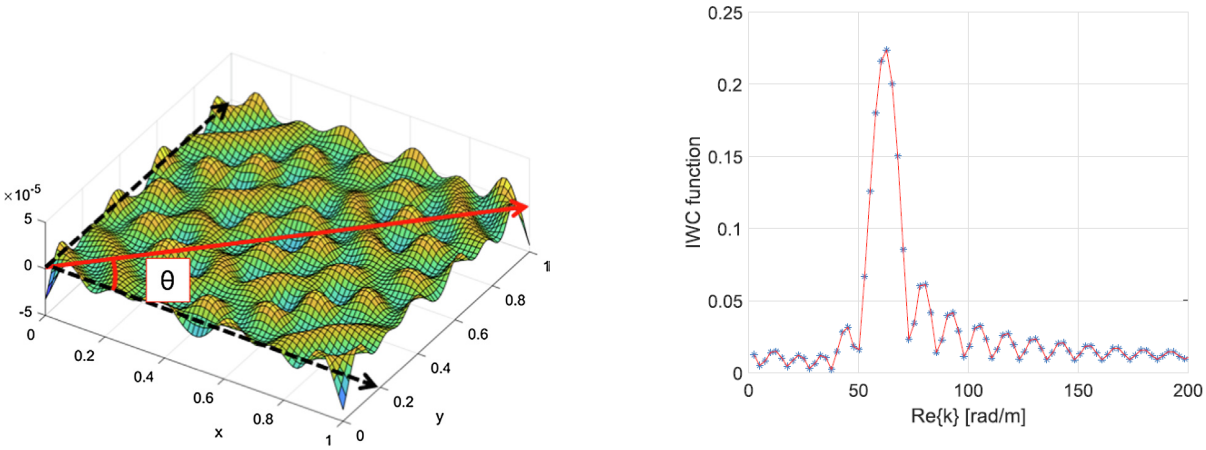

Figure I.10: Left side: The vibrational field and the presentation of the direction θ where the correlation is determined. Right side: IWC function where the index of the maximum corresponds to the wavenumber at a frequency f_0 [84].

	Face plates	Core
E_1 (GPa)	60.27	-
E_2 (GPa)	60.27	-
E_3 (GPa)	-	0.668
ν	0.029	-
G_{12} (GPa)	5	-
G_{13} (GPa)	5	0.31
G_{23} (GPa)	5	0.137
ρ (kgm^{-3})	1594	49.65

Table I.3: Properties of the sandwich honeycomb panel [41].

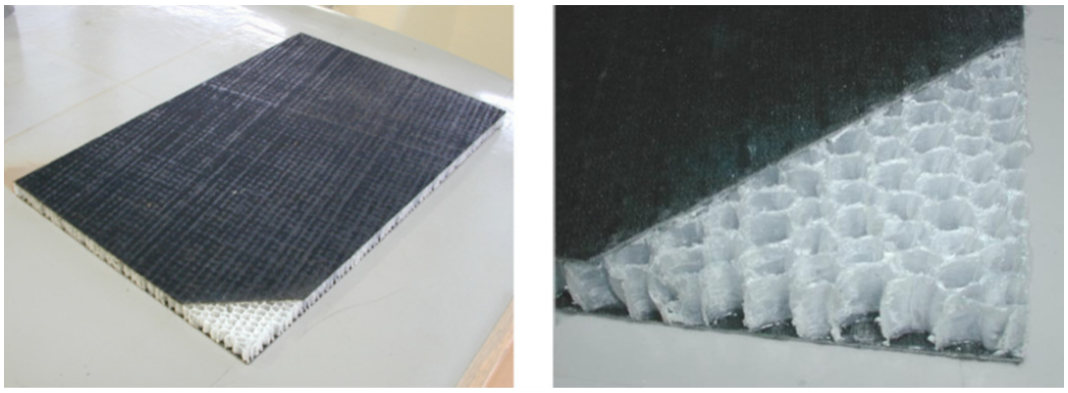

Figure I.11: Honeycomb panel [41].

Cherif et al. [21] applied the IWC method to estimate the damping loss factor of orthotropic structures using an iterative refinement process. The damping loss factor of each frequency is determined by using the following expression (further details in Section I. 5):

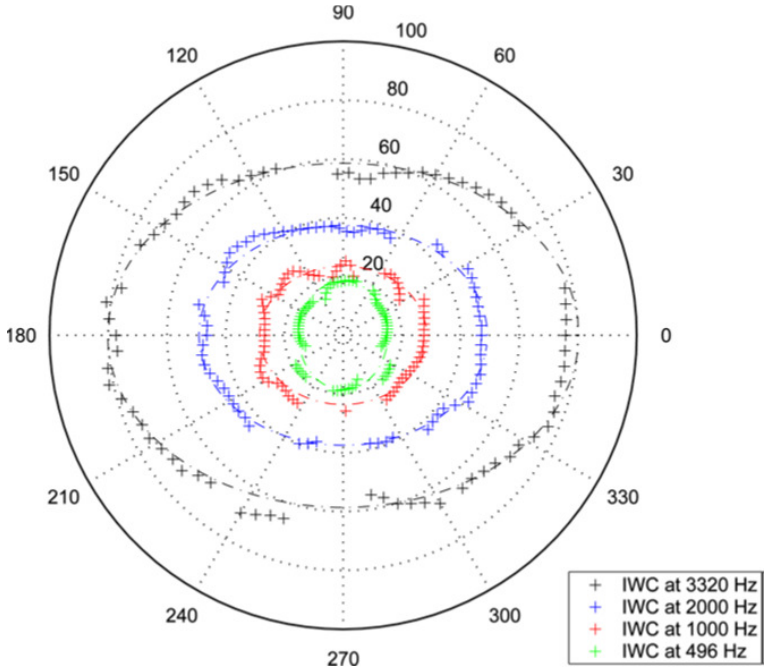

Figure I.12: θ-dependence wavenumber of the honeycomb panel [41].

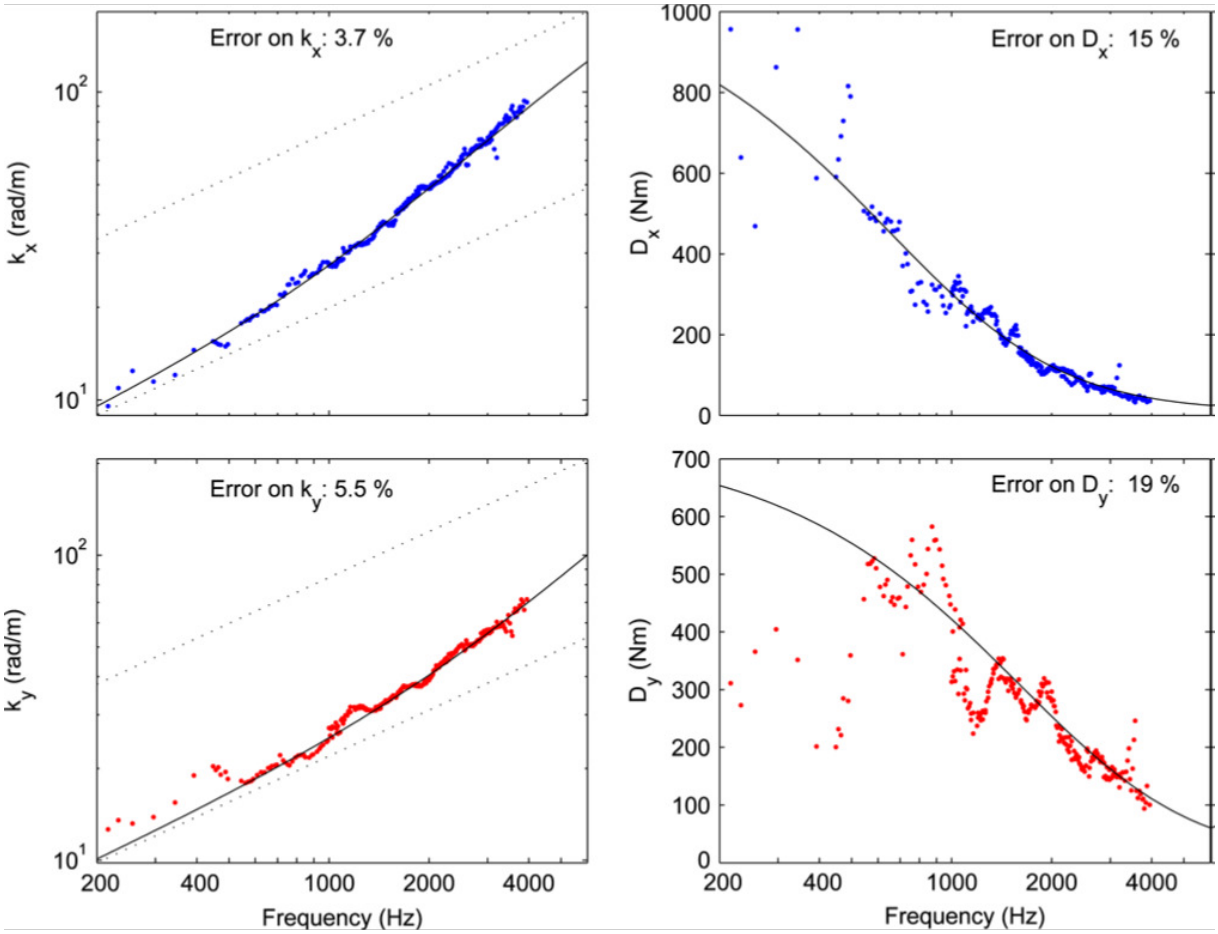

Figure I.13: Comparison of the identified wavenumber and the dynamic stiffness of the IWC method and the model of Nilsson [41].

$$\eta = \left| \frac{\mathrm{Im}(k)^4}{\mathrm{Re}(k)^4} \right| \quad . \tag{I.26}$$

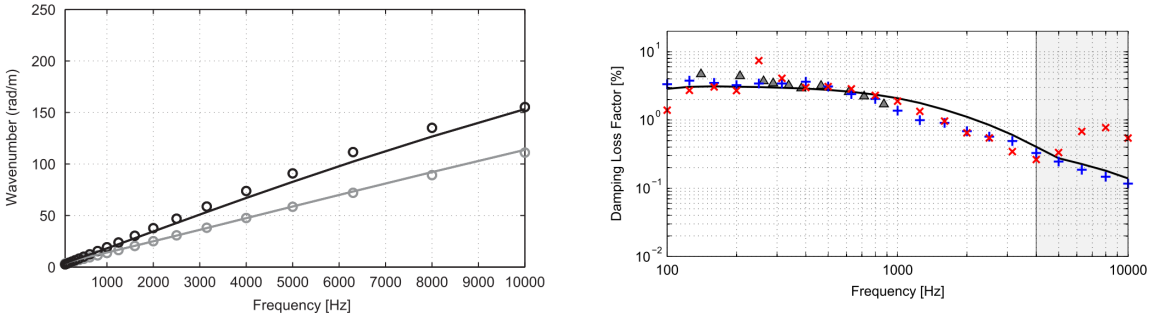

Figure I.14: Left: Dispersion curve of an orthotropic composite panel. Theoretical wavenumbers in the directions k_x (▬) and k_y (▬) vs measured wavenumbers in the directions k_x (○) and k_y (○). Right: The damping loss factor of an orthotropic composite panel. △ 3dB method, + decay rate method, × power input method and ▬ IWC method [21].

Based on Fig. I.14, the estimation of the wavenumbers correlates well with the theoretical solution based on the discrete general laminate model [36] and the estimation of the damping loss factor using the IWC method shows also a good correlation compared to other experimental methods as shown in Fig. I.14) [21].

I. 3. 4 Inhomogeneous Wave Correlation method for curved structures

Tufano et al. [84] introduced a variant formulation of the IWC method for curved structures. Using the notations and the coordinates system shown in Fig. I.15, the following relationships stand:

$$y = R\sin\varphi \approx R\varphi \quad \text{and} \quad k_\varphi = Rk_y \quad , \tag{I.27}$$

where R is the curvature radius and φ is the angular coordinates. Note that Eq. I.27 is only valid when φ is small. Substituting these relationships in the expression of the inhomogeneous wave (see Eq. I.22), the equation writes:

$$\widetilde{w}_{k,\gamma,\theta}(x,\varphi) = \mathrm{e}^{-\mathrm{i}k(\theta)(1+\mathrm{i}\gamma(\theta))((x-x_0)\cos\theta+R(\varphi-\varphi_0)\sin\theta)} \quad , \tag{I.28}$$

where φ_0 indicates the angular position of the point force. The modified inhomogeneous wave correlation writes:

$$\mathrm{IWC}(k,\gamma,\theta) == \frac{|\sum_{i=1}^{N}\hat{w}_{k,\gamma,\theta}(x_i,\varphi_i)\widetilde{w}^*_{k,\gamma,\theta}(x_i,\varphi_i)\rho_i S_i|}{\sqrt{\sum_{i=1}^{N}|\hat{w}_{k,\gamma,\theta}(x_i,\varphi_i)|^2\rho_i S_i \sum_{i=1}^{N}|\widetilde{w}_{k,\gamma,\theta}(x_i,\varphi_i)|^2\rho_i S_i}} \quad . \tag{I.29}$$

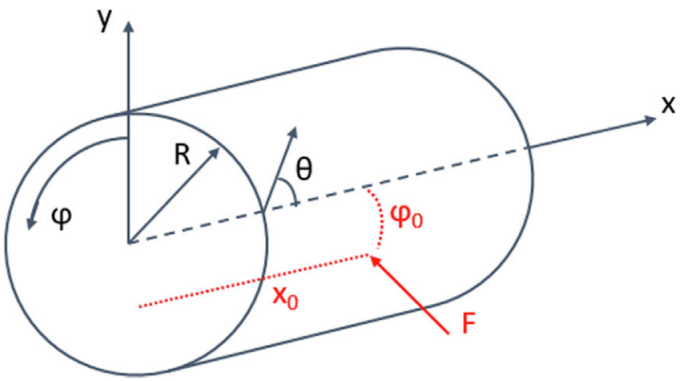

Figure I.15: Curved structure coordinates system [84].

The proposed method has been studied over an aluminium aircraft sidewall panel in three different configurations:

1. Bare configuration under a diffused acoustics field (DAF) excitation;
2. Bare configuration under a point mechanical excitation;
3. Addition of resonators to the panel under a diffused acoustics fields excitation.

Fig. I.16a shows the internal surface of the panel where the shaker is placed to excite the structure. A 3D laser vibrometer is used to scan the displacement field of the external surface. The dispersion curve is projected in two orthogonal directions, axial and circumferential directions.

(a) (b)

Figure I.16: Set-up of the experimental measurement of the panel [84].

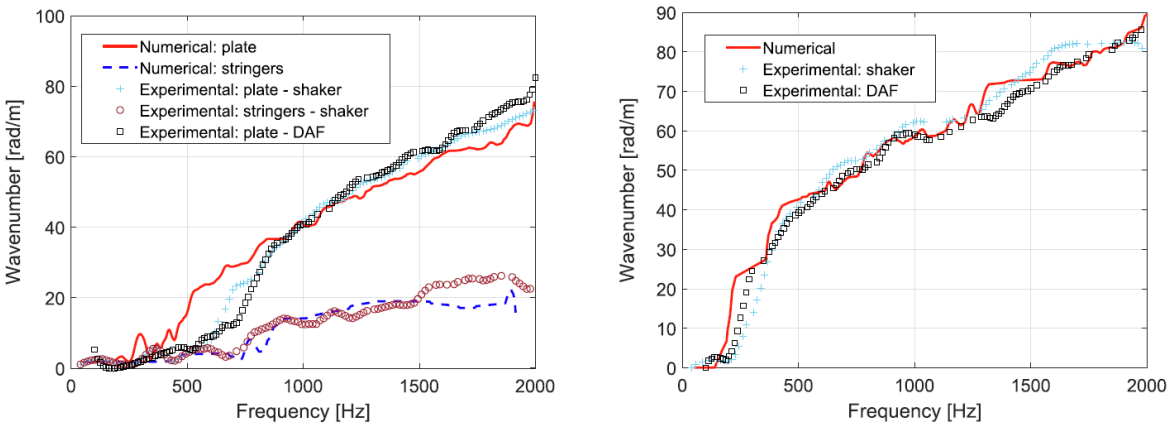

(a) (b)

Figure I.17: Dispersion curves for different types of configurations of the aluminium aircraft sidewall panel. (a) Axial direction and (b) circumferential direction [86].

Fig. I.17a represents two different modes of propagation in the axial direction: the flexural wavenumber of the plate and the flexural wavenumber of the stringer. On the other hand, a good agreement of the axial wavenumber of two different loadings: shaker and DAF are visible in Fig. I.17a. For the circumferential direction as shown in Fig. I.17b, a good agreement between the experimental dispersion curve and the numerical dispersion curve under the two different loading conditions is demonstrated.

I. 3. 5 Inhomogeneous Wave Correlation- Green's function method

The IWC method is based on the plane wave hypothesis and is therefore limited due to the nature of the plane wave itself. Indeed, the vibrational field near the excitation point cannot be compared with a plane wave. Therefore the measurements must be done over an observation area sufficiently far from the excitation point. In reality, this condition is difficult to obtain due to the finite dimensions of the panel.

To overcome this limitation, Tufano in his dissertation [83] replaced the inhomogeneous wave function by the Green's function of the isotropic infinite plate [91]. This method combines advantages of the IWC and the Green's function. Compared to the IWC method, the Green's function is more adapted to describe the vibrational field near the excitation point. Tufano applied the proposed method to an isotropic laminated plate and an isotropic homogeneous plate with tuned mass damper (TMD).

For a thin plate of infinite dimensions subject to a harmonic point excitation, the Green's function is described as [83]:

$$G_\infty(\hat{k}, r) = \frac{\mathrm{i}}{8\hat{k}^2 D}[H_0^{(1)}(\hat{k}r) - H_0^{(1)}(\mathrm{i}\hat{k}r)] \quad , \tag{I.30}$$

where G_∞ is the Green's function of the infinite plate, $\hat{k}$ is the complex wavenumber defined by $\hat{k} = k_R + \mathrm{i}k_I$, D is the bending stiffness defined by $D = \frac{Eh^3}{12(1-\nu^2)}$, E is the Young's modulus, h is the thickness, ν is the Poisson's coefficient and $H_0^{(1)}$ is the zero order Hankel's function of the first kind. The radius, r, is defined as the distance between the excitation point and the observation point.

Considering an acquisition region of area S, the normalized correlation function writes:

$$\mathrm{IWCG}(k, \gamma) = \frac{|\sum_{i=1}^{N} \hat{w}(r_i) {G_\infty}^*(\hat{k}, r_i)\rho_i S_i|}{\sqrt{\sum_{i=1}^{N} |\hat{w}(r_i)|^2 \rho_i S_i \sum_{i=1}^{N} \left|G_\infty(\hat{k}, r_i)\right|^2 \rho_i S_i}} \quad , \tag{I.31}$$

This approach estimates the complex wavenumber at each frequency by calculating the correlation between the measured displacement field and the Green's function by using Eq. I.31.

Tufano applied the method to an isotropic 1.0 m × 0.6 m thermoplastic polymer (ABS) panel (Thickness $h = 0.01$ m, Young's modulus $E = 1.0$ GPa, density $\rho = 980$ kg/m^3, Poisson's coefficient $\nu = 0.35$ and $\eta = 2\%$, 4%). The dispersion curve of the ABS is plotted in Fig. I.18a [83]. A good agreement between the proposed approach is observed in the low frequency while an overestimation is observed in the high frequency range.

The estimation of the damping loss factor using Eq. I.26 reaches asymptotically the value of the structural damping introduced in the FE model [83]. The characterization of the elastic properties using this approach is done globally by considering a full field harmonic displacement field and not for each angle separately.

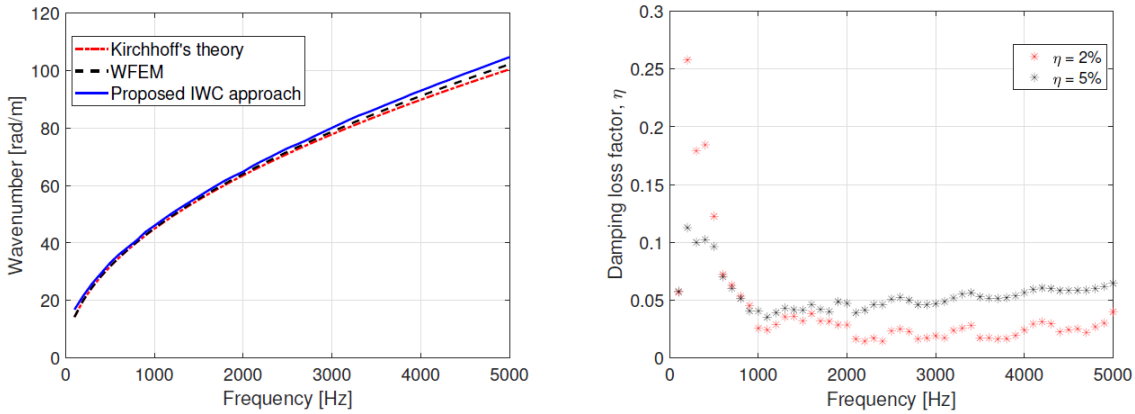

Figure I.18: Left: Dispersion curve of an isotropic ABS panel compared to other methods. Right: Damping loss factor estimation [83].

I. 3. 6 Green's function of elliptical orthotropic plates

Recently, Marchetti et al. [57] introduced a new wave fitting approach of an orthotropic elliptic plate based on the Green's function which uses the decomposition of the Hankel's function. The method considers the normal displacement field measured over a regular grid mesh (x_p, y_q). An off-axes orthotropy is considered assuming that the plate axes are different from the orthotropy axes (x', y') of the material (see Fig. I.19). The angle between the two coordinates systems corresponds to the orthotropy angle θ' [57] .

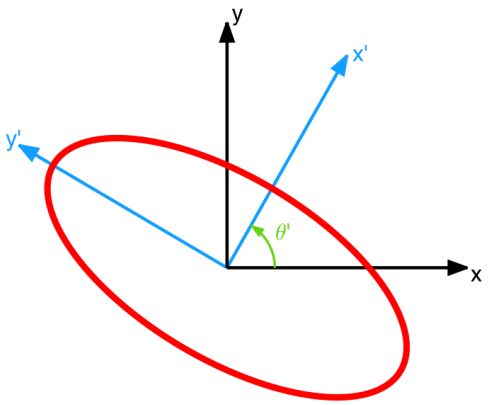

Figure I.19: Example of the flexural wavenumber curve of an elliptical orthotropic plate. (x, y) represents the measurement axes and (x', y') represents orthotropy axes [57].

The equation of motion of an orthotropic elliptic structure writes [6, 57]:

$$\left(\left(\sqrt{D'_{11}}\frac{\partial^2}{\partial x'^2}+\sqrt{D'_{22}}\frac{\partial^2}{\partial y'^2}\right)^2-\rho h\omega^2\right)w\left(x',y'\right)=\delta\left(x'-x'_0,y'-y'_0\right)\quad , \tag{I.32}$$

where w is the displacement field, ω is the angular frequency, ρ is the plate density, h is the plate thickness and (x'_0, y'_0) is the position of the source. The moduli D_{11} and D_{22} represent the flexural rigidity of the structure in (x', y').

For infinite structures, the solution of the equation of motion in Eq. I.32 writes [6]:

$$G_\infty(x', y', \omega) = \frac{\mathrm{i}}{8\sqrt{\rho h \omega^2}\sqrt[4]{D'_{11}D'_{22}}}\left(H_0^{(1)}(\kappa r) - H_0^{(1)}(\mathrm{i}\kappa r)\right) \quad , \tag{I.33}$$

where κ is a pseudo-wavenumber. The relation between the pseudo-wavenumber and the bending rigidities is described as:

$$\kappa r = \sqrt[4]{\rho h \omega^2}\sqrt{\frac{(x'-x'_0)^2}{\sqrt{D'_{11}}} + \frac{(y'-y'_0)^2}{\sqrt{D'_{22}}}} \quad . \tag{I.34}$$

The values of the bending rigidities D'_{11} and D'_{22} and the orthotropy angle θ' that minimize the error between the Green's function and the measured displacement field are considered as the dynamic material characteristic. The performance of the method is verified over a sandwich aluminium panel with a honeycomb core [57].

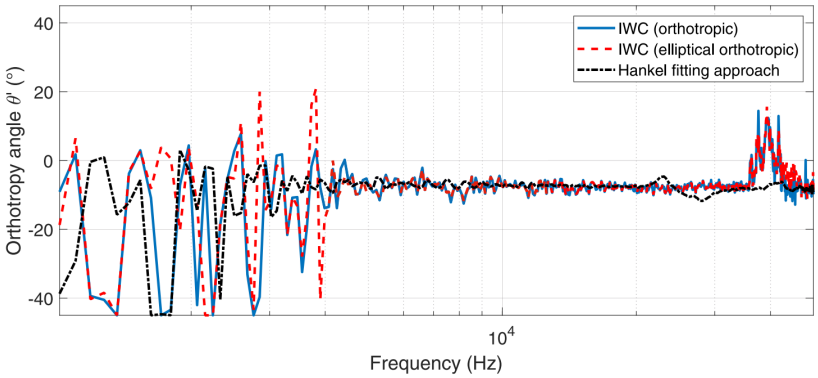

Figure I.20: Orthotropy angle identified by the Hankel fitting approach and the IWC method assuming orthotropic and elliptical orthotropic plate characteristics [57].

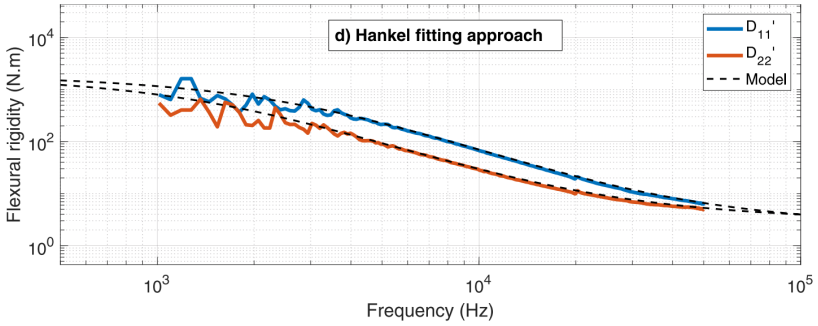

Figure I.21: Equivalent bending rigidities identified by the Hankel fitting approach [57].

The angle of orthotropy identified by the Hankel fitting approach and the IWC method is shown in Fig. I.20. Fig. I.21 compares the estimation of the bending rigidities using Hankel fitting versus the analytical model [57]. A good correlation between all the methods is observed above 4.5 kHz.

This approach is based on the knowledge of the analytical solution of the Green's function of elliptical orthotropic plates defined in the thesis of Berthaut [6]. The applicability of this method to any kind of structures is however limited.

I. 4 Classical damping loss factor measurement techniques

A good estimation of the damping remains a big challenge in the research domain due to the complexity of the dynamic interaction of system joints and geometry [11]. Various damping test methods have been developed throughout the years to characterize the performance of damping treatments [21]. These methods can be classified into three main groups. The first is the frequency-domain modal analysis for example the half-power bandwidth method. The second is the time domain decay-rate methods such as the decay rate method (DRM). The third is the method based on energy and wave propagation such as the power input method (PIM). In this section, these classical damping loss factor characterization techniques are presented.

I. 4. 1 Half-power bandwidth method (3dB method)

The half-power bandwidth or the 3dB method is broadly used to estimate the damping loss factor in the low frequency range and assumes low damping [23, 29]. This method is based on the estimation of the damping from the frequency response function of a system. In theory, the damping is proportional to the width of the magnitude of the displacement based transfer function curve when the magnitude is 3dB down from the peak.

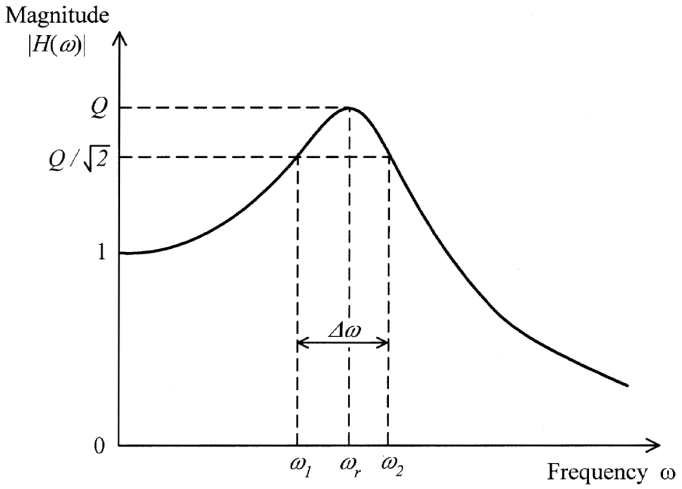

Figure I.22: Schematic presentation of the half-power bandwidth method in estimating the damping ratio [29].

This method has been extensively adopted to the single-degree-of-freedom (SDOF) and to the multi-degree-of-freedom (MDOF) systems. The application of this method to MDOF systems is based on the assumption that each peak in the frequency response function is affected only by the mode under study, which requires small damping (negligible modal overlap) [67].

The frequency response function of a single degree of freedom system with viscous damping excited by a harmonic force writes [67]:

$$|X(\omega)| = \frac{1}{1-(\omega/\omega_n)^2 + 2\mathrm{i}\xi(\omega/\omega_n)} \quad , \tag{I.35}$$

where ω_n is the natural frequency and ξ is the damping ratio. For low damping structures where $\xi \ll 1$, the peak magnitude at resonance is written as:

$$|X(\omega_n)| = \frac{1}{2\xi} \quad . \tag{I.36}$$

Half-power bandwidth is defined as the width $\Delta\omega$ of the frequency-response magnitude curve when the magnitude is $\frac{1}{\sqrt{2}}$ of the peak (see Fig. I.22). The half-power points are given by:

$$\frac{1}{\sqrt{2}}\frac{1}{2\xi} = \left|\frac{1}{1-(\omega/\omega_n)^2 + 2\mathrm{i}\xi(\omega/\omega_n)}\right| \quad . \tag{I.37}$$

For low damping structures, the two roots of Eq. I.37, ω_1 and ω_2 is written as [29]:

$$\frac{\omega_2 - \omega_1}{\omega_n} = 2\xi \quad . \tag{I.38}$$

The modal damping ratio ξ can be related to the structural damping loss factor η by the relation [35]:

$$\eta = 2\xi\sqrt{1-\xi^2} \quad . \tag{I.39}$$

For low damping structures, the relation $\eta = 2\xi$ is rather used [32]. In practical, the application of the method can be influenced by several factors [78]. The first is the choice of the frequency resolution ΔHz that may influence the extraction of the frequency. The second is the spacing between two modes (see Fig. I.23). To avoid this second problem, a modal separation method needs to be applied to separate both peaks.

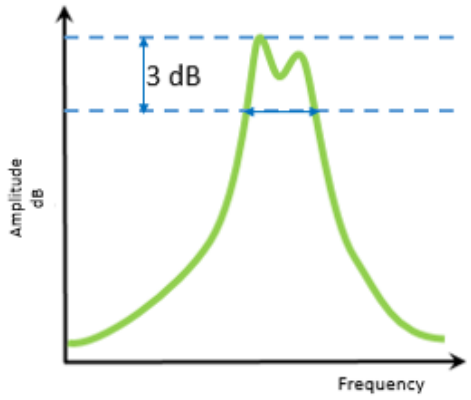

Figure I.23: Example of two closely spaced modes [78].

The method can be applied by measuring the frequency response function of a point of the panel subject to an excitation. The measurement can be done at few points and the

average damping loss factor can be obtained. However, this method is only applicable in the low frequency range where the modal density and the modal overlap are low. In high frequency range, methods based on the statistical energy analysis can be adopted. In the next section, the method based on the decay rate and the power input are discussed.

I. 4. 2 Decay Rate Method

The decay rate method is based on the logarithmic decrement of the transient structural response which is described as the response of an oscillator submitted to a mechanical force at time $t = 0$ [47]. The method assumes the damping is similar for all the modes in the frequency band (third-octave band here).

The amplitude of the response after the excitation will decay exponentially at a rate of $G\mathrm{e}^{(-\pi f \eta t)}$, where G is the gain, f is the frequency, η is the damping loss factor and t is the measurement time (see Fig. I.24).

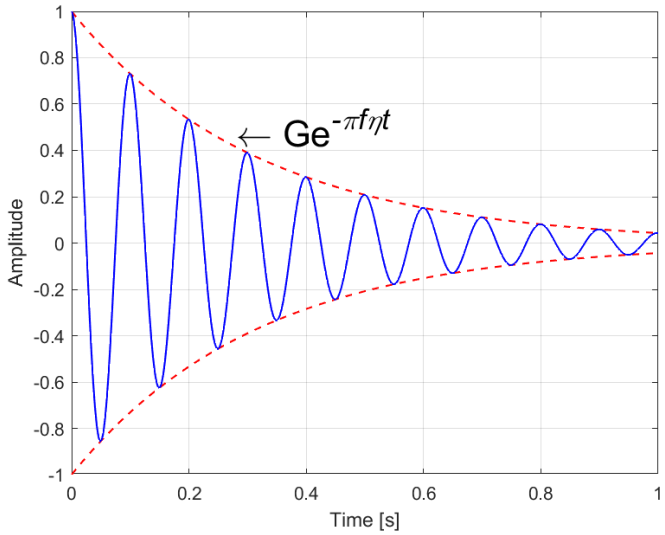

Figure I.24: Transient response of a single degree of freedom system.

For low damping structures, the decay slope Δ_{dB} between two instances, t_1 and t_2 with amplitudes G_1 and G_2 in decibels is described by [11]:

$$\begin{aligned} \Delta_{dB} &= 20\log_{10}\frac{G_1}{G_2} \quad , \\ &= 20\log_{10}\frac{G\mathrm{e}^{-\pi f \eta t_1}}{G\mathrm{e}^{-\pi f \eta t_2}} \quad , \\ &= 27.3 f \eta (t_2 - t_1) \quad . \end{aligned} \tag{I.40}$$

The decay rate $D = \Delta_{dB}/(t_2 - t_1)$ is described as the difference of the gain decibels in function of time. Thus, the solution of Eq. (I.40) in function of the damping loss factor is defined as:

$$\eta = \frac{D}{27.3f} \quad . \tag{I.41}$$

In practical, the measurement can be done by using an impact hammer and an accelerometer over few excitation points. The result is then averaged spatially on one-third octave frequency band.

This method is classically used in SEA related studies. For examples, Bolduc et al. [13, 12] and Cherif et al. [21, 22] used the method to estimate damping for several types of structures: a flat isotropic panel, an aircraft side wall (a curved ribbed panel) and a sandwich carbon fiber panel with a honeycomb core.

I. 4. 3 Power Input Method

The estimation of the damping loss factor using the power input method is based on the quotient between the power injected to the system and the dissipated energy.

The principle of the method is described in this section. Under the hypothesis of steady-state conditions where the input energy is assumed to be equal to the dissipated energy, the loss factor of a structural system can be written as [11, 53]:

$$\eta(\omega) = \frac{E_{in}}{E_T} \quad , \tag{I.42}$$

where E_{in} is the input energy and E_T is the average total energy of the system.

In practical, the input energy E_{in} can be expressed in term of input power of the form $P_{in} = \omega E_{in}$ and can be calculated with a simultaneous measurement of the force and the velocity at the point of excitation. The input power can be described as:

$$P_{in} = \frac{1}{2} |F|^2 \, Re\{Q(\omega)\} \quad , \tag{I.43}$$

where F is the input force and $Q(\omega)$ is the input mobility. The input mobility is defined as the quotient between the input velocity V_{in} and the input force. This relation writes:

$$Q(\omega) = \frac{V_{in}(\omega)}{F} \quad . \tag{I.44}$$

The calculation of the total energy E_T requires an assumption, the total energy E_T is equal to twice the kinetic energy of the system [11]. The total energy writes:

$$E_T = M\langle v^2 \rangle \quad , \tag{I.45}$$

where M is the mass of the system and $\langle v^2 \rangle$ is the average quadratic velocity of the system. The damping loss factor is now defined as:

$$\eta = \frac{P_{in}}{\omega E_T} = \frac{\frac{1}{2} |F|^2 \, Re\{Q(\omega)\}}{\omega M \langle v^2 \rangle} \quad . \tag{I.46}$$

The power input method exploits the relation between the power and the energy under the assumption of the statistical energy analysis. This method supposes that the damping of the system is low and the damping is the same for all modes. To obtain a more accurate result in estimating the damping loss factor, the measurement needs to be averaged to few measurement locations and averaged over a frequency band (most commonly one-third octave band).

In addition, the excitation must be done far from the edge to avoid error in calculating the input power due to evanescent waves generated at boundaries. On the other hand, the measurement must be done outside a circle R_D from the excitation point to respect the reverberant field criterion. Inside the circle, the measured field is dominated by the direct field. The radius writes [19, 53]:

$$R_D = \frac{\omega \eta h}{2\pi c_g} \quad , \tag{I.47}$$

where η is the damping estimated using the 3dB method, h is the thickness of the panel and c_g is the group velocity.

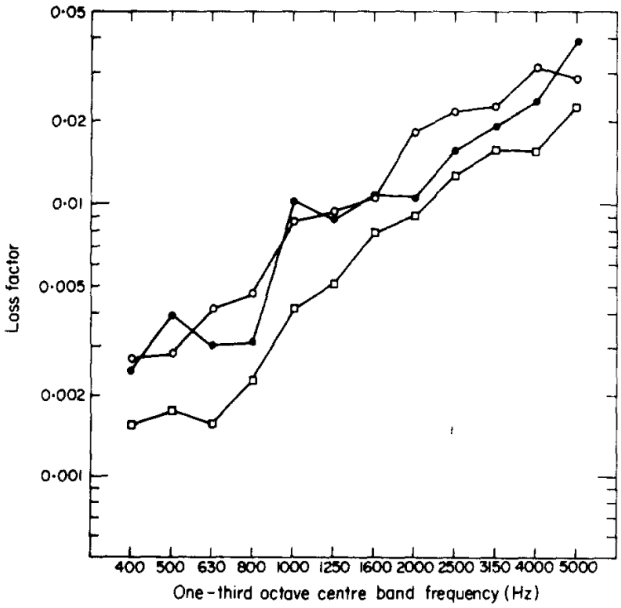

Figure I.25: Damping loss factor a steel plate. ∘ steady state method, □ decay rate method and • *in situ* power input method [9].

Bies et al. [9] applied the decay rate method and the power input method to a mild steel flat panel of 1 mm in thickness and 0.2 m^2 in area. The method is compared to the steady state method that is based on the power balance equation of a system [9]. The measurement of loss factors using the decay rate method is underestimated compared to the power input method. Furthermore, the estimation of the damping loss factor using the *in situ* power input method shows a good correlation compared to the steady state method as shown in Fig. I.25. The reason for the discrepancy between the steady state and the transient method is that the energy distribution among modes of the system during reverberant decay is not in steady state equilibrium [9].

Cherif et al. [20] applied the 3dB method, the power input method and the decay rate method on two composite sandwich panels with different thickness. Mechanical properties

of both panels are described in Fig. I.4. The estimation of the damping loss factor for the thin and the thick panels is shown in Figs. I.26a-b. For both panels, the decay rate method and the power input method are reliable compared to the 3dB method from 200 Hz to 1000 Hz. In the high frequency range (gray area in Figs. I.26a-b) , the power input method shows discrepancies due to the limitation in injecting power to the system [20].

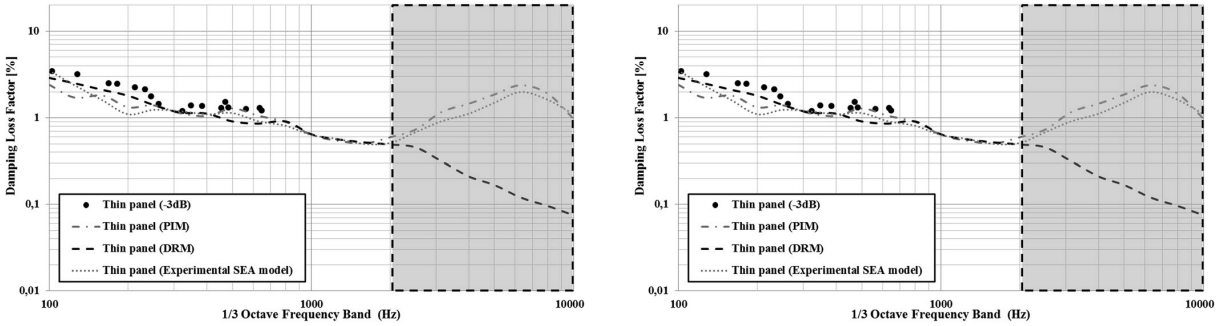

(a) Thin composite sandwich panel.

(b) Thick composite sandwich panel.

Figure I.26: Comparison of the damping loss factor between the 3dB method, the power input method and the decay rate method [20].

	Thick panel skins	Core	Thin panel skins	Core
h (mm)	0.96	25.4	0.51	6.35
E_1 (GPa)	46	0.001	23.6	0.001
E_2 (GPa)	46	0.001	23.6	0.001
E_3 (GPa)	46	0.179	23.6	0.001
G_{12} (GPa)	17.6	1	10.34	1
G_{13} (GPa)	17.6	26	10.34	44.8
G_{23} (GPa)	17.6	56	10.34	24.1
ν_{12}	0.3	0.45	0.141	0.45
ν_{13}	0.3	0.01	0.141	0.01
ν_{23}	0.3	0.01	0.141	0.01
ρ (kg/m3)	1900	64	1900	48

Table I.4: Mechanical properties of the thin and thick sandwich carbon fiber honeycomb panels [20].

The decay rate method and the power input method that are based on statistical energy analysis assumptions allow the estimation of the damping behavior in the high frequency range. However, these approaches provides only spatially averaged power for each substructure of the considered system in a defined frequency band (most commonly one-third octave band).

I. 5 Spatial damping loss factor

The attenuation of a plane wave γ is defined by the complex wavenumber of the form $\hat{k} = k(1 + \mathrm{i}\gamma)$. For an infinite structure, the exponential decay of vibration energy with distance r can be described as [24]:

$$< E_{decay} >= E_0 e^{-\frac{\eta\omega r}{c_g}} \quad , \tag{I.48}$$

where $c_g = \partial\omega/\partial k$ is the group velocity and E_0 is the initial energy. The angular frequency can also be written in the form of $k = \omega/c_\varphi$ where k is the wavenumber and c_φ is the phase velocity. Eq. I.48 can then be written as:

$$< E_{decay} >= E_0 e^{-\eta\frac{c_\varphi}{c_g}kr}. \tag{I.49}$$

On the other hand, a harmonic displacement field can be defined in the form of $e^{-\mathrm{i}kr}e^{-\gamma kr}$. The decay energy of the displacement field can be described as:

$$< E_d >= E_0 e^{-2\gamma kr}. \tag{I.50}$$

Equating both propagating energy equations, the damping loss factor can be defined as:

$$\eta = 2\gamma\frac{c_g}{c_\varphi} = 2\frac{\mathrm{Im}(k)}{\mathrm{Re}(k)}\frac{c_g}{c_\varphi} \quad . \tag{I.51}$$

For pure bending waves propagation, the group velocity and the phase velocity is related by $c_g = 2c_\varphi$. For longitudinal waves or shear waves, the medium is not dispersive thus $c_g = c_\varphi$.

I. 5. 1 Love-Kirchhoff's theory

Most commonly, the damping loss factor can be derived from the flexural wavenumber k_f based on the Love-Kirchhoff's theory of a thin plate. The equation writes [73, 62, 21, 56]:

$$\eta_{eq} = \left|\frac{\mathrm{Im}(k_f)^4}{\mathrm{Re}(k_f)^4}\right| \quad . \tag{I.52}$$

The theory considers a constant ratio $c_g/c_\phi = 2$. In general, this relation is only valid for pure bending and not applicable for thick structures. Fig. I.27 shows the velocity ratios and the damping loss factor determined using Eqs. I.51 and I.52 for different values of thickness of a sandwich beam. The properties are given in Table I.5.

The ratio is approximately equal to 2 for a thin core on the entire frequency range as the behavior of the sandwich panel is dominated by the bending motion. The damping loss factor estimation using Eq. I.51 and Eq. I.52 shows a good correlation. For a thick

core, the ratio is approximately equal to 1 above 1000 Hz as the behavior of the thick sandwich panel is dominated by the shearing of the core. The estimation of the damping loss factor using the Love-Kirchhoff's theory is overestimated.

In conclusion, the Love-Kirchhoff's damping theory can easily be applied based on the knowledge of the flexural wavenumber but only limited to thin structures. Meanwhile, the damping loss factor estimation using Eq. I.51 is more general for both thin and thick structures because this approach takes into account the wave propagation behavior.

	h (mm)	ρ (kg/m^3)	E (GPa)	G (GPa)	η
First skin	0.75	2700	70	-	0.001
Core	10.2	74	0.130	0.045	0.04
Second skin	2	2700	70	-	0.001

Table I.5: Characteristic of the sandwich beam [56].

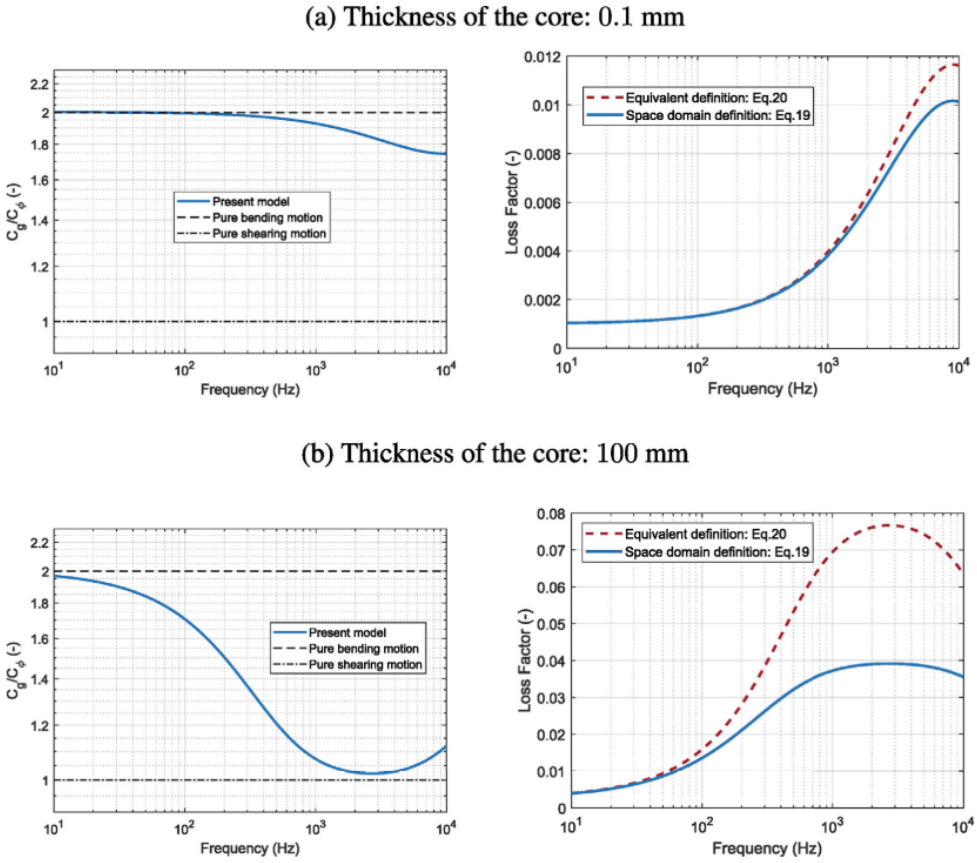

Figure I.27: Velocity ratios and comparison of the equivalent and apparent loss factors of a sandwich plate for different values of thickness of the core [56].

I. 5. 2 Spatial average damping loss factor

The average damping loss factor of an isotropic panel can be described as:

$$< \eta(\omega) >= \frac{\int_0^{2\pi} \eta(\omega,\theta)\mathrm{d}\theta}{\int_0^{2\pi} \mathrm{d}\theta} \quad . \tag{I.53}$$

However, the relation is not applicable to non-isotropic structures because the number of modes is different in each direction and the damping loss factor varies in each direction. Manconi et al. [54] describes the method to calculate the average damping loss factor of non-isotropic structures by considering the modal density [54]. A more general average loss factor formulation is given by:

$$\bar{\eta}(\omega) = \frac{\int_0^{2\pi} \eta(\omega,\theta) n(\omega,\theta)\mathrm{d}\theta}{\int_0^{2\pi} n(\omega,\theta)\mathrm{d}\theta} \quad , \tag{I.54}$$

where $n(\omega,\theta)$ is the angular modal density for each direction given by [53, 36]:

$$n(\omega,\theta) = \frac{S}{\pi^2}\frac{k(\omega,\theta)}{c_g(\omega,\theta)} \quad . \tag{I.55}$$

Here S is the area of the structure and $k(\omega,\theta)$ and $c_g(\omega,\theta)$ are the wavenumber and the group velocity at each angle and each frequency. Finally, the average loss factor of non-isotropic structures is written as:

$$\bar{\eta}(\omega) = \frac{\int_0^{2\pi} \eta(\omega,\theta)\frac{k(\omega,\theta)}{c_g(\omega,\theta)}\mathrm{d}\theta}{\int_0^{2\pi} \frac{k(\omega,\theta)}{c_g(\omega,\theta)}\mathrm{d}\theta} \quad . \tag{I.56}$$

The method defined in Eq. I.56 is adapted in this thesis, and the same averaging method is also used in the reference analytical solution based on the discrete general laminate model [36] (further details in Section I. 7).

I. 6 Image source method

The Green's function of an infinite plate estimates the damping loss factor precisely. However, the method shows some discrepancies and is relatively less accurate in the low frequency range and for lightly damped structures. This is due to the reflection at boundaries which is ignored in the free field Green's function.

In this section, the image source method for simply supported and roller supported developed by Gunda et al. [37, 38] is first discussed. In the second part, the image source method for abritrary boundary conditions developed by Cuenca et al. [25, 27, 28] is then explained.

I. 6. 1 Image source method for simply supported and roller supported panels

The image source method or ray tracing techniques has been commonly employed in disciplines such as acoustics, optics and electromagnetics. The work presented here is an extension of the image source method in structural vibrations.

Gunda et al. [37] uses the combination of the image source method and the Hankel's functions to construct the Green's function of a finite plate with simply supported boundary conditions. The feasibility of the method has been demonstrated by Gunda in calculating the frequency-dependent response of thin plates and beams with simply supported and roller supported panel.

The principle of the method is detailed in this section. The fundamental solution of the isotropic Green's function described in Eq. I.30 is based on the assumption that the plate is infinite. To apply this to a finite plate, the boundary conditions on the plate edge have to be satisfied [37].

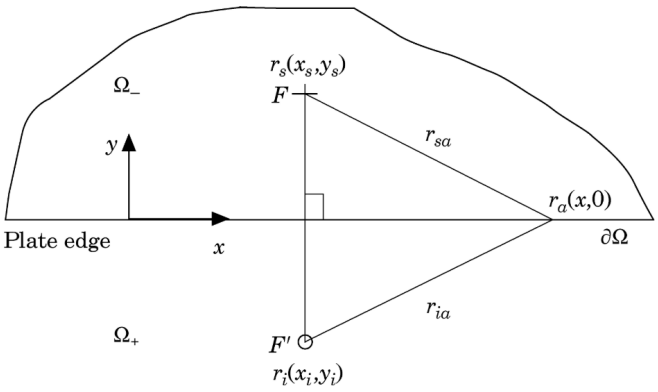

Figure I.28: Schematic presentation of a semi-infinite plate [37].

To obtain the solution for a semi-infinite plate subjected to a point force F at point $r_s(x_s, y_s)$, an imaginary point force F' at a distance y_s from the edge is introduced. This distance is equal to the distance of F from the edge of the plate. Assumes $r_a(x, 0)$ be any point on the edge of the semi-infinite plate (see Fig. I.28). $r_s(x_s, y_s)$ and $r_s(x_i, y_i)$ are the

coordinates of the source and the image points respectively. The distances of the source and image locations writes:

$$r_{sa} = r_{ia} = r = \sqrt{(x - x_s)^2 + y_s^2} = \sqrt{(x - x_i)^2 + y_i^2} \quad . \tag{I.57}$$

The deflection u, the normal slope θ, the shear force F_y and the bending moment M_y at the edge of the plate can be expressed by calculating the sum of contributions from both sources. These relationships write:

$$w = -\frac{\mathrm{i}\,(F + F')}{8\hat{k}^2 D}\left[H_0^{(1)}(\hat{k}r) - H_0^{(1)}(\mathrm{i}\hat{k}r)\right] \quad , \tag{I.58}$$

$$\theta = \frac{(F' - F)\,\mathrm{i}y_0}{8\hat{k}^2 D\, r}\frac{\partial}{\partial r}\left[H_0^{(1)}(\hat{k}r) - H_0^{(1)}(\mathrm{i}\hat{k}r)\right] \quad , \tag{I.59}$$

$$F_y = \frac{\mathrm{i}y_0\,(F' - F)}{8\hat{k}^2}\nabla^2\left(\frac{1}{r}\frac{\partial}{\partial r}\left[H_0^{(1)}(\hat{k}r) - H_0^{(1)}(\mathrm{i}\hat{k}r)\right]\right) \quad , \tag{I.60}$$

$$M_y = \frac{(F + F')}{8\hat{k}^2}\left\{\left\{\left(\frac{1}{r} - \frac{y_0^2}{r^3}\right) + \nu\left(\frac{1}{r} - \frac{x^2}{r^3}\right)\right\}\frac{\partial}{\partial r} + \left(\frac{y_0^2}{r^2} + \nu\frac{x^2}{r^2}\right)\frac{\partial^2}{\partial r^2}\right\}\left[H_0^{(1)}(\hat{k}r) - H_0^{(1)}(\mathrm{i}\hat{k}r)\right] \quad . \tag{I.61}$$

Based on relationships described above, the simply supported boundary conditions where the deflection and the bending moment are zeros implies the relation $F' = -F$. The roller boundary conditions where the normal slope and the shear force are zeros implies the relation $F' = F$.

However, the reflection coefficient of the free-free and the clamped boundary conditions along the plate edge is not directly applied because the reflected wave has a local near field response which includes wave propagation along the edge of the plate and evanescent waves in orthogonal directions [18]. A different approach is required for these two boundary conditions and will be briefly discussed later in this section.

Gunda applied the method to a finite simply supported rectangular plate. The configuration of the image source contributions is shown in Fig. I.29.

The proposed method is compared with an example of a simply supported rectangular steel plate. The dimensions of the panel are length $a = 0.5842$ m along x, width $b = 0.7366$ m along y and thickness $h = 0.762$ mm. Gunda considered 40 reflections for the image sources method. The dynamic compliance $C(\omega) = u/F(\omega)$, where $u(\omega)$ is the displacement field and $F(\omega)$ is the input force as a function of x/a along $y/b = 0.34$ is shown in Fig. I.30. Based on the result, a very good convergence between the modal decomposition method and the image sources method is observed.

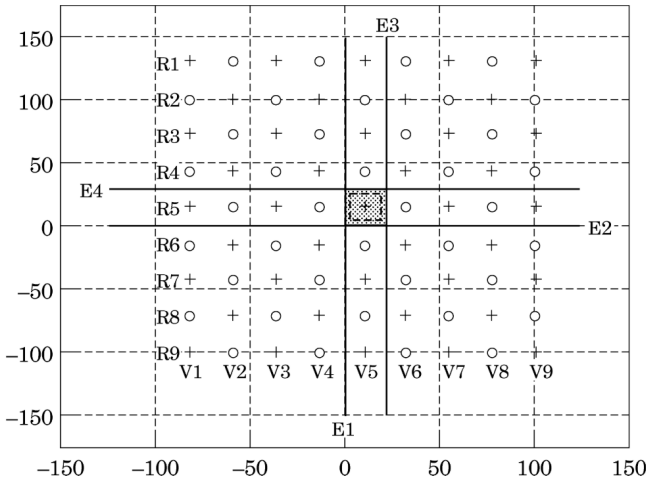

Figure I.29: Infinite plate with positive (+) and negative (0) sources equivalent to a simply supported plate with edges E1, E2, E3 and E4 [37].

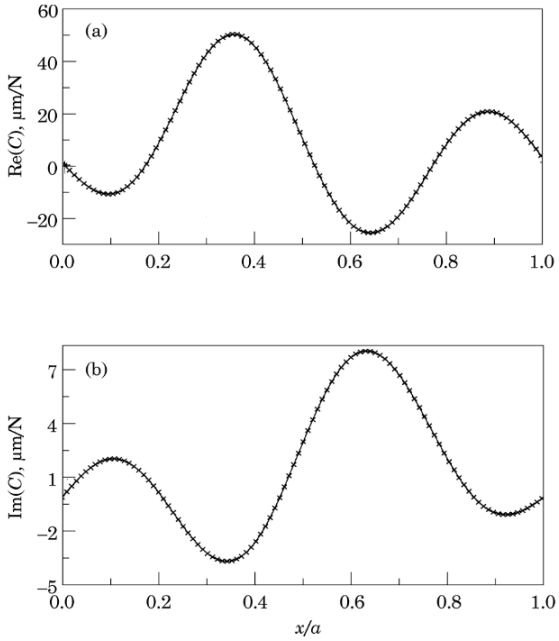

Figure I.30: Dynamic compliance along the line $y/b = 0.34$ due to a unit force at $(0.65a, 0.51b)$. - Image sources method and × Modal analysis. [37].

I. 6. 2 Image source method for arbitrary boundary conditions

The former is limited to the simply supported and to the roller supported boundary conditions. For other boundary conditions, the reflection coefficient involves wave conversion between the propagating and evanescent components of the field and depends on the angle of incidence of the waves and on frequency [28]. Later in 1998 [38], Gunda developed the harmonic Green's function for a thin semi-infinite plate with clamped or free edges by applying corrections to either simply supported or roller supported boundary conditions. Recently, Cuenca et al. [28] introduced an image source method with arbitrary boundary conditions.

The Green's function of the infinite plate G_∞ describes the direct contributions of the source to the displacement field and the incident field on boundaries. To better describe this phenomenon, the Green's function of an infinite plate G_∞ is rather expressed in rectangular coordinates.

For such purpose, an arbitrary oriented coordinates (ξ, μ), where ξ is the axial coordinate, collinear to a given boundary and μ is the transverse coordinate, normal to the boundary (see Fig. I.31). The Green's function G_∞ is represented as a sum of plane waves in rectangular coordinates of the form [28]:

$$G_\infty\left(\xi,\mu,\xi_0,\mu_0;k_f\right)=\frac{\mathrm{i}}{8\pi k_f^2 D}\int_{-\infty}^{+\infty}\mathrm{e}^{\mathrm{i}k_\xi(\xi-\xi_0)}\left(\frac{\mathrm{e}^{\mathrm{i}\sqrt{k_f^2-k_\xi^2}|\mu-\mu_0|}}{\sqrt{k_f^2-k_\xi^2}}+\mathrm{i}\frac{\mathrm{e}^{-\sqrt{k_f^2+k_\xi^2}|\mu-\mu_0|}}{\sqrt{k_f^2+k_\xi^2}}\right)\mathrm{d}k_\xi \quad . \tag{I.62}$$

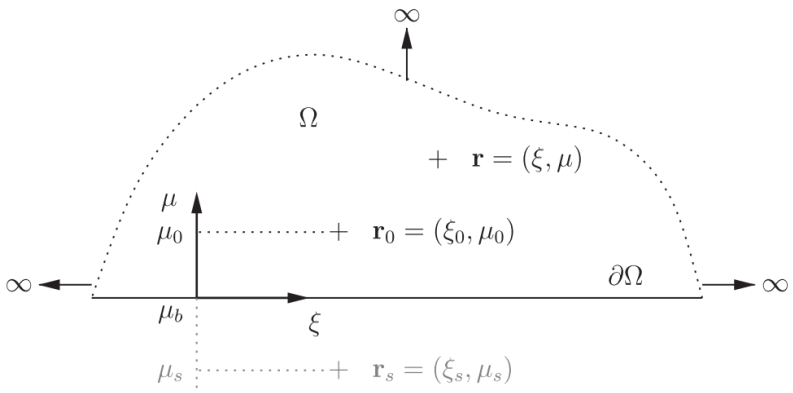

Figure I.31: Schematic presentation of the coordinates. $\mathbf{r_0}$, original source, $\mathbf{r_s}$, image source and $\mathbf{r}$, observation point [28].

Eq. I.62 is obtained using one-dimensional Fourier transform of the equation of motion of an isotropic plate on coordinate ξ [28]. Transverse wavenumbers $k_\mu^{(1)}=\sqrt{k_f^2-k_\xi^2}$ and $k_\mu^{(2)}=\mathrm{i}\sqrt{k_f^2+k_\xi^2}$ as functions of the axial wavenumber k_ξ are shown in Fig. I.32.

The term $e^{\mathrm{i}\sqrt{k_f^2-k_\xi^2}|\mu-\mu_0|}/\sqrt{k_f^2-k_\xi^2}$ is considered a propagating wave for $|k_\xi|<|k_f|$ and an evanescent wave for $|k_\xi|>|k_f|$. Meanwhile, the term $\mathrm{i}e^{-\sqrt{k_f^2+k_\xi^2}|\mu-\mu_0|}/\sqrt{k_f^2+k_\xi^2}$ represents an evanescent wave for all values of k_ξ [28].

For the application of this method, the Green's function G_Ω of the semi-infinite plate is assumed as follow [28]:

$$\begin{cases} D\left(\nabla^4-k_f^4\right)G_\Omega\left(\mathbf{r},\mathbf{r}_0;k_f\right)=\delta\left(\mathbf{r}-\mathbf{r}_0\right), & \mathbf{r}\in\Omega \\ \text{Boundary conditions}, & \mathbf{r}\in\partial\Omega \end{cases} , \tag{I.63}$$

where $\mathbf{r_0}$ is the location of the point source (see Fig. I.31) and the arbitrary boundary conditions are considered linear and homogeneous along the edge. The displacement field

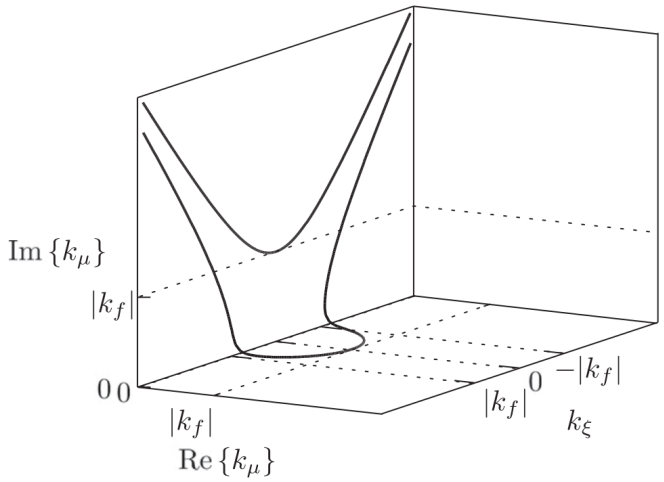

Figure I.32: Transverse wavenumbers as functions of k_ξ. Lower curve, $k_\mu^{(1)} = \sqrt{k_f^2 - k_\xi^2}$ and upper curve, $k_\mu^{(2)} = \mathrm{i}\sqrt{k_f^2 + k_\xi^2}$ [28].

at $\mathbf{r}$ can be expressed as the sum of the Green's function of the infinite plate and the reflected field from the boundary, G_s. This relation writes:

$$G_\Omega(\mathbf{r}, \mathbf{r_0}; k_f) = G_\infty(\mathbf{r}, \mathbf{r_0}; k_f) + G_s(\mathbf{r}, \mathbf{r_s}, \mu_b; k_f) \quad , \tag{I.64}$$

where μ_b describes the location of the boundary along the edge (see Fig. I.31). To determine G_s with arbitrary boundary conditions, the integrand of Eq. I.62 along axis $\mu = \mu_b$, is written as:

$$w_i\left(\xi, \mu, \xi_0, \mu_0, \mu_b; k_f\right) = \mathrm{e}^{\mathrm{i}k_\xi(\xi-\xi_0)}\left(A_0\mathrm{e}^{-\mathrm{i}\sqrt{k_f^2-k_\xi^2}(\mu-\mu_b)} + B_0\mathrm{e}^{\sqrt{k_f^2+k_\xi^2}(\mu-\mu_b)}\right) \quad , \tag{I.65}$$

where

$$A_0 = \frac{\mathrm{i}}{8\pi k_f^2 D}\frac{\mathrm{e}^{-\mathrm{i}\sqrt{k_f^2-k_\xi^2}(\mu_b-\mu_0)}}{\sqrt{k_f^2-k_\xi^2}}, \quad B_0 = \frac{\mathrm{i}}{8\pi k_f^2 D}\frac{\mathrm{i}\mathrm{e}\sqrt{k_f^2+k_\xi^2}(\mu_b-\mu_0)}{\sqrt{k_f^2+k_\xi^2}} \quad . \tag{I.66}$$

Similarly, the reflected wave is written as:

$$w_r\left(\xi, \mu, \xi_0, \mu_0, \mu_b; k_f\right) = \mathrm{e}^{\mathrm{i}k_\xi(\xi-\xi_0)}\left(A_s\mathrm{e}^{-\mathrm{i}\sqrt{k_f^2-k_\xi^2}(\mu-\mu_b)} + B_s\mathrm{e}^{\sqrt{k_f^2+k_\xi^2}(\mu-\mu_b)}\right) \quad , \tag{I.67}$$

where A_s and B_s depend on the boundary conditions. The relation between A_0, B_0, A_s and B_s is given by:

$$\begin{bmatrix} A_s \\ B_s \end{bmatrix} = \mathbf{R}\begin{bmatrix} A_0 \\ B_0 \end{bmatrix} \quad , \tag{I.68}$$

where

$$\mathbf{R}\left(k_\xi, k_f\right) = \begin{bmatrix} R_{pp}\left(k_\xi, k_f\right) & R_{ep}\left(k_\xi, k_f\right) \\ R_{pe}\left(k_\xi, k_f\right) & R_{ee}\left(k_\xi, k_f\right) \end{bmatrix} \quad . \tag{I.69}$$

$\mathbf{R}(k_\xi, k_f)$ is the reflection matrix where (p) and (e) represent the propagating and the evanescent components respectively. The reflected field G_s is the superposition of an infinite number of elementary waves in the form of Eq. I.67. The reflected field is interpreted as the contribution of the image source to the total bending field. This is done by performing the changes of variables $\xi_S = \xi_0$ and $\mu_b - \mu_0 = -(\mu_b - \mu_s)$ [28]. The reflected field G_s can then be described as [28]:

$$
\begin{aligned}
G_S^{(I)}\left(\mathbf{r}, \mathbf{r}_s, \mu_b; k_f\right) = \frac{\mathrm{i}}{8\pi k_f^2 D} \int_{-\infty}^{+\infty} \mathrm{e}^{\mathrm{i}k_\xi(\xi-\xi_s)} \\
\left[\begin{array}{cc} \mathrm{e}^{\mathrm{i}\sqrt{k_f^2-k_\xi^2}(\mu-\mu_b)} & \mathrm{e}^{-\sqrt{k_f^2+k_\xi^2}(\mu-\mu_b)} \end{array}\right]
\left[\begin{array}{cc} R_{pp}\left(k_\xi, k_f\right) & R_{ep}\left(k_\xi, k_f\right) \\ R_{pe}\left(k_\zeta, k_f\right) & R_{ee}\left(k_\xi, k_f\right) \end{array}\right] \\
\left[\begin{array}{c} \dfrac{\mathrm{e}^{\mathrm{i}\sqrt{k_f^2-k_\xi^2}(\mu_b-\mu_s)}}{\sqrt{k_f^2-k_\xi^2}} \\ \mathrm{i}\dfrac{\mathrm{e}^{-\sqrt{k_f^2+k_\xi^2}(\mu_b-\mu_s)}}{\sqrt{k_f^2+k_\xi^2}} \end{array}\right] .
\end{aligned}
\tag{I.70}
$$

The final expression of the Green's function of a semi-infinite plate G_Ω (see Eq. I.64) is given by the sum of the Green's function of infinite plate G_∞ described in Eq. I.62 and the reflected field G_s described in Eq. I.63.

The present formulation introduced by Cuenca [28] represents the generality of the first order image source method. Comparing to the application of the image source method introduced by Gunda [37, 38], this approach includes an explicit dependence on the location of the boundary μ_b which is important in order to take into account the coupling between the incident field and the reflected field [28]. The corresponding reflection matrices for a simply supported, roller, clamped and free edge is presented in Tab. I.6.

Boundary conditions		Reflection matrix $\mathbf{R}(\mathbf{k_\xi}, \mathbf{k_f})$
Simply supported	$\begin{cases} w(\xi,\mu_b)=0 \\ M_\mu(\xi,\mu_b)=0 \end{cases}$	$\begin{bmatrix} -1 & 0 \\ 0 & -1 \end{bmatrix}$
Roller	$\begin{cases} \frac{\partial w}{\partial \mu}(\xi,\mu_b)=0 \\ V_\mu(\xi,\mu_b)=0 \end{cases}$	$\begin{bmatrix} 1 & 0 \\ 0 & 1 \end{bmatrix}$
Clamped	$\begin{cases} w(\xi,\mu_b)=0 \\ \frac{\partial w}{\partial \mu}(\xi,\mu_b)=0 \end{cases}$	$\begin{bmatrix} -\frac{\sqrt{k_f^2+k_\xi^2}-\mathrm{i}\sqrt{k_f^2-k_\xi^2}}{\sqrt{k_f^2+k_\xi^2}+\mathrm{i}\sqrt{k_f^2-k_\xi^2}} & \frac{2\sqrt{k_f^2+k_\xi^2}}{\sqrt{k_f^2+k_\xi^2}+\mathrm{i}\sqrt{k_f^2-k_\xi^2}} \\ \frac{2\mathrm{i}\sqrt{k_f^2+k_\xi^2}}{\sqrt{k_f^2+k_\xi^2}+\mathrm{i}\sqrt{k_f^2-k_\xi^2}} & \frac{\sqrt{k_f^2+k_\xi^2}-\mathrm{i}\sqrt{k_f^2-k_\xi^2}}{\sqrt{k_f^2+k_\xi^2}+\mathrm{i}\sqrt{k_f^2-k_\xi^2}} \end{bmatrix}$
Free	$\begin{cases} M_\mu(\xi,\mu_b)=0 \\ V_\mu(\xi,\mu_b)=0 \end{cases}$	$\begin{bmatrix} \frac{ad-bc}{ad+bc} & \frac{-2ac}{ad+bc} \\ \frac{-2bd}{ad+bc} & -\frac{ad-bc}{ad+bc} \end{bmatrix}$ $a = k_f^2 + (1-\nu)k_\xi^2$ $b = -k_f^2 + (1-\nu)k_\xi^2$ $c = -\sqrt{k_f^2+k_\xi^2}(k_f^2-(1-\nu)k_\xi^2)$ $d = \mathrm{i}\sqrt{k_f^2-k_\xi^2}(k_f^2+(1-\nu)k_\xi^2)$

Table I.6: Boundary conditions and reflection matrices for a simply supported, roller, clamped or free edge [28].

Second and subsequent wave reflections on the boundaries

In the previous section, the contributions of the image source of first order is described. However, the contribution of an image source of second order and subsequent cannot be derived directly using the same procedure because an individual plane wave resulting from the first reflection cannot be written in the form of Eq. I.67 in the local coordinate system of another edge where a second reflection may take place [28].

Here, an approximation is proposed by neglecting the evanescent components of Eq. I.67 because the wavelength is considered short compared to the plate dimensions which is true only in the high frequency range. The approximation writes [28]:

$$G_s^{(II)}\left(\mathbf{r},\mathbf{r}_s;k_f\right) = V\left(\mathbf{r},\mathbf{r}_s\right)\frac{\mathrm{i}}{8\pi k_f^2 D}\int_{-|k_f|}^{|k_f|} \mathrm{e}^{\mathrm{i}k_\xi(\xi-\xi_s)} A_{pp}^{(s)}\left(k_\xi,k_f\right)\frac{\mathrm{e}^{\mathrm{i}\sqrt{k_f^2-k_\xi^2}(\mu-\mu_s)}}{\sqrt{k_f^2-k_\xi^2}}\,\mathrm{d}k_\xi \quad , \quad \text{(I.71)}$$

where $V(\mathbf{r},\mathbf{r_s})$ is the validity conditions that is equal to 1 in the domain of the application and 0 elsewhere. $A_{pp}^{(s)}(\theta)$ is the amplitude weight of the image source s [28]. The amplitude weight $A_{pp}^{(s)}(\theta)$ is the product scalar of the reflection coefficients R_{pp} of the edges that contribute in the construction of image sources s.

Approximated Green's function

Finally, the approximated Green's function of the polygonal plate can be described as a linear combination of the original source, the first order image sources and the second order image sources of the form:

$$\widetilde{G_\Omega}(\mathbf{r}, \mathbf{r_0}; k_f) = G_\infty(\mathbf{r}, \mathbf{r_0}; k_f) + \sum_{s=1}^{N_v} G_S^{(I)}(\mathbf{r}, \mathbf{r_s}, \mu_b^{(s)}; k_f) + \sum_{s=N_v+1}^{\infty} G_s^{(II)}(\mathbf{r}, \mathbf{r_s}; k_f) \quad , \quad \text{(I.72)}$$

where N_v is the number of vertices or edges of the plate.

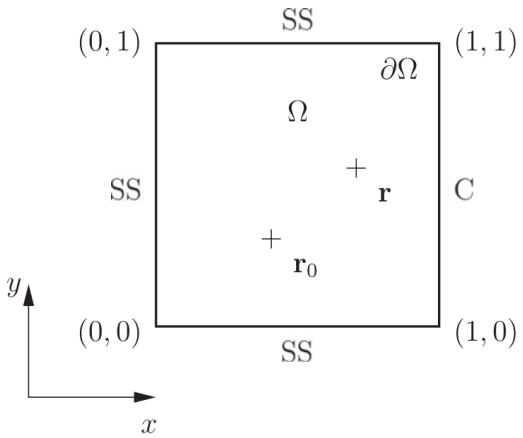

Figure I.33: Square plate with three simply supported (SS) edges and one clamped (C) edge [28].

The validity of the method is tested on a Levy-type plate in which the analytical harmonic response of this panel is known analytically [79]. The schematic presentation and the different boundary conditions of the edges is shown Fig. I.33. A square steel panel with a length $L = 1$ m (Density $\rho = 7850$ kg/m^3, Young's modulus E = 210 GPa, Poisson's coefficient ν= 0.33 and damping η_{skin}=7%) is considered with simply supported edges along $y = 0$, $y = L$ and $x = 0$, and a clamped edge along $x = L$. The reference solution is computed analytically by using a modal decomposition method and compared to the proposed method with 488 sources contributions.

Figs. I.34a-b show the normal displacement of the exact solution and the image source method at 3000 Hz. Fig. I.34c-d show the displacement field on vertical lines l_1 to l_5. Fig I.34h shows the euclidean normalized error between the exact solution and the proposed method. The results show good correlation in the whole plate except near the clamped edge within a distance to half of the wavelength. This error is due to the evanescent waves which are neglected for sources of second and higher orders.

This method has been successfully developed to characterize the isotropic structures with arbitrary polygonal plates by using a generalised image source method. The advantage of this method is that the wave propagation, geometry and boundary conditions can be treated separately. To the best of our knowledge, the application of the image source method is limited to polygonal isotropic structures. The application of this method to non-isotropic structures may be one of the domain of interest.

The potential of the image source method in combination with the Green's function-based model correlation (GFC) method will be studied in Chapter IV.

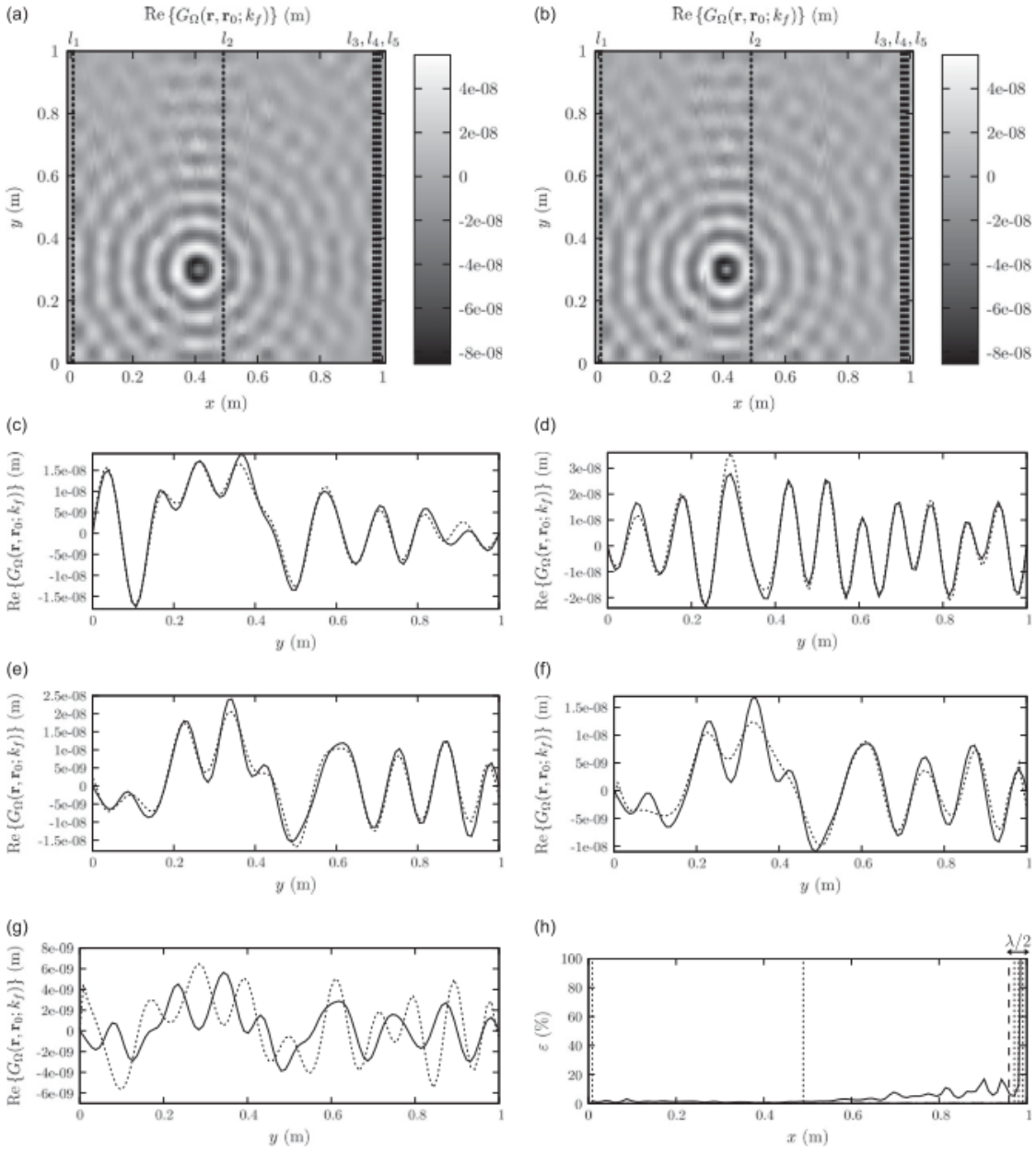

Figure I.34: Amplitude of Green's function for the square plate. (a) Exact; (b) Image sources method; (c)-(g) displacement field on vertical lines l_1 to l_5; ⁻, exact; ..., Image sources method; (h) Error as function of abscissa [28].

I. 6. 3 A wave fitting approach using an image source method

Roozen et al. [75] presented a new wave fitting approach to estimate the material properties of thin isotropic structures. The proposed method constructs the harmonic displacement field model by combining the Green's function of an infinite plate described in Eq. I.30 and its image sources which represent the successive reflections of waves on the boundaries [27]. The principle of the method is detailed in this section.

The response of the harmonic displacement field is approximated by means of a linear combination of image sources of the form [75]:

$$\tilde{w}(x_j, y_j, \omega) = \sum_{n=1}^{N} \alpha_n(\omega)\phi_n(x_j, y_j) \quad , \tag{I.73}$$

where α_n is the strength of each image source and ϕ_n the Green's function of an infinite plate:

$$\phi_n(x_j, y_j) = G_\infty(x_j - x_0(n), y_j - y_0(n)) \quad , \tag{I.74}$$

where $x_0(n)$ and $y_0(n)$ are the x and y-locations of the n-th image source. Considering all M measurement points on the plate and N image sources, Eq. I.73 can be written in matrix notation of the form:

$$\tilde{\mathbf{w}} = \mathbf{\Phi}\alpha \quad . \tag{I.75}$$

$\tilde{\mathbf{w}}$ is a vector representing the projected displacement $\tilde{w}(x_j, y_j, \omega)$, $\mathbf{\Phi}$ is a matrix representing the vectors of the image source Green's functions, ϕ_n and α is a vector representing the contribution strengths $\alpha_n(\omega)$. The vector of contribution strengths α can be determined via a regularized pseudo-inverse approach and the equation writes [75]:

$$\alpha = \text{argmin}(||\mathbf{w} - \mathbf{\Phi}\alpha||^2 + \lambda^2||\alpha||^2) \quad , \tag{I.76}$$

where λ is the Tikhonov regularisation term determined by a Bayesian characterization [3, 68, 92].

Roozen applied the method numerically to an isotropic rectangular plate with free edges and the structural loss factor of the panel is set at $\eta = 5\%$. The convergence study was also conducted with different number of images sources as shown in Fig. I.35. The projected fields, $\tilde{\mathbf{w}}$, for a frequency of 15 kHz are presented in Fig. I.35a-d for a varying number of image sources. For the given geometry and the boundary conditions, nine sources are enough to describe the vibrational of a point excited plate.

Furthermore, Roozen applied the method experimentally to a sandwich isotropic steel panel with a polymer core. The experimental set-up of the sandwich panel is shown in Fig. I.36. The estimation of the dispersion curve and the damping properties, is calculated in a least squares senses between the measured field and the projected field with nine sources. Fig. I.37 shows the result on the estimation of the wavenumber and the damping loss factor.

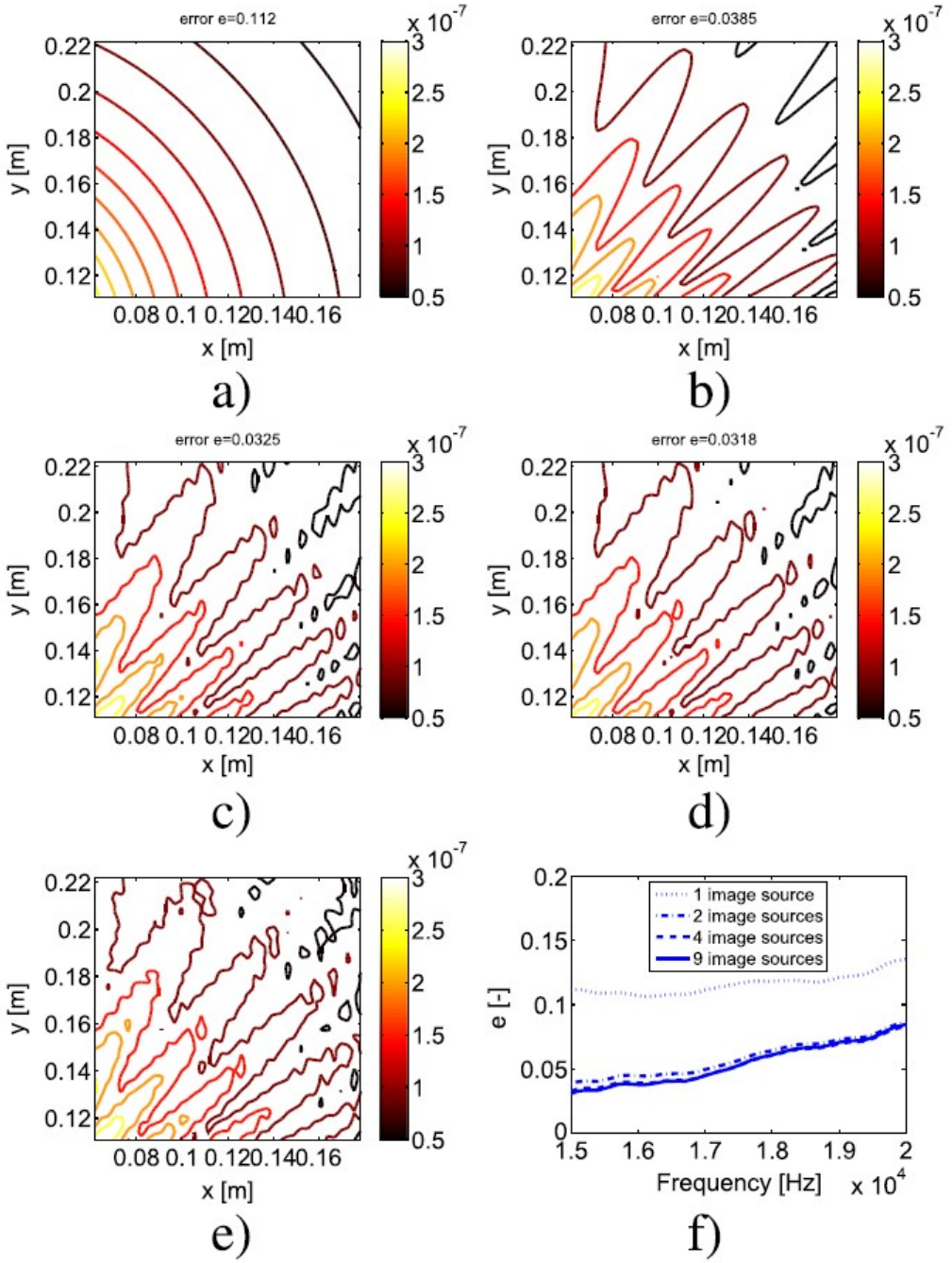

Figure I.35: Contour lines of the absolute vibration levels of a free edges panel at 15 kHz. a) 1 source. b) 2 sources. c) 4 sources. d) 9 sources and e) Measured harmonic field from the numerical simulations. f) Error e as a function of the frequency [75].

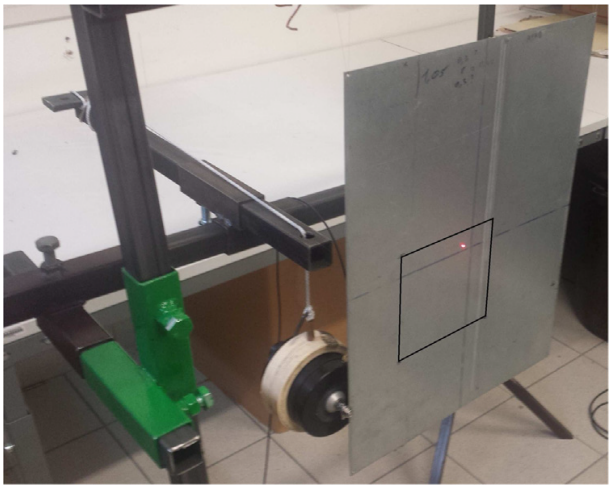

Figure I.36: Experimental set-up of the image source method. The black line on the plate indicates the measurement area [75].

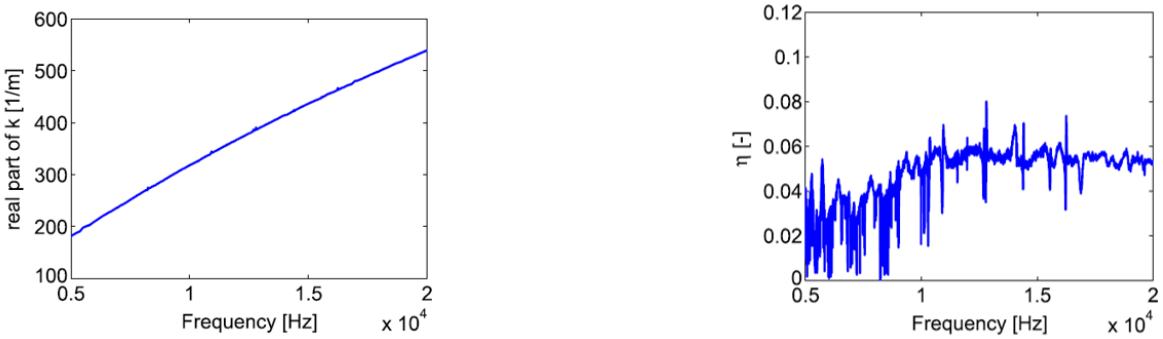

Figure I.37: The estimation of the material properties. Left: The real part of the wavenumber. Right: The damping loss factor [75].

I.7 Discrete general laminate model

Finally as the discrete general laminate model (GLM) [36] will be used throughout this thesis as a reference for validation of the estimated wavenumber and damping, a brief description is given here.

This approach assumes each layer as a thick laminate with orthotropic orientation, rotational inertia and transversal shearing, membrane and bending deformations. The equation of motion is developed following a wave approach based on discrete layer description.

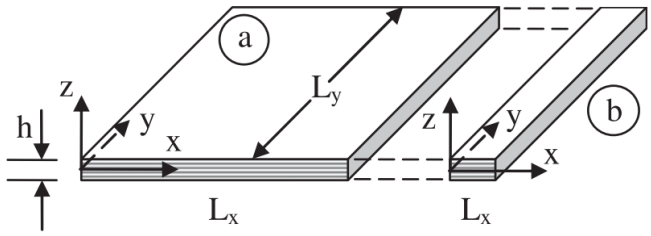

Figure I.38: Global geometrical configuration. (a) Planar laminated composite panel and (b) planar laminated composite beam [36].

The geometry of the planar composite panel is shown in Fig. I.38. This method assumes membrane and bending displacements and rotations of each layer. Thus, the displacement field of the i-th layer of the panel is defined as:

$$\begin{cases} u^i(x,y,z) = u_0^i(x,y) + z\varphi_x^i(x,y) & , \\ v^i(x,y,z) = v_0^i(x,y) + z\varphi_y^i(x,y) & , \\ w^i(x,y,z) = w_0^i(x,y) & , \end{cases} \tag{I.77}$$

where $u^i(x,y,z)$, $v^i(x,y,z)$ and $w^i(x,y,z)$ are the displacement along x-direction, y-direction and z-direction respectively. $\varphi_x^i(x,y)$ and $\varphi_y^i(x,y)$ are the rotations along z-direction and y-direction respectively.

For the i-th layer, five equilibrium equations are defined as:

$$\begin{aligned} &N_{x,x}^i + N_{xy,y}^i + F_x^i - F_x^{i-1} = m_s^i u_{,tt}^i + I_{z2}^i \varphi_{x,tt}^i \quad , \\ &N_{xy,x}^i + N_{y,y}^i + F_y^i - F_y^{i-1} = m_s^i v_{,tt}^i + I_{z2}^i \varphi_{y,tt}^i \quad , \\ &Q_{x,x}^i + Q_{y,y}^i + F_z^i - F_z^{i-1} = m_s^i w_{,tt}^i \quad , \\ &M_{x,x}^i + M_{xy,y}^i - Q_x^i + z^i F_x^i - z^{i-1} F_x^{i-1} = I_z^i \varphi_{x,tt}^i + I_{z2}^i u_{,tt}^i \quad , \\ &M_{xy,x}^i + M_{y,y}^i - Q_y^i + z^i F_y^i - z^{i-1} F_y^{i-1} = I_z^i \varphi_{y,tt}^i + I_{z2}^i v_{,tt}^i \quad , \end{aligned} \tag{I.78}$$

where $Q_{x,x}^i$ and $Q_{y,y}^i$ are the transverse shear stress, $N_{x,x}^i$, $N_{y,y}^i$ and $N_{xy,x}^i$ are the in-plane stress and $M_{x,x}^i$, $M_{xy,y}^i$, $M_{xy,x}^i$ and $M_{y,y}^i$ are the stress moments. The rotational inertia, the in-plane, the bending, the transverse shearing effects and the orthotropic ply directions are accounted for in each layer. The resulting dynamic equilibrium of Eq. I.78 is then regrouped in two vectors: a displacement-rotation vector $\{\mathbf{U}\}$ and an interlayer forces vector $\{\mathbf{F}\}$:

$$\begin{aligned}\{\mathbf{U}\} &= \left\{u^1; v^1; w^1; \varphi_x^1; \varphi_y^1; u^2; v^2; w^2; \varphi_x^2; \varphi_y^2; \cdots u^N; v^N; w^N; \varphi_x^N; \varphi_y^N\right\}^T \quad , \\ \{\mathbf{F}\} &= \left\{F_x^1; F_y^1; F_z^1; F_x^2; F_y^2; F_z^2; \cdots F_x^{N-1}; F_y^{N-1}; F_z^{N-1}\right\}^T \quad .\end{aligned} \tag{I.79}$$

To solve for the dispersion relations [36], the system of dynamic equilibrium equations is expressed in term of a hybrid displacement-force vector $\langle \mathbf{e} \rangle$ defined as:

$$\langle \mathbf{e} \rangle = \begin{Bmatrix} U \\ F \end{Bmatrix} \quad . \tag{I.80}$$

Assuming a harmonic solution $\langle \mathbf{e} \rangle = e^{(\mathrm{i}k_x x + \mathrm{i}k_y y - \mathrm{i}\omega t)}$, a generalized complex polynomial eigenvalue problem is defined as:

$$(\mathbf{k_c^2}[\mathbf{A_2}] - \mathrm{i}\mathbf{k_c}[\mathbf{A_1}] - [\mathbf{A_0}])\{e\} = 0 \quad , \tag{I.81}$$

where $k_c = \sqrt{k_x^2 + k_y^2}$ and $[\mathbf{A_0}]$, $[\mathbf{A_1}]$ and $[\mathbf{A_2}]$ are real square matrices of dimensions $5N + 3(N-1)$, where N is the number of layers. Assuming $\lambda = \mathrm{i}\mathbf{k_c}$, Eq. I.81 can be rewritten into a first order system in the form [36]:

$$\left(\lambda \begin{bmatrix} \mathbf{A}_1 & \mathbf{A}_2 \\ \mathbf{A}_2 & \mathbf{0} \end{bmatrix} - \begin{bmatrix} -\mathbf{A}_0 & \mathbf{0} \\ \mathbf{0} & \mathbf{A}_2 \end{bmatrix}\right) \begin{Bmatrix} \mathbf{e} \\ \lambda \mathbf{e} \end{Bmatrix} = \begin{Bmatrix} \mathbf{0} \\ \mathbf{0} \end{Bmatrix}. \tag{I.82}$$

Eq. I.82 represents the dispersion relations of the laminated composite structure. The corresponding natural frequencies ω_{mn} are obtained from the solution of Eq. I.81 in the form:

$$(\mathbf{k_{mn}^2}[\mathbf{A_2}] - \mathrm{i}\mathbf{k_{mn}}[\mathbf{A_1}] - [\mathbf{A_0}])\{e\} = \omega_{mn}^2[\mathbf{A_{02}}]\{e\} \quad , \tag{I.83}$$

$$k_{mn} = \frac{\lambda(m, n, L_x/L_y)}{L_x} \quad , \tag{I.84}$$

where λ_{mn} is the frequency dependent boundary condition for each combination (m, n) and side dimensions ratio (L_x, L_y). $[\mathbf{A_1}]$, $[\mathbf{A_2}]$, $[\mathbf{A_{01}}]$ and $[\mathbf{A_{02}}]$ are real square matrices of dimensions $5N + 3(N-1)$ with $[\mathbf{A_0}] = [\mathbf{A_{01}}] - \omega[\mathbf{A_{02}}]$.

Ghinet and Atalla [36] use the modal strain energy U_n to identify the damping loss factor of sandwich structures in function of the frequency and the wave heading angle. The equivalent loss factor of a panel or a beam with N layers is defined as:

$$\begin{aligned}\eta_n &= \frac{1}{\pi}\int_0^\pi \frac{\sum_{k=1}^{N_{\mathrm{lay}}} \eta_k U_n^k}{U_n} d\varphi \quad , \\ &= \frac{1}{\pi}\int_0^\pi \frac{\sum_{k=1}^{N_{\mathrm{lay}}} \eta_k \mathbf{v_n}^{\mathrm{T}} \mathcal{R} \left[\lambda_{\mathbf{n}} \mathbf{A} - \mathbf{B}\right] \mathbf{v_n}}{\mathbf{v_n}^{\mathrm{T}} \mathcal{R} \left[\lambda_{\mathbf{n}} \mathbf{A} - \mathbf{B}\right] \mathbf{v_n}} d\varphi \quad ,\end{aligned} \tag{I.85}$$

where

$$\mathbf{A} = \begin{bmatrix} \mathbf{A_1} & \mathbf{A_2} \\ \mathbf{A_2} & \mathbf{0} \end{bmatrix}; \quad \mathbf{B} = \begin{bmatrix} \mathbf{A_{01}} & \mathbf{0} \\ \mathbf{0} & \mathbf{A_2} \end{bmatrix}; \quad \text{and} \quad \mathbf{v_n} = \begin{Bmatrix} \mathbf{e} \\ \lambda \mathbf{e} \end{Bmatrix} \quad . \tag{I.86}$$

Eq. I.86 calculates the average damping loss factor over half wavenumber space with respect to the heading direction φ.

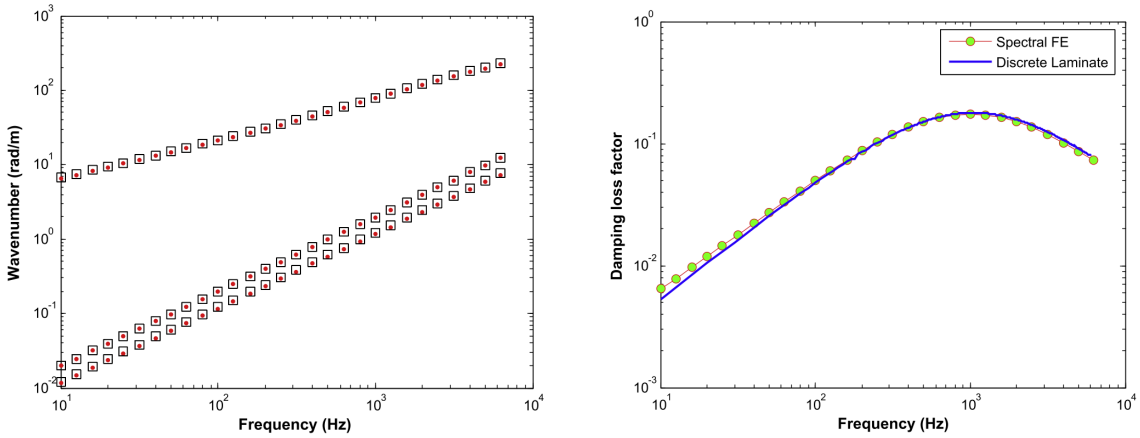

Figure I.39: Left: Propagating wavenumber solutions of the sandwich beam. (· · ·) 3D composite Spectral Finite Elements approach. [77]; (□□□) Discrete Laminate approach. Right: Damping loss factor of the sandwich beam [36].

The method has been applied to a sandwich beam to determine the wavenumber and the damping loss factor. The characteristic of the beam is defined in Table. I.7.

	Skins		Core	
Young's modulus (Pa)	$E_1 = E_3$	210 x 10^9	E_2	15.7642 x 10^6
Shear modulus (Pa)	$G_1 = G_3$	80.77 x 10^9	G_2	1.88 x 10^6
Density (kg/m^3)	$\rho_1 = \rho_3$	7850	ρ_2	1000
Loss factor	$\eta_1 = \eta_3$	0.001	η_2	0.5

Table I.7: Material properties of the sandwich beam: $L_x = 0.25$ m; $L_y = 0.02$ m; $h_1 = h_3 = 0.449$ mm; $h_2 = 0.035$ mm [36].

The wavenumber and the damping loss factor results are plotted in Fig. I.39. Excellent agreement is observed between the analytical discrete laminate model and the spectral finite elements approaches [77].

I. 8 Conclusion of the chapter

This chapter presented some of the characterization methods available in the open literature and methods to estimate the damping loss factor of vibrating structures. The advantages, the drawbacks and the results of each method have been briefly discussed. The analytical solution based on the discrete general laminate model (GLM) has been presented at the end of the chapter. This solution will be used as a reference for validation of the estimate wavenumber and damping.

To conclude, the identification of the real part of the wavenumber is not an issue. It can be obtained using various methods such as the force analysis technique (FAT), the discrete Fourier transform (DFT), the inhomogeneous wave correlation (IWC) method, the Green's function based correlation. The latter can be even enhanced using the image source method.

However few studies are presented to discuss the effect of important parameters such as the source location, the size of the observation window and the averaging of the damping over heading angles. In addition, robust estimation of the damping loss factor related to the imaginary part of the wavenumber remains an open issue with the majority of described characterization methods.

In consequence, the present work will revisit the IWC method in Chapter II, the Green's function based-model correlation (GFC) method in Chapter III and the GFC method with the image source method (GFC-ISM) in Chapter IV to address explicitly these remaining issues and in particular, robust estimation of the damping loss factor.

Chapter II

An enhanced formulation of the inhomogeneous wave correlation method

The classical IWC method which is based on the maximization of the correlation between the measured displacement field and the inhomogeneous wave is investigated in this chapter. An enhanced formulation of the Inhomogeneous Wave Correlation (IWC) method that improves the estimation of the damping loss factor is introduced. The proposed method takes into account the exponential decay with distance from the excitation point in the inhomogeneous wave formulation. The validity of the proposed method is investigated numerically using the Finite Element Method (FEM) on several panels: an isotropic aluminium panel, a sandwich aluminium panel with a viscoelastic core and an anisotropic 7 layers epoxy resin panel. In addition, the effect of the observation window and the effect of the excitation location are also discussed.

II.1 Introduction

In the open literature, the development of a robust method able to estimate the wavenumber and in particular, the damping loss factor of planar complex structures remains very challenging. The modal approach is broadly used to characterize the material properties in the low frequency range. In the mid and the high frequency range, this approach is no longer applicable due to the high modal density and the high modal overlap of the vibrating structure.

The inverse wave approach was first introduced by McDaniel et al. [61, 62] to estimate the flexural wavenumber and the damping loss factor of one-dimensional structures. Berthaut et al. [7] extended the method by developing an Inhomogeneous Wave Correlation (IWC) method to identify the wavenumber as a function of the wave heading angle for two-dimensional structures. The method is based on the maximization of the correlation between the measured displacement field and plane waves of the form $e^{\pm ik(\theta)(x\cos\theta+y\sin\theta)}$.

The method has been applied to complex structures such as a stiffened panel [42, 43], an orthotropic sandwich carbon fiber with honeycomb core [21] and a plate with distributed resonators [87, 84]. Cherif et al. [21] applied the IWC method to estimate the flexural wavenumber and the damping loss of orthotropic structures from a displacement field measurement.

The ability of the classical IWC method to predict precisely the wavenumber of complex structures is proven. However, the estimation of the damping loss factor remains very difficult due to the nature of the plane wave itself. In fact, the classical formulation of the IWC method neglects the effects of the wave propagation around the excitation point. The method considers that the observation field is far from the excitation point and the wave propagation is approximated by plane waves. In reality, the effect of the excitation is not negligible especially when one considers the excitation point in the observation window.

In fact, the presence of a point load excitation in the observation window provides a very important impact especially on the estimation of the damping loss factor. In this chapter, an enhanced formulation of the inhomogeneous wave that explicitly accounts for the exponential decay of the wave amplitude with the distance from the source is introduced to overcome this limitation. The proposed method improves the estimation of the damping loss factor. The performance of the method is investigated numerically using

the Finite Element Method (FEM) on several flat panels. The results are compared with the classical IWC method and with a reference solution based on the general laminate model [36].

In Section II. 2, the classical IWC method is described and the variant formulation is introduced. The numerical validation on three different panels: 1) an isotropic aluminium panel ; 2) a sandwich aluminium panel with a viscoelastic core; and 3) an anisotropic 7 layers epoxy panel; with a fixed excitation point is described in Section II. 3.

In Section II. 4, the precision of the method by changing the observation window size is investigated on an isotropic aluminium panel and in Section II. 5, the effect of different excitation location is illustrated on an isotropic aluminium panel and an anisotropic 7 layers epoxy panel.

II. 2 Theory

An excitation point **O** with coordinates (x_0, y_0) and an arbitrary observation point $\mathbf{M_i}$ with the coordinates (x_i, y_i) are defined as shown. The vector between these two points is defined as:

$$\mathbf{OM_i} = R\cos(\theta)\,\mathbf{x} + R\sin(\theta)\,\mathbf{y} \quad , \tag{II.1}$$

where R is the distance between points O and M_i and θ is the angle between the vector $\mathbf{OM_i}$ and the x-axis. Fig. II.1 shows the schematic presentation of the problem.

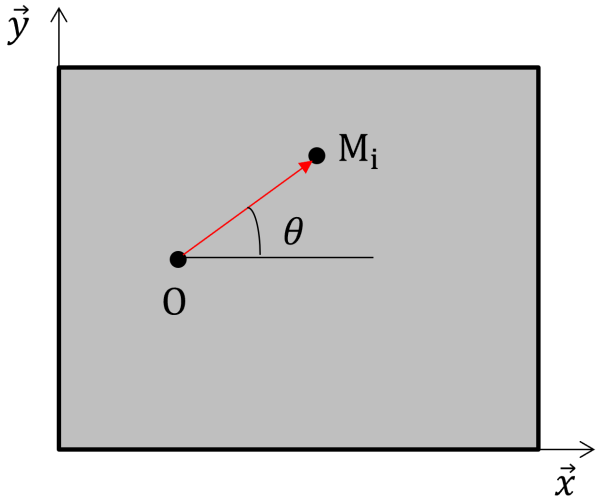

Figure II.1: Schematic presentation of the plate with an excitation point **O** and an arbitrary observation point $\mathbf{M_i}$.

The inhomogeneous wave with a time-harmonic convention of $e^{-i\omega t}$ is written as:

$$\sigma_{k,\gamma,\theta}(x_i, y_i) = e^{\mathbf{ik}.(1+i\gamma).\mathbf{OM_i}} \quad , \tag{II.2}$$

where $\mathbf{k}$ is the wavenumber vector and γ is the attenuation factor. The illustration of the inhomogeneous wave subject to an excitation at $x_0 = 0.3$ m in the xz plane using Eq. II.2 is shown in Fig. II.2a. Implementing naively Eq. II.2, the wave amplitude decreases in the positive direction from the excitation point and increases in the negative direction from the excitation point.

To correctly account for damping, it is better to represent explicitly the associated exponential decay of the wave amplitude with distance from the source as:

$$\widetilde{\sigma}_{k,\gamma,\theta}(x_i, y_i) = e^{\mathrm{i}.\mathbf{k}.\mathbf{OM_i}} e^{-|\mathbf{k}.\gamma.\mathbf{OM_i}|} \quad . \tag{II.3}$$

The relationship between the attenuation constant and the damping loss factor depends on the type of waves [24] and is discussed in Section I. 4.

The illustration of the wave propagation using this variant formulation is shown in Fig. II.2b. The wave amplitude decreases exponentially in both positive and negative directions from the excitation point at $x = 0.3$ m. The main objective of introducing this formulation is to improve the estimation of the damping loss factor in the presence of the excitation point in the observation window. Note that both formulations Eqs. II.2 and II.3 provide similar wave propagation results if the excitation point is outside of the observation window, as the wave model is identical.

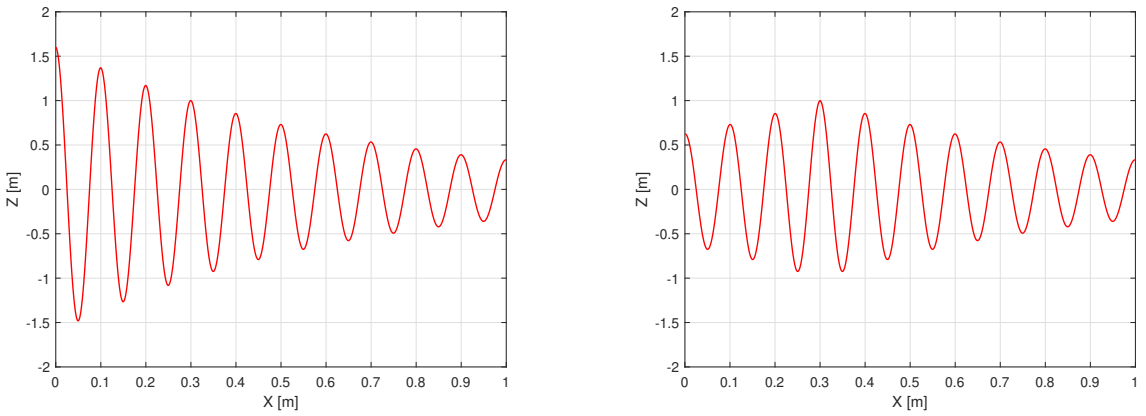

(a) The classical inhomogeneous wave. (b) The enhanced inhomogeneous wave.

Figure II.2: The comparison of the two different formulation of the inhomogeneous waves with an excitation at $x_0 = 0.3$m and $\gamma = 0.25$.

For the application of the method, the enhanced formulation of the inhomogeneous wave $\widetilde{\sigma}^*_{k,\gamma,\theta}(x_i, y_i)$ (see Eq. II.3) is correlated to the measured displacement field $\hat{w}(x_i, y_i)$ by using the correlation function described in Section I. 3. 3. The damping loss factor is determined using Eq. I.51 and the average damping loss factor is calculated using Eq. I.56.

II. 3 Numerical validation with a fixed excitation point

For the isotropic aluminium panel and the sandwich aluminium with a viscoelastic core, the simulations of the panels are done using an in-house finite element software with solid 20-node hexahedron (HEXA20) elements [69, 8, 4]. For the 7 layers epoxy resin panel, the simulations are done with ZPST shell elements [16, 92, 17, 51, 80].

All the panels are subjected to a mechanical point load excitation at $x_0 = 0.2$ m and $y_0 = 0.4$ m. The calculation area of the correlation factor in Eq. I.25 is reduced by 5 cm from each boundary to minimize the effect waves generated by the reflection at boundaries. The schematic presentation of the panel is shown in Fig. II.3.

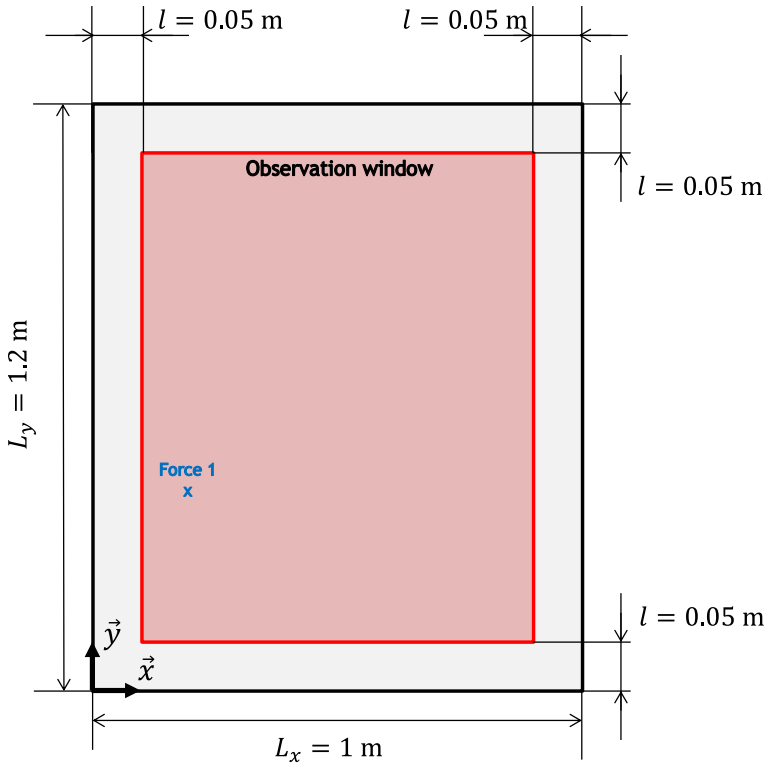

Figure II.3: Schematic presentation of the panel.

II. 3. 1 Isotropic aluminium panel

The method is first applied to a 1 m × 1.2 m isotropic aluminium panel (Density ρ = 2796 kg/m^3, Young's modulus E = 69 GPa, Poisson's coefficient ν= 0.33 and damping η=2%, 5%).

2% structural damping

The IWC wavenumber maps at 6100 HZ of both classical IWC method and enhanced IWC method are shown in Fig. II.4a-b, respectively. Both maps are identical because

based on Eq. II.2 and Eq. II.3, the real part of wavenumber remains the same for both formulations. Based on the maps, the isotropic behavior of the panel is clearly observed.

The dispersion curves obtained from both classical and enhanced IWC method are shown in Fig. II.5. The results show a very good agreement compared to the analytical solution based on the thin plate theory.

The damping loss factor estimated using the classical and the enhanced IWC method are shown in Fig. II.6. The classical IWC method overestimates the damping loss factor on the entire frequency range. The enhanced method still depicts discrepancies compared to the theoretical value but shows a better agreement.

5% structural damping

The IWC wavenumber maps at 1850 Hz and 6100 Hz of the enhanced IWC method are shown in Fig. II.7a-b, respectively. At 1850 Hz, the isotropic behavior is clearly visible. At 6100 Hz, the amplitude of the maximum varies in function of the angle. The position of the excitation coordinates generates a privileged direction of the wave propagation and is well observed in the positive k_x area in this case.

The dispersion curves obtained from both classical and enhanced IWC method are shown in Fig. II.5. The results show a very good agreement compared to the analytical solution.

The damping loss factor estimated using the classical and the enhanced IWC method are shown in Fig. II.9. The classical IWC method underestimates the damping loss factor over the entire frequency range. For the enhanced IWC method, the damping loss factor shows a better agreement compared to the analytical solution above 3000 Hz. Below, the estimation is still not accurate due to the modal behavior of the displacement field.

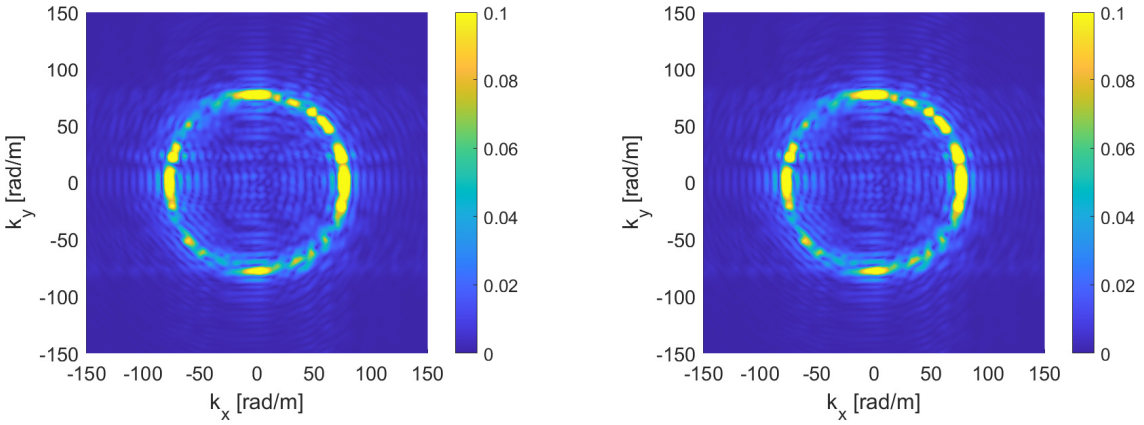

(a) Classical IWC method.

(b) Enhanced IWC method.

Figure II.4: IWC wavenumber maps of the numerical isotropic aluminium panel at 6100 Hz with 2% structural damping.

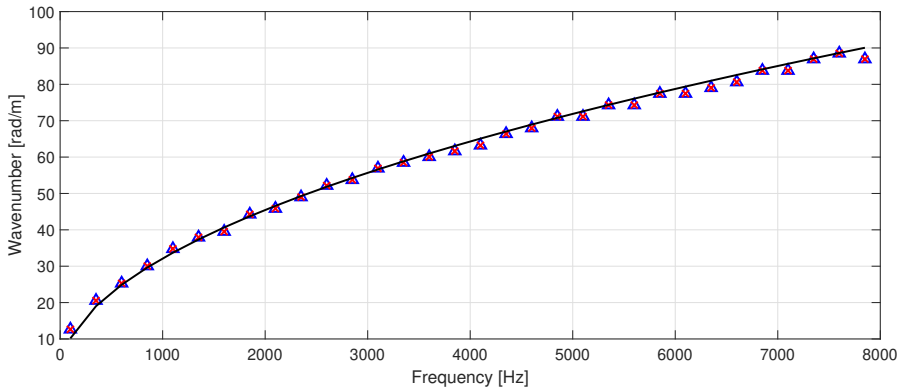

Figure II.5: Comparison of the dispersion curve of the isotropic aluminium panel with 2% structural damping. – analytical, △ classical IWC method and × enhanced IWC method.

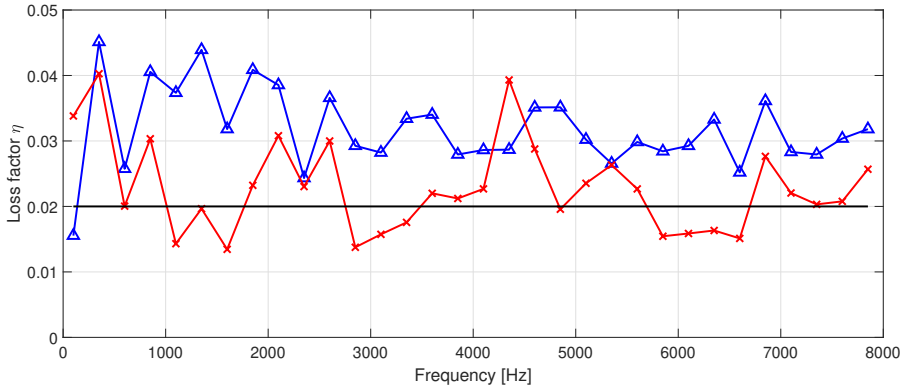

Figure II.6: Comparison of the dispersion curve of the isotropic aluminium panel with 2% structural damping. – exact damping, △ classical IWC method and × enhanced IWC method.

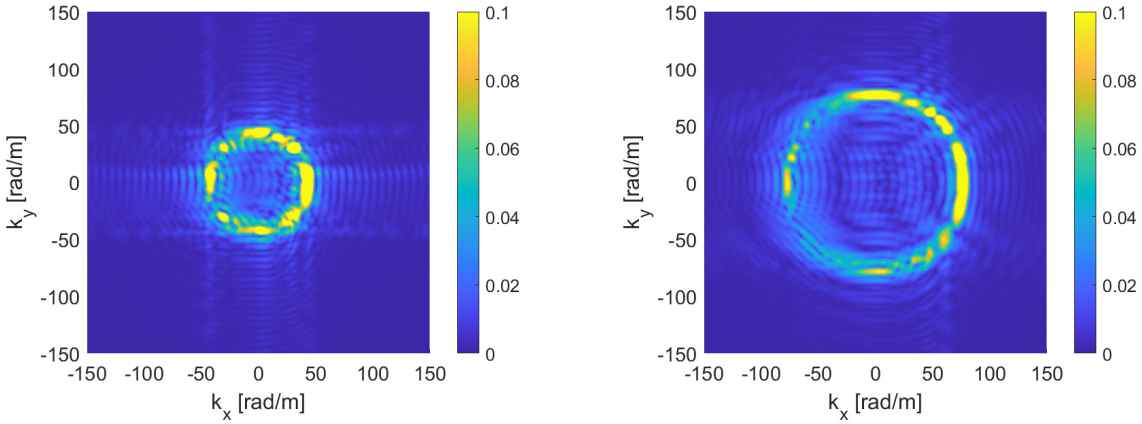

(a) 1850 Hz. (b) 6100 Hz.

Figure II.7: IWC wavenumber maps of the numerical isotropic aluminium panel at 1850 Hz and 6100 Hz with 5% structural damping.

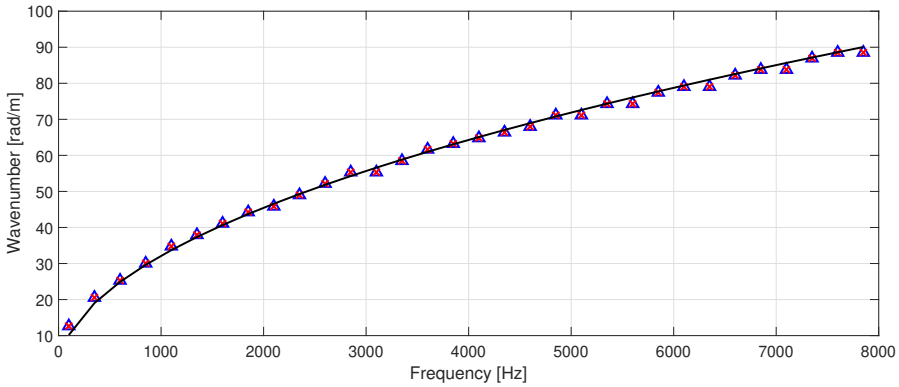

Figure II.8: Comparison of the dispersion curve of the isotropic aluminium panel with 5% structural damping. – analytical, △ classical IWC method and × enhanced IWC method.

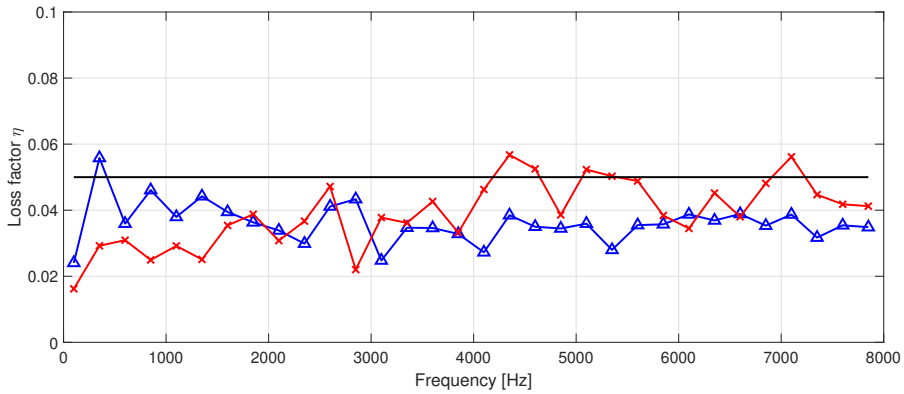

Figure II.9: Comparison of the dispersion curve of the isotropic aluminium panel with 5% structural damping. – analytic, △ classical IWC method and × enhanced IWC method.

II. 3. 2 Sandwich aluminium panel with a viscoelastic core

The method is then applied to a 1 m × 1.2 m sandwich viscoelastic panel. The skins are 2 mm thick aluminium panels (Density $\rho = 2700$ kg/m^3, Young's modulus E = 71 GPa, Poisson's coefficient ν= 0.33 and damping η_{skin}=1%). The core is a 0.76 mm viscoelastic panel (Density $\rho = 900$ kg/m^3, Young's modulus E = 1 GPa, Poisson's coefficient ν= 0.33 and damping η_{core}=20%).

The IWC wavenumber maps at 1850 Hz and 6100 Hz are shown in Fig. II.10a-b, respectively. At 1850 Hz, the isotropic behavior of the panel is observed. At 6100 Hz, a privileged direction of propagation in the positive k_x area is visible due to the effect of the excitation point. The dispersion curves determined using the classical and the enhanced IWC method are shown in Fig. II.11. Both of them are in a very good agreement compared to the GLM.

The damping loss factor estimated using the classical and the enhanced IWC method are shown in Fig. II.12. The classical IWC method overly underestimates the damping loss factor above 1000 Hz. The proposed method shows a much better agreement in the high frequency range above 4500 Hz. Between 3000 Hz to 4500 Hz, the enhanced IWC

method slightly underestimates the damping loss factor. In the low frequency range, both methods underestimate the damping loss factor. This error is due to the reflection at boundaries.

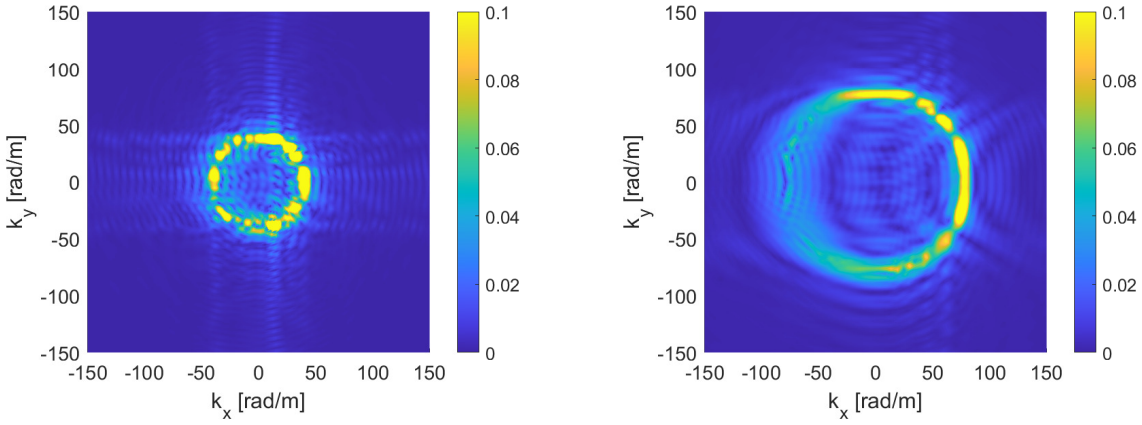

(a) 1850 Hz. (b) 6100 Hz.

Figure II.10: IWC wavenumber maps of the numerical sandwich aluminium panel with a viscoelastic core at 1850 Hz and 6100 Hz.

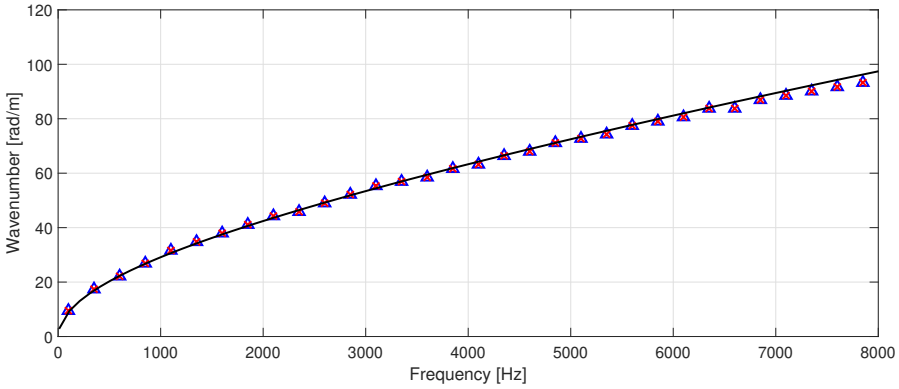

Figure II.11: Comparison of the dispersion curve of the numerical sandwich aluminium with a viscoelastic core panel. – GLM, △ classical IWC method and × enhanced IWC method.

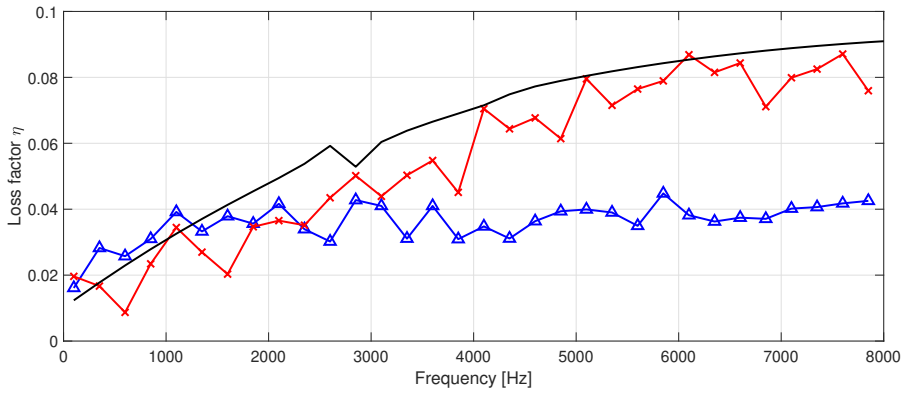

Figure II.12: Comparison of the dispersion curve of the numerical sandwich aluminium with a viscoelastic core panel. – analytic, △ classical IWC method and × enhanced IWC method.

II. 3. 3 Anisotropic 7 layers epoxy resin panel

The method is then applied to a more complex 1 m × 1.2 m 7 layers epoxy resin panel with different laminate angles. The mechanical properties of the epoxy resin is defined in Table II.1. The thickness and the orientation angles of each layer is shown in Table II.2.

ρ (kg/m^3)	E_1 (GPa)	E_2 (GPa)	E_3 (GPa)	G_{12} (GPa)	G_{13} (GPa)	G_{23}	ν_{12}	ν_{13}	ν_{23}	η
1500	133.36	7.7	7.7	3.1	3.1	2.6	0.29	0.29	0.4999	0.05

Table II.1: Mechanical properties of the epoxy resin.

Layer	Thickness (m)	Orientation (°)
1	0.000125	0
2	0.000125	30
3	0.000125	90
4	0.00025	-30
5	0.000125	90
6	0.000125	30
7	0.000125	0

Table II.2: Thickness and orientation of each epoxy resin layer.

The normal displacement at 3350 Hz is shown in Fig. II.13. The IWC wavenumber maps at 1100 Hz and 3350 Hz are shown in Fig. II.14a-b, respectively. For both frequencies, privileged directions of propagation due to the effect of the excitation coordinates are visible and the anisotropic behavior, where the wavenumber is no longer constant as a function of the angle θ, is observed.

The dispersion curves at 0°, 45° and 90° estimated using the enhanced IWC method are shown in Fig. II.15. The results are compared to the reference solution based on the

general laminate model [36]. Note that only the dispersion curves of the enhanced IWC method is shown because both classical and enhanced method are identical in estimating the real part of the wavenumber (see Section II. 2). The results at 0°, 45° and 90° show a very good agreement compared to the reference solution in the whole frequency range. Based on this result, the robustness of the IWC method in estimating the wavenumber is corroborated.

The damping loss factor estimated using the classical and the enhanced IWC methods are shown in Fig. II.16. Both results are compared with the GLM in which a power balance equation is used to estimate the loss factor [36]. In the low frequency range below 1500 Hz, both methods slightly underestimate the damping loss factor. The enhanced method shows a good agreement in average compared to the reference solution from 2000 Hz to 7000 Hz. Above 7000 Hz, the enhanced method shows discrepancies. The error is certainly due to the simple arithmetic averaging over angle θ while there are definitely directions in which the estimation is not fine due to privileged directions of wave propagation. A spatial angle filtering is needed and is discussed later in Chapter III.

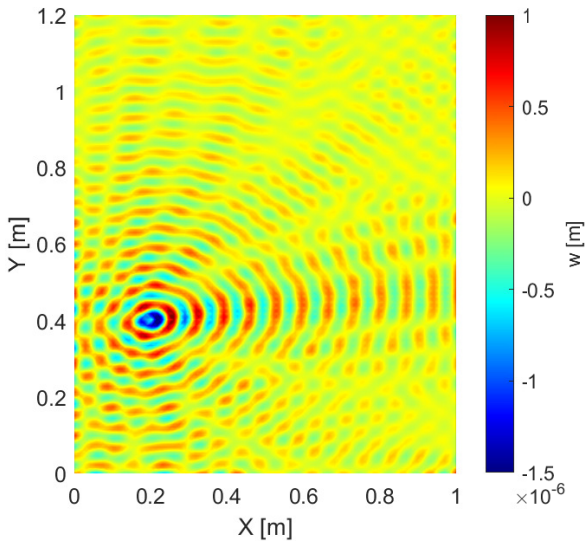

Figure II.13: Normal displacement **w** of the anisotropic 7 layers epoxy resin panel at 3350 Hz.

To conclude, the estimation of the wavenumber is the same for both classical and enhanced IWC methods. On the contrary, the enhanced IWC method improves the estimation of the damping loss factor compared to the classical method for all three tested panels. The improvement is due to the variant formulation that takes into account the exponential decay with distance from the excitation location.

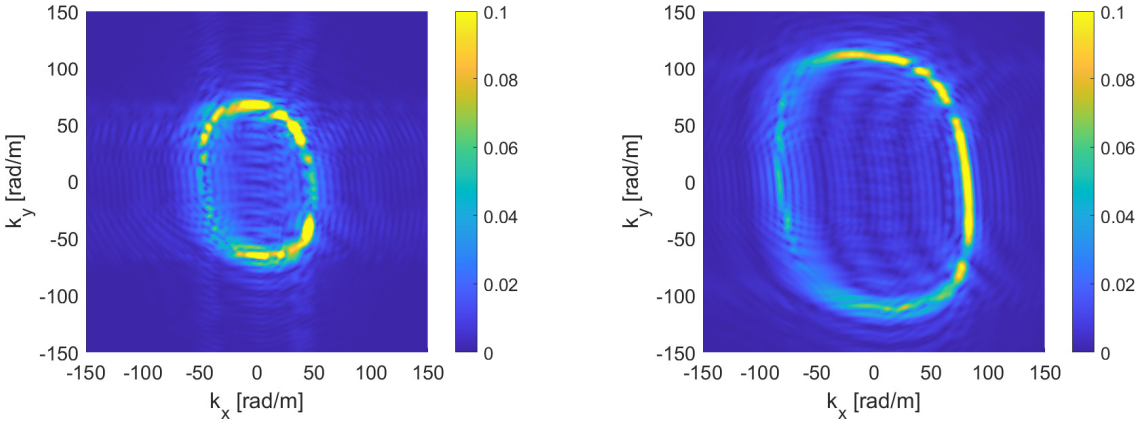

(a) 1100 Hz. (b) 3350 Hz.

Figure II.14: IWC wavenumber maps of the numerical sandwich aluminium panel with a viscoelastic core at 1850 Hz and 6100 Hz.

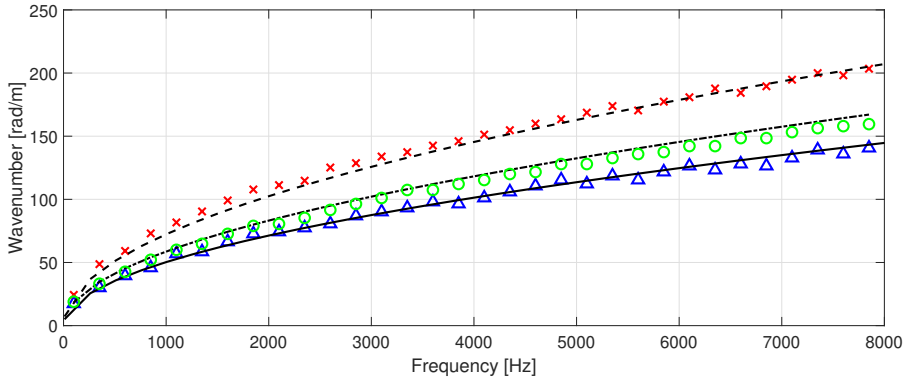

Figure II.15: Comparison of the dispersion curve of the numerical 7 layers epoxy resin panel. – GLM 0°, –. 45°, – – 90°, △ enhanced IWC method 0°, ○ enhanced IWC method 45° and × enhanced IWC method 90°.

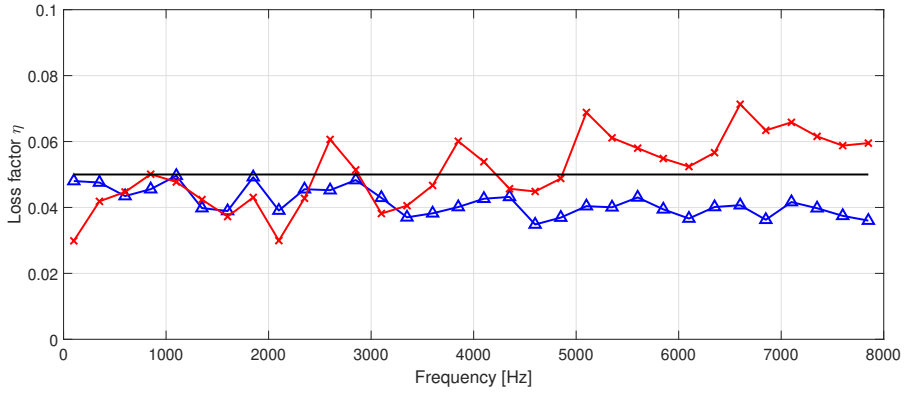

Figure II.16: Comparison of the damping loss factor of the numerical 7 layers epoxy resin panel. – exact damping, △ classical IWC method and × enhanced IWC method.

II. 4 Effect of the observation window

The objective of this section is to observe the effect of excluding the excitation location for the observation window on the results of the IWC method. As discussed in Section II. 2, both formulations Eqs. II.2 and II.3 provide similar wave propagation results if the excitation point is outside of the observation window. Thus in this section, only the enhanced method is used for the correlation function.

In theory, far from the excitation point and in the absence of strong reflections from boundaries, the circular shape of the wave propagation has grown to a large enough radius and the wave front can be approximated as a plane wave [34]. The IWC method is supposed to be able to predict the damping loss factor if the excitation point is excluded in the observation window and the vibrating field is dominated by plane wave.

To study the effect, two different sizes of the observation windows are investigated in this section. To do so, the boundary at $x = 0$ m is reduced by $\Delta x_1 = 30$ cm and $\Delta x_2 = 40$ cm for each case respectively to avoid the presence of the excitation point in the observation window. A point mechanical load excitation is fixed at $x_0 = 0.2$ m and $y_0 = 0.4$ m. The schematic presentation of the reduced observation window is shown in Fig. II.17.

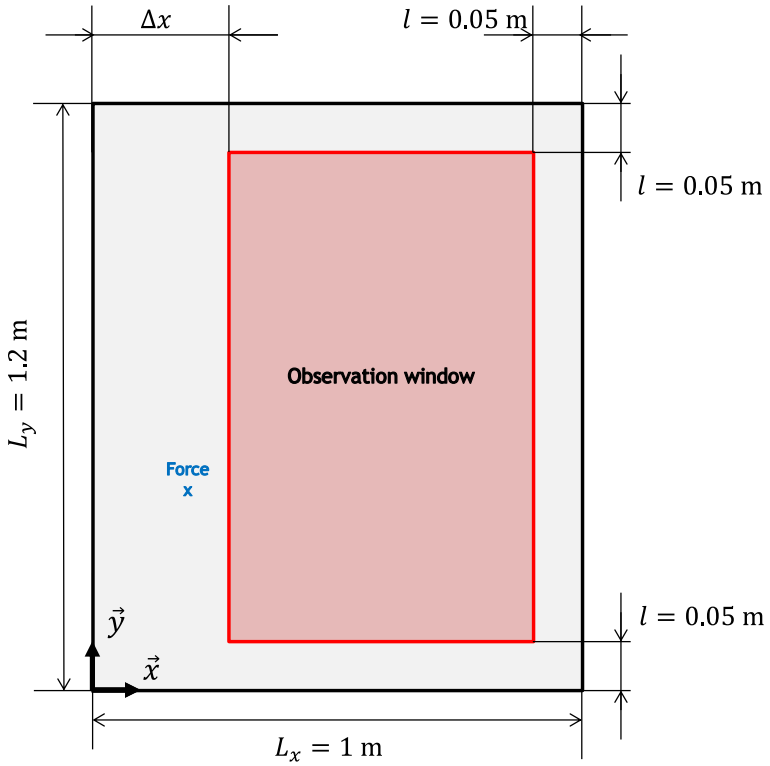

Figure II.17: Schematic presentation of the panel. The size of the observation window varies in function of Δx.

The method with reduced observation window is applied to a 1 m × 1.2 m isotropic aluminium panel (Density $\rho = 2796$ kg/m^3, Young's modulus E = 69 GPa, Poisson's coefficient ν= 0.33 and damping η=5%).

Figs. II.18 and II.19 show the IWC wavenumber maps at 1850 Hz and 6100 Hz for both

configurations, $\Delta x_1 =$ 30 cm and $\Delta x_2 =$ 40 cm, respectively. The isotropic behavior of the panel is visible for both frequencies and both configurations. The dispersion curves estimated with reduced observation windows are shown in Fig. II.20. The results are compared to the analytical solution based on the Love-Kirchhoff theory [39]. Based on the result, the method is able to identify precisely the wavenumber on the entire frequency range.

The estimation of the damping loss factor is shown in Fig. II.21. For the first case where the window is reduced by $\Delta x_1 = 30$ cm, the estimation of the damping loss factor above 3000 Hz shows a good correlation compared to the input data, $\eta = 5\%$. Below 3000 Hz, the method is not able to predict precisely the damping. For the second case where the window is reduced by $\Delta x_2 = 40$ cm, the estimation of the damping loss factor converges to the analytical solution above 5000 Hz. The reduction of the observation window deteriorates the method between 3000 Hz and 5000 Hz. The discrepancies shown by the second case between 3000 Hz and 5000 Hz as compared to the first case is due to the limited number of wavelength to predict precisely the damping loss factor. Below 3000 Hz, the discrepancies shown by both observation window sizes are more likely due to the form of the propagating wave.

To conclude, the estimation of the wavenumber is less sensitive to the size of the observation window. For both observation windows sizes, the method is able to predict precisely the wavenumber in all the frequency range. On the other hand, the estimation of the damping loss factor is more precise with a bigger observation window. In Chapter III, a method based on the Green's function is presented and allows the inclusion of the excitation point in the observation window. This new method maximizes the observation window size and improves tremendously the frequency range in which the correlation technique is applicable.

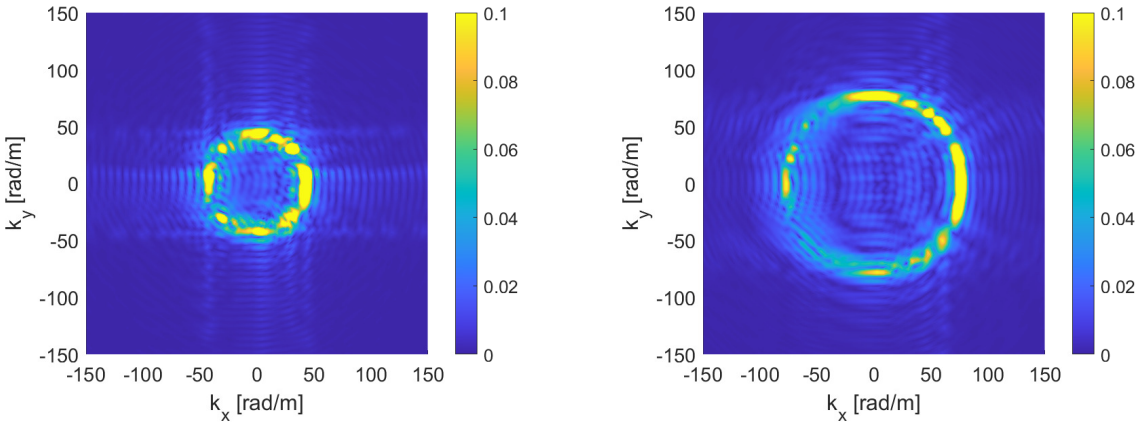

(a) 1850 Hz. (b) 6100 Hz.

Figure II.18: IWC wavenumber maps of the aluminium panel at 1850 Hz and 6100 Hz for the first case ($\Delta x_1 = 30$ cm).

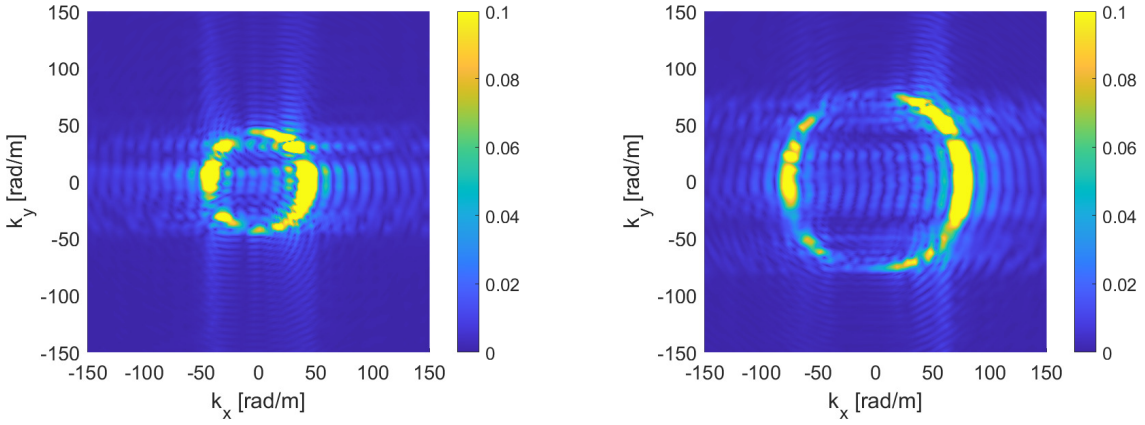

(a) 1850 Hz. (b) 6100 Hz.

Figure II.19: IWC wavenumber maps of the aluminium panel at 1850 Hz and 6100 Hz for the first case ($\Delta x_2 = 40$ cm).

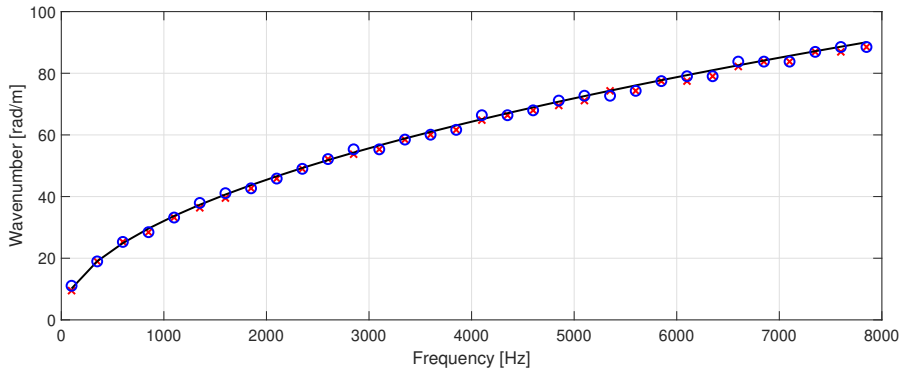

Figure II.20: Comparison of the dispersion curve of the numerical isotropic aluminium panel with 5% structural damping. – analytic, × enhanced IWC method with $\Delta x_1 = 30$ cm and ○ enhanced IWC method with $\Delta x_2 = 40$ cm.

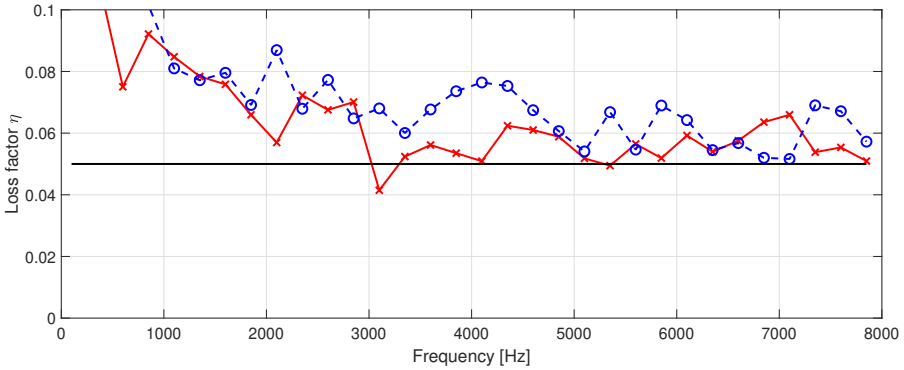

Figure II.21: Comparison of the damping loss factor of the numerical isotropic aluminium panel with 5% structural damping and with reduced observation window. × enhanced IWC with $\Delta x_1 = 30$ cm and – ○ – enhanced IWC with $\Delta x_2 = 40$ cm.

II.5 Effect of the excitation location

Contrary to the previous application of the proposed method where the excitation location is fixed at $x_0 = 0.2$ m and $y_0 = 0.4$ m, this section investigates the effect of different excitation location on the estimation of the wavenumber and the damping loss factor by fixing the size of the observation window.

Based on the observation of the IWC wavenumber maps in the two previous sections, privileged directions of the wave propagation are dependant on the excitation position. For isotropic structures where the wavenumber is similar regardless the directions of the angle θ, the estimation of the wavenumber is easily determined by localising the global maximum of the map for each frequency. However for non-isotropic structures, the estimation of the wavenumber may be difficult for some of the directions θ if the excitation location is badly chosen.

The first objective of this section is to illustrate this effect by applying the proposed method to two panels: 1) an isotropic aluminium panel and 2) an anisotropic 7 layers epoxy panel. Secondly, the objective of this investigation is to illustrate the impact of different excitation location on the estimation of the damping loss factor.

The simulations are done over three different excitation points. The first one is $x_{0_1} = 0.2$ m and $y_{0_1} = 0.4$ m. The second one is the central excitation at $x_{0_2} = 0.5$ m and $y_{0_2} = 0.6$ m. The third one is an excitation near the edge at $x_{0_3} = 0.1$ m and $y_{0_3} = 0.1$ m.

For each case, the observation window is reduced by 5 cm from each boundary. The schematic presentation of the three excitation points is shown in Fig. II.22.

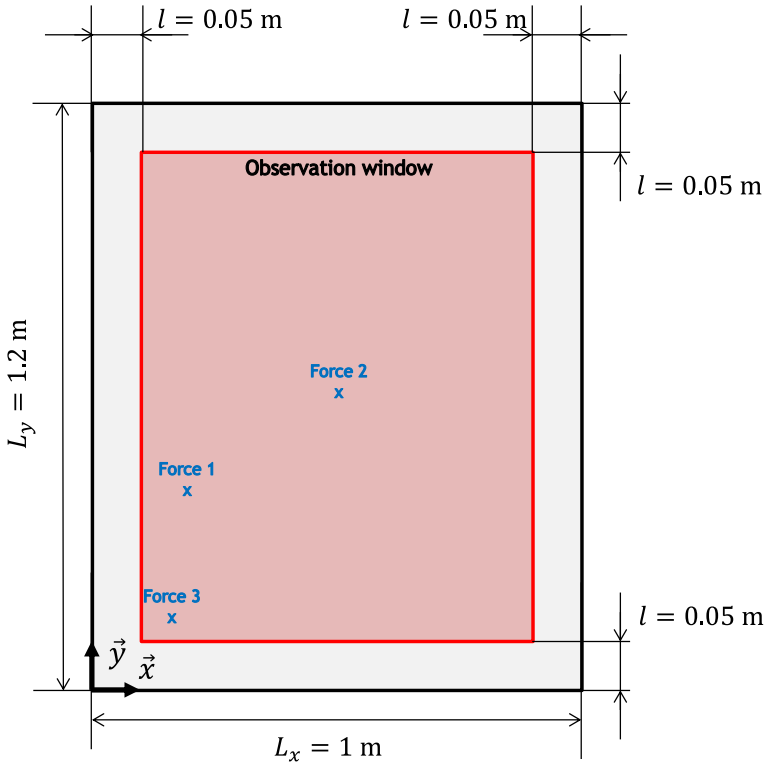

Figure II.22: Schematic presentation of the panel with three different excitation points.

II. 5. 1 Isotropic aluminium panel

The studied case is applied to a 1 m × 1.2 m isotropic aluminium panel (Density $\rho = 2796$ kg/m^3, Young's modulus E = 69 GPa, Poisson's coefficient $\nu = 0.33$ and damping $\eta = 5\%$).

The IWC wavenumber maps at 1850 Hz and 6100 Hz of the three different simulations are shown in Fig. II.23. For the maps at 1850 Hz, the isotropic behavior of the panel is clearly identifiable for the all cases as shown in Fig. II.23a, Fig. II.23c and Fig. II.23e. However, a privileged direction of propagation is more pronounced for the third case compared to the first and second cases.

For the maps at higher frequency of 6100 Hz, the isotropic behaviour is clearly visible for the second excitation as shown in Fig. II.23d. The radius of the maximum is almost constant as a function of the angle. For the first excitation as shown in Fig. II.23b, a privileged direction of the propagation in the negative k_x area of the map is visible. However, the isotropic behavior of the panel is still identifiable. For the third excitation as shown in Fig.II.23f, the wave propagation is very directive in the third quadrant of the map. The isotropic behavior for this case is not easily identifiable.

The dispersion curves at 180° of each excitation are estimated in Fig. II.24. For the first and second excitation, a good correlation of the dispersion curve compared to the analytical solution is observed in the whole frequency range. For the third excitation, some discrepancies are visible at 5000 Hz, 6800 Hz and 7600 Hz. These discrepancies are certainly due to the privileged directions of the wave propagation of the panel.

However, the estimation of the damping loss factor is much more difficult to be exploited. Fig. II.25 shows the damping loss factor of three different excitation points using the classical IWC method. For the central excitation, the method overestimates the damping loss factor on the entire frequency range. For the first excitation, the method underestimates the damping loss factor in the frequency range above 500 Hz. For the third case, the method overestimates the damping loss factor below 3500 Hz and underestimates the damping above 500 Hz.

Fig. II.26 shows the estimation of the damping loss factor using the enhanced formulation of the IWC method. For the central excitation, the method shows discrepancies on the entire frequency range. The discrepancies are due to the response observed in the window is dominated by the near field which does not resemble to an inhomogeneous plane wave. For the first and second excitation, the enhanced IWC method shows good agreement above 4000 Hz compared to the input data. However below 4000 Hz, the damping loss factor is underestimated. The error is certainly due to the simple arithmetic averaging over angle θ while there are definitely directions in which the estimation is not fine due to privileged directions of wave propagation. A spatial angle filtering is needed and is discussed later in Chapter III.

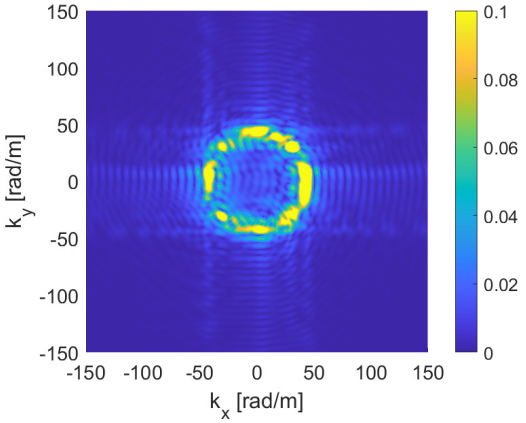

(a) 1850 Hz, $x_{0_1} = 0.2$ m and $y_{0_1} = 0.4$ m.

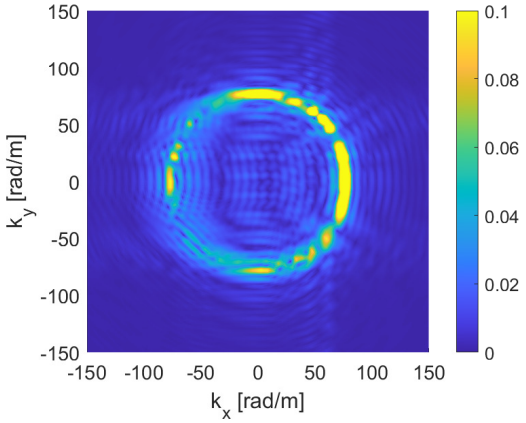

(b) 6100 Hz, $x_{0_1} = 0.2$ m and $y_{0_1} = 0.4$ m.

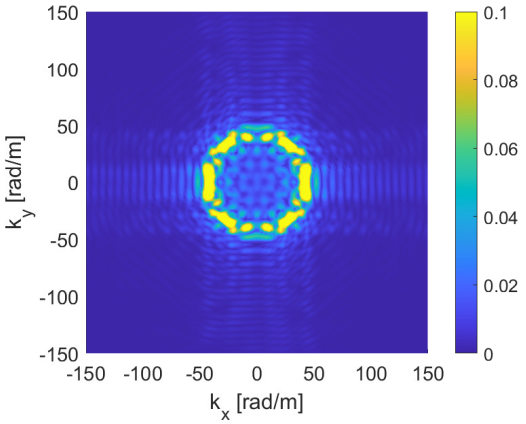

(c) 1850 Hz, $x_{0_2} = 0.5$ m and $y_{0_2} = 0.6$ m.

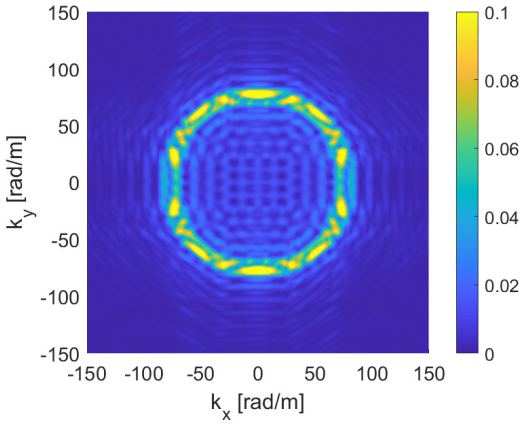

(d) 6100 Hz, $x_{0_2} = 0.5$ m and $y_{0_2} = 0.6$ m.

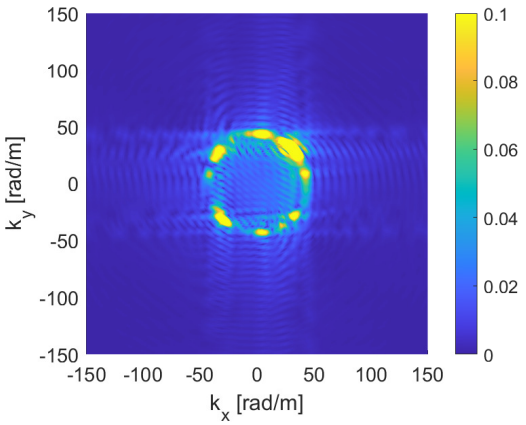

(e) 1850 Hz, $x_{0_3} = 0.1$ m and $y_{0_3} = 0.1$ m.

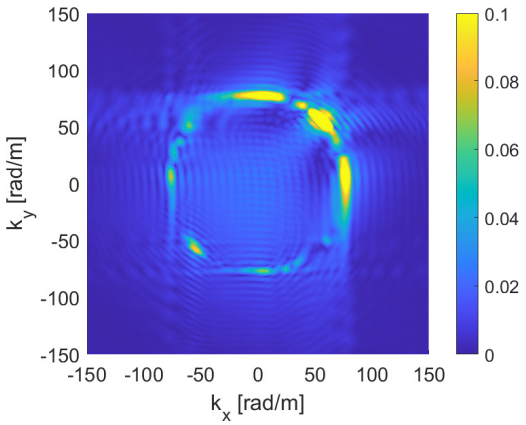

(f) 6100 Hz, $x_{0_3} = 0.1$ m and $y_{0_3} = 0.1$ m.

Figure II.23: IWC wavenumber maps of the numerical isotropic aluminium with 5% structural damping subjected to different points of excitation.

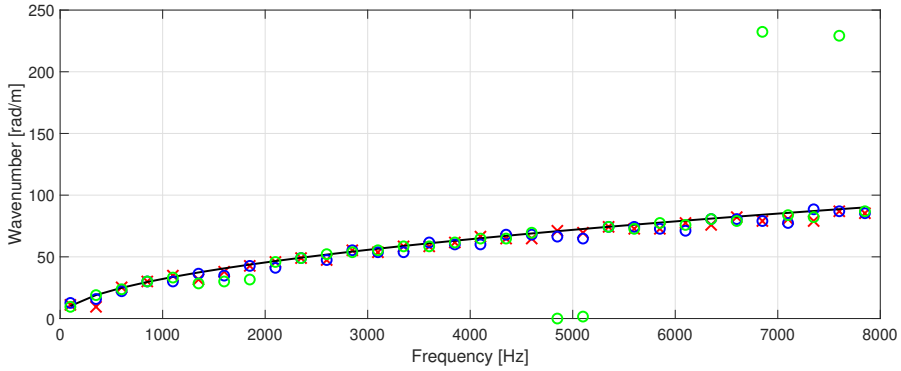

Figure II.24: Comparison of the dispersion curve of the numerical isotropic aluminium panel with 5% structural damping and with different excitation points **at** 180°. − GLM, × $x_{0_1} = 0.2$ m and $y_{0_1} = 0.4$ m, ○ $x_{0_2} = 0.5$ m and $y_{0_2} = 0.6$ m, ○ $x_{0_3} = 0.1$ m and $y_{0_3} = 0.1$ m.

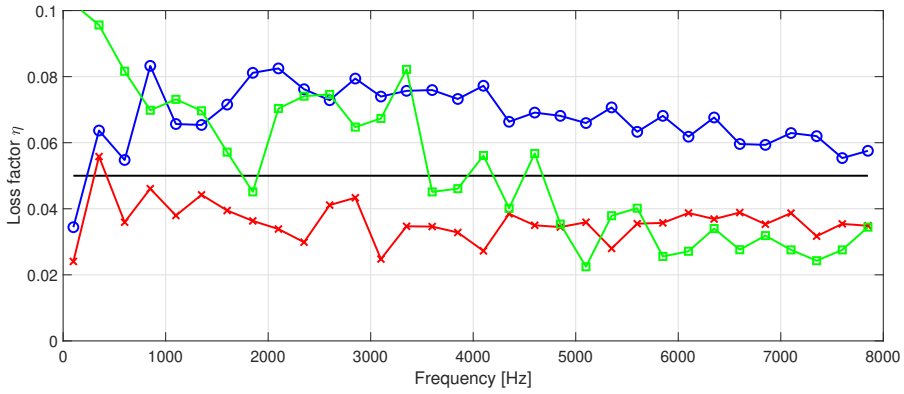

Figure II.25: Comparison of the damping loss factor of the numerical isotropic aluminium panel with 5% structural damping and with different excitation points using the classical IWC method. − GLM, × $x_{0_1} = 0.2$ m and $y_{0_1} = 0.4$ m, ○ $x_{0_2} = 0.5$ m and $y_{0_2} = 0.6$ m, □ $x_{0_3} = 0.1$ m and $y_{0_3} = 0.1$ m.

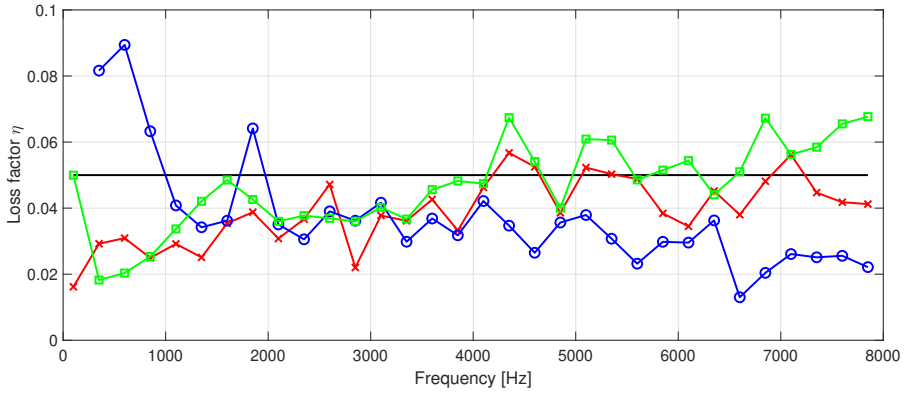

Figure II.26: Comparison of the damping loss factor of the numerical isotropic aluminium panel with 5% structural damping and with different excitation points using the enhanced IWC method. − GLM, × $x_{0_1} = 0.2$ m and $y_{0_1} = 0.4$ m, ○ $x_{0_2} = 0.5$ m and $y_{0_2} = 0.6$ m, □ $x_{0_3} = 0.1$ m and $y_{0_3} = 0.1$ m.

II. 5. 2 Anisotropic 7 layers epoxy panel

The same investigation is then applied to an anisotropic 1 m × 1.2 m 7 layers epoxy resin panel with different angles of orientation. The orientation angles and the thickness of each layer are shown in Tab. II.2. The mechanical properties of the epoxy resin are defined in Fig. II.1.

The IWC wavenumber maps at 1850 Hz and 6100 Hz of three different simulations are shown in Fig. II.27. For the first case at 1850 Hz, some privileged directions in the second and third quadrants can be seen as shown in Fig. II.27a. However, the anisotropic behavior of the panel is still visible. For the first excitation at 6100 Hz as shown in Fig. II.27b, the anisotropic behavior is less visible compared to the map at 1850 Hz but it can still be identified.

For the second excitation where the panel is subject to a central excitation, the amplitude of the maximum is almost constant as a function of the angle and the anisotropic behavior can easily be identified for both frequencies (see Figs. II.27c-d). However for the third excitation, the wave propagation are very directive for both frequencies at 1850 Hz and 6100 Hz as shown in Figs. II.27e-f respectively and the anisotropic behavior is no longer easily predictable. The amplitude of the maximum is concentrated in the third quadrant of the map for both frequencies.

The dispersion curves at 40° and 220° for each excitation are presented in Figs. II.28 and II.29, respectively. A very good correlation is visible for all cases at 40°. At 220°, a very good correlation is visible between the IWC method for the first and second excitation as compared to the reference solution based on the general laminate model (GLM) [36]. However for the third excitation, some discrepancies are visible at 800 Hz 2800 Hz, 4600 Hz and 7600 Hz. These discrepancies are certainly due to the privileged directions of the wave propagation of the panel as shown in the IWC wavenumber maps.

The damping loss factor estimation using the enhanced IWC method of three different excitation points is shown in Fig. II.30. For the second case where the panel is subject to a central excitation, the proposed method underestimates the damping loss factor in the whole frequency range. For the first and third cases, the enhanced IWC method shows good agreement compared to the GLM above 1000 Hz. Below this frequency, the proposed method slightly underestimates the damping loss factor. Again, the error is certainly due to the simple arithmetic averaging over angle θ while there are definitely directions in which the estimation is not fine due to privileged directions of wave propagation. A spatial angle filtering is needed and is discussed later in Chapter III.

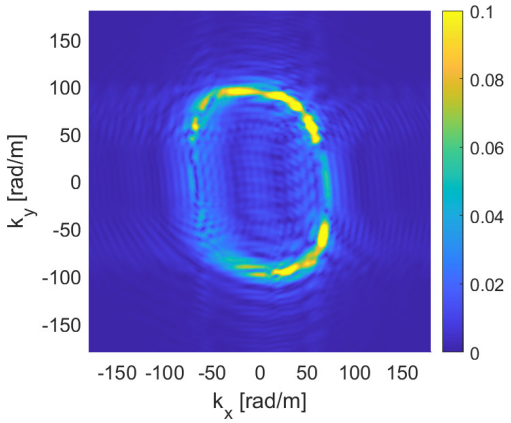

(a) 1850 Hz, $x_{0_1} = 0.2$ m and $y_{0_1} = 0.4$ m.

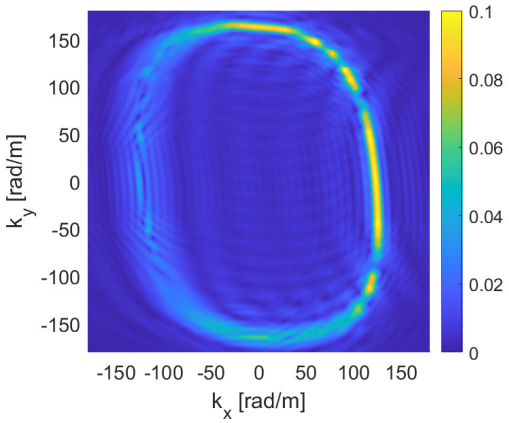

(b) 6100 Hz, $x_{0_1} = 0.2$ m and $y_{0_1} = 0.4$ m.

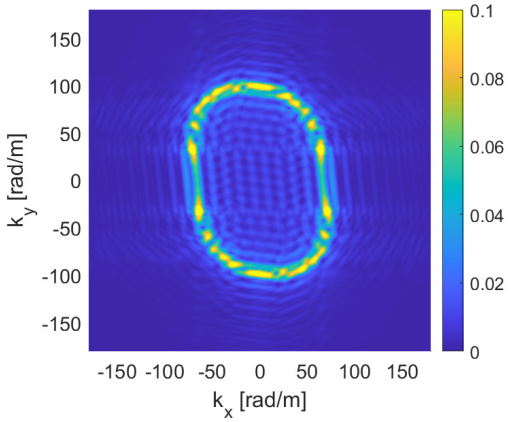

(c) 1850 Hz, $x_{0_2} = 0.5$ m and $y_{0_2} = 0.6$ m.

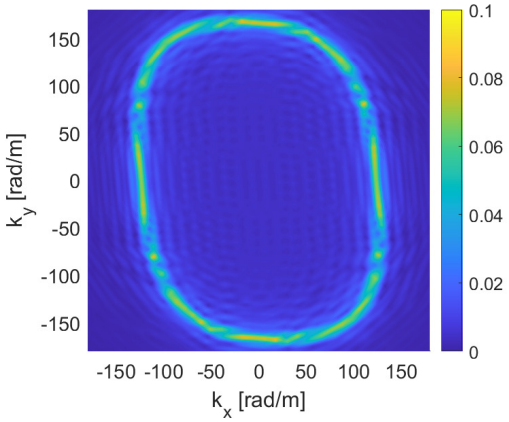

(d) 6100 Hz, $x_{0_2} = 0.5$ m and $y_{0_2} = 0.6$ m.

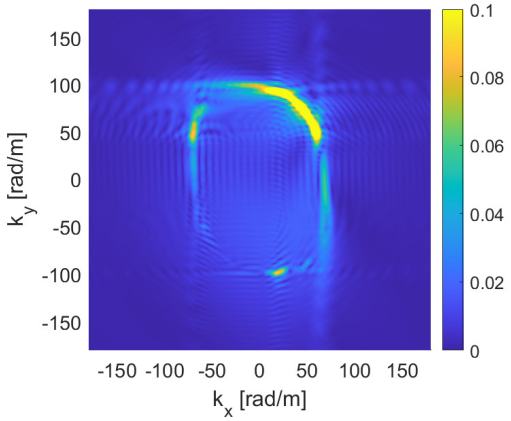

(e) 1850 Hz, $x_{0_3} = 0.1$ m and $y_{0_3} = 0.1$ m.

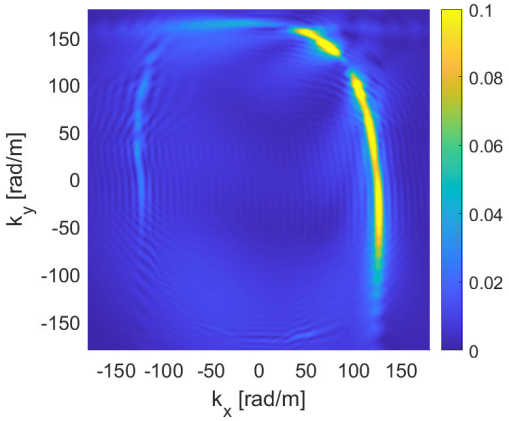

(f) 6100 Hz, $x_{0_3} = 0.1$ m and $y_{0_3} = 0.1$ m.

Figure II.27: IWC wavenumber maps of the numerical anisotropic 7 layers epoxy resin panel with 5% structural damping subject to different points of excitation.

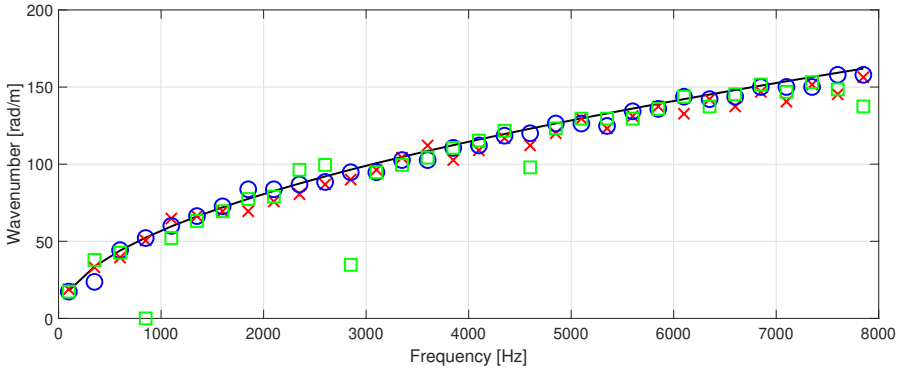

Figure II.28: Comparison of the dispersion curve of the numerical anisotropic 7 layers epoxy resin panel with 5% structural damping and with different excitation points **at** 220°. − analytic, × $x_{0_1} = 0.2$ m and $y_{0_1} = 0.4$ m, ○ $x_{0_2} = 0.5$ m and $y_{0_2} = 0.6$ m, □ $x_{0_3} = 0.1$ m and $y_{0_3} = 0.1$ m.

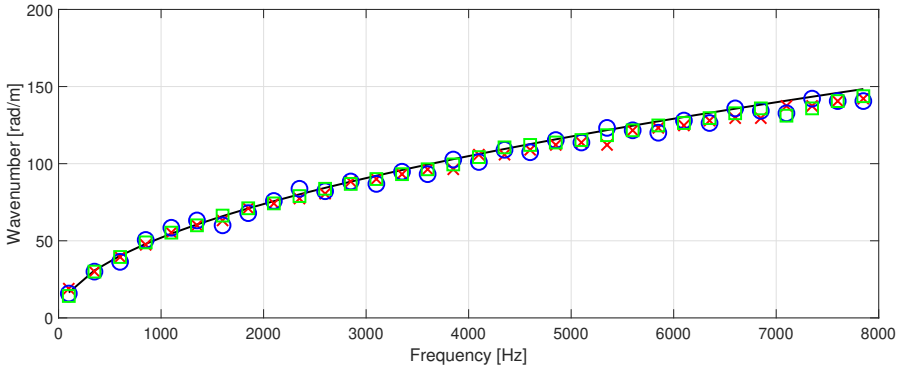

Figure II.29: Comparison of the dispersion curve of the numerical anisotropic 7 layers epoxy resin panel with 5% structural damping and with different excitation points **at** 40°. − analytic, × $x_{0_1} = 0.2$ m and $y_{0_1} = 0.4$ m, ○ $x_{0_2} = 0.5$ m and $y_{0_2} = 0.6$ m, □ $x_{0_3} = 0.1$ m and $y_{0_3} = 0.1$ m.

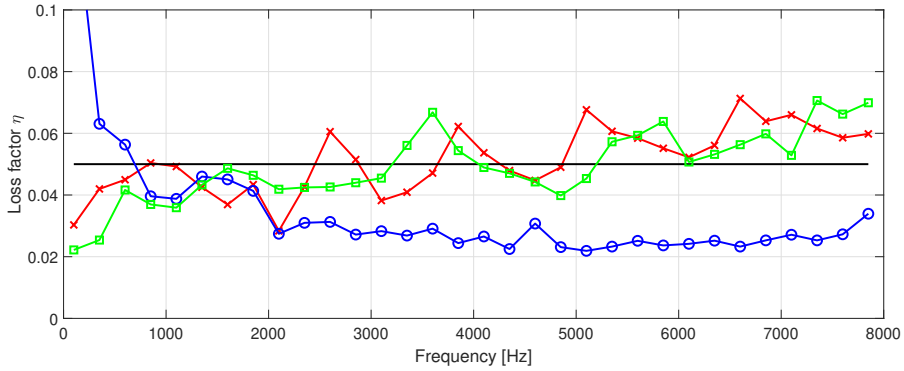

Figure II.30: Comparison of the damping loss factor of the anisotropic 7 layers epoxy resin panel 5% structural damping and with different excitation points using the enhanced IWC method. − analytic, × $x_{0_1} = 0.2$ m and $y_{0_1} = 0.4$ m, ○ $x_{0_2} = 0.5$ m and $y_{0_2} = 0.6$ m, □ $x_{0_3} = 0.1$ m and $y_{0_3} = 0.1$ m.

II.6 Limitations related to the plane wave assumption

Three different studies have been conducted to investigate the robustness of the method in the previous sections. Globally, the enhanced method improves the estimation of the damping loss factor compared to the classical IWC method. However, the application of the proposed method in the presence of the excitation point shows discrepancies. In fact, the plane wave assumption is limited due to the nature of the plane wave itself.

To observe this limitation, an example of a simply supported aluminium panel excited with a point force is used for the demonstration (Length along x direction $L_x = 2$ m, Length along y direction $L_y = 1$ m, Density $\rho = 2796$ kg/m^3, Young's modulus E = 69 GPa, Poisson's coefficient ν= 0.33 and damping η=10%). The panel is subject to a central excitation at $x_0 = 1$ m and $y_0 = 0.5$ m.

The solution of the equation of motion is solved analytically by using the modal decomposition method. The equation writes (time-harmonic convention of $e^{-\mathrm{i}\omega t}$) [39]:

$$w(x,y,\omega) = \sum_{m=1}^{m}\sum_{n=1}^{n} \frac{\varphi_{mn}(x_0,y_0)\varphi_{mn}(x,y)}{\omega_{mn}^2 - \omega^2 + \mathrm{i}\eta\omega\omega_{mn}} \frac{4}{\rho h L_x L_y} \quad , \tag{II.4}$$

where the mode shapes are written as:

$$\varphi_{mn}(x,y) = \sin(\frac{m\pi x}{L_x})\sin(\frac{n\pi y}{L_y}) \quad , \tag{II.5}$$

and the eigen frequencies are defined by:

$$\omega_{mn} = \sqrt{\frac{D}{\rho h}}\left(\left(\frac{m\pi}{L_x}\right)^2 + \left(\frac{n\pi}{L_y}\right)^2\right) \quad . \tag{II.6}$$

Fig. II.31 shows the real part of the normal displacement of the panel along the vertical line $y = 0.5$ m. The displacement field $w(x, y = 0.5\ m, \omega)$ is compared to the Green's function of an isotropic infinite plate in Eq. I.30 and the enhanced inhomogeneous wave in Eq. II.3.

In order to quantify the error, the normalized reconstruction error is calculated. The equation writes [75]:

$$e = \frac{||w(x,y,\omega) - \tilde{w}||^2}{||w(x,y,\omega)||^2} \quad , \tag{II.7}$$

where $w(x,y,\omega)$ is the harmonic field and $\tilde{w}$ is either the Green's function (see Eq. I.30) or the inhomogeneous wave and $||...||$ denotes the Euclidean norm of a matrix.

The error calculated for the case shown in Fig. II.31 is about 23.4% for the Green's function and is about 116.3% for the inhomogeneous wave.

To conclude, the error calculated between the measured displacement field and the enhanced inhomogeneous wave is much superior compared to the error calculated between

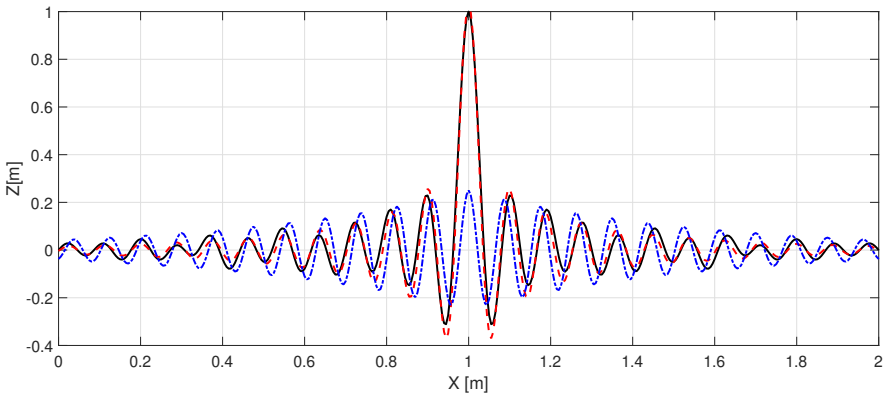

Figure II.31: Real part of the normal displacement of a simply supported panel along $y = 0.5$ m, the Green's function and the inhomogeneous wave (frequency, $f = 5000$ Hz). - Harmonic field, - - Green's function and -. inhomogeneous wave.

the measured displacement field and the Green's function. The plane wave assumption is very limited in the presence of the excitation point in the observation window. The correlation function can be improved by replacing the inhomogeneous wave with the Green's function to represent better the vibrational field and will be studied in Chapter III

II.7 Conclusion of the chapter

An enhanced formulation of the IWC method to improve the estimation of the damping loss factor has been introduced in this chapter. The performance of the method has been demonstrated numerically by comparison with a reference analytical model.

For the wavenumber, the classical and the new enhanced IWC method are able to predict precisely the wavenumber for all the cases if the excitation point is correctly defined. However, the accuracy of the estimation of the damping loss factor varies as a function of different parameters. For the first case where the excitation point is fixed and is in the observation window, the proposed method improves the estimation of the damping loss factor compared to the classical method for all the panels.

For the second case where the excitation point is outside of the observation window, the proposed method shows good agreement compared to the reference analytical model in the high frequency range. However in the low frequency range, the method is limited due to the window size. Here, the proposed method that takes into account the effect of the excitation point presents a major advantage because the observation can be maximized and thus, the estimation of the damping loss factor in the low frequency range can be improved.

For the third case with three different excitation points, the damping loss factor estimation where the panel is subjected to a central excitation shows discrepancies in the whole frequency range for both classical and enhanced methods. On the contrary, the enhanced method improves the estimation of the damping loss factor when the panel is subject to the excitation near the edge. Certainly, an enhanced angle averaging, excluding directions wherein the estimation is inaccurate will improve the results. This will be illustrated in Chapter III.

In conclusion, the estimation of the damping loss factor of a finite panel using the plane wave assumption remains difficult in the presence of the excitation point. In the next chapter, the inhomogeneous wave is replaced with a Green's function based-model. It will be shown that this approach improves tremendously the estimation of the damping loss factor because it is more adapted to describe the vibrational field near the excitation point.

Chapter III

Green's function based-model correlation method

In this chapter, a Green's function-based model correlation (GFC) method able to estimate the damping loss factor as a function of the frequency and the heading angle of complex structures is introduced. The first part of this chapter is presented as an article submitted to the *Journal of Sound and Vibration* in June 2022. A preliminary version of the method developed herein has also been communicated and published in a conference as:

M. N. Bin Fazail, J.-D. Chazot, G. Lefebvre, N. Atalla, Identification of the dispersion curves and the damping loss factor using green's function-based model of non-isotropic structures, Proceedings of the 28th International Congress on Sound and Vibration, Singapore (2022)

In the second part of the chapter, a further work on the effect of the excitation location to the estimation of the damping loss factor is presented. Three different excitation locations are defined: the first is near a boundary, the second is at the center and the third is near a corner. The performance of each excitation location is studied numerically and experimentally.

Damping loss factor characterization of complex structures using a Green's function-based model

Muhammad Najib BIN FAZAIL, Jean-Daniel CHAZOT, Gautier LEFEBVRE, Noureddine ATALLA

Journal of Sound and Vibration (under review), 2022

Abstract

The Inhomogeneous Wave Correlation technique has been used to estimate experimentally the wavenumber of simple and complex structures. However this method is essentially focused on the real part of the wavenumber and is not always robust to measure the damping loss factor related to its imaginary part. Another correlation technique able to capture the damping effects of complex structures as function of the heading angle accurately is presented here. Instead of using an inhomogeneous plane wave, the correlation is made with a Green's function to better take into account the behavior of the structure excited by a point force. Several results, with simulated and measured data, are compared with an analytical discrete laminate model and show the accuracy of this Green's Function Correlation technique to recover the damping loss factor of complex structures with high damping and in the mid to high frequency range.

III. 1 Introduction

In the domain of transportation industry, noise control requires robust simulation tools to predict the vibratory and acoustic levels inside and outside vehicles such as airplanes, cars and trains. Numerous global [21, 86, 41, 42, 43, 7] and local [71, 72, 1, 57] characterization methods have been developed throughout the years to feed the numerical models with accurate input data.

One of the local approaches that has been widely used is the Force Analysis Technique (FAT) [71, 72, 1, 57]. This method estimates the equation of motion by means of a finite different scheme. The Corrected Force Analysis Technique (CFAT) [49, 48] extends the method to reduce the bias error of the finite different scheme by adding correction factors. The main advantage of this method is the ability to be applied without any knowledge outside of the studied area such as the boundary conditions or sources. However, this method is sensitive to measurement uncertainties.

The global method based on the wave fitting approach which is less sensitive to measurement uncertainties is adapted in this paper. One of the first wave approach application has been carried out by McDaniel et al. [62, 61] to estimate the complex wavenumber and the damping loss factor of one dimensional structures. This approach is based on the error minimisation between a wave model and the measured responses. The discrete spatial Fourier Transform (DFT) [50, 42, 33] has also been used widely to determine the wavenumber of two dimensional structures. The rapidity and the bijectivity of the method presents major advantages but is limited to equally measurement points and is not able to estimate the damping loss factor.

The Inhomogeneous Wave Correlation (IWC) developed by Berthaut et al. [7] extends the previous method and allows the identification of the wavenumber. This approach is based on the maximization of the correlation between an inhomogeneous wave and the spatial field as a function of the wave heading angle or the direction of the wave propagation. The method has been applied to one-dimensional structures [73], two-dimensional sandwich structures with honeycomb cores [41, 21], stiffened panels [42, 43], panel with distributed resonators [87] and curved structures [86]. Cherif et al. [21] applied the IWC method to estimate the average damping loss factor of orthotropic structures using an iterative refinement process. One of the major drawbacks of this approach is the complexity to define the iteration range to achieve the convergence of results.

In fact, the IWC method which is based on the plane wave hypothesis is limited due to the nature of the plane wave itself. Indeed, the vibrational field near the excitation point cannot be compared with a plane wave. Therefore the measurements must be done over an observation area sufficiently far from the excitation point. In reality, this condition is difficult to obtain due to the finite dimensions of the panel. To overcome this last limitation, Tufano in his dissertation [83] replaced the inhomogeneous wave by the Green's function of the isotropic infinite plate. This method combines advantages of the IWC and the Green's function which uses a set of Hankel's function. Tufano applied his method to an isotropic laminated plate and to an isotropic plate with tuned mass damper (TMD).

Another wave fitting approach has been introduced by Cuenca et al. [27, 28]. In this approach, the harmonic displacement field model is constructed by combining the contri-

bution of the image sources emitting the Green's function of an infinite plate. This model is then fitted with the measured displacement field to estimate the material properties. Roozen et al. [75] applied the method experimentally to estimate the wavenumber and the damping loss factor of a thin isotropic plate by adding a Bayesian regularisation to increase the accuracy of the method. Recently, Marchetti et al. [57] extended the method to characterize elliptical orthotropic structures based on the analytical expression developed by Berthaut [6] in the appendix of his thesis.

To the best of our knowledge, the application of the Green's function to estimate the wavenumber and in particular, the damping loss factor to more complex structures has never been developed or at least published. This Green's function-based model correlation (GFC) method enables to estimate the wavenumber and in particular, the damping loss factor in function of the heading angle without using an iterative refinement process. This method offers more stability in estimating the damping loss factor for highly damped structures in the mid to high frequency range.

The proposed method is applied to multilayered structures with different degrees of complexities and compared to analytical solutions based on a discrete laminate model [36]. On the other hand, experimental validations are also presented in this paper. The estimation of the average damping loss factor is compared to reference methods such as the half-power bandwidth method [67], the decay rate method [9, 11] and the power input method [11].

In Section III. 2, the overview of the IWC method is described and the Green's function based-model replacing the plane wave assumption is introduced. The numerical validation on panels with different complexities such as a sandwich laminated glass with frequency dependant characteristic viscoelastic core, an anisotropic sandwich laminate panel with different fibers orientation and an orthotropic sandwich graphite-epoxy with a viscoelastic core panel is described in details in Section III. 3 to validate the feasibility of the method. The experimental procedures to measure the harmonic field of the sandwich carbon fiber honeycomb panel with thick core are described and associated results are discussed in Section III. 4.

III. 2 Theory

III. 2. 1 Inverse Wave method

The method developed in this paper is based on the Inhomogeneous Wave Correlation (IWC) function. This approach calculates the correlation between the measured displacement field $\hat{w}(x, y)$ and an inhomogeneous plane wave defined as:

$$\hat{\sigma}_{k,\gamma,\theta}\left(x_i, y_i\right) = \mathrm{e}^{-\mathrm{i}k(\theta)(1+\mathrm{i}\gamma(\theta))(x_i \cos\theta + y_i \sin\theta)} \quad , \tag{III.1}$$

where k is the wavenumber, γ is the attenuation factor, θ is the propagation angle and (x_i, y_i) are the coordinates of the point i. The correlation function is given by:

$$\mathrm{IWC}(k,\gamma,\theta) = \frac{|\sum_{i=1}^{N} \hat{w}(x_i,y_i)\sigma^*_{k,\gamma,\theta}(x_i,y_i)\rho_i S_i|}{\sqrt{\sum_{i=1}^{N}|\hat{w}(x_i,y_i)|^2\rho_i S_i \sum_{i=1}^{N}|\sigma_{k,\gamma,\theta}(x_i,y_i)|^2\rho_i S_i}} \quad , \tag{III.2}$$

where * denotes the complex conjugate, ρ_i is a surface integration weight at point i (ρ_i=1 if the surface is divided into equal surface patches and the integrand is assumed constant over each patch), S_i is an estimation of the surface around the point i and N is the total number of acquisition points [7]. The algorithm first defines the angle θ into a discrete set of values (θ_j). For each of these angles, the value of (k_i, γ_i) that maximizes the IWC function is determined [7].

III. 2. 2 IWC method with a Green's function-based model

Using the same idea described in the Section III. 2. 1, a modified IWC method is defined in this section. This formulation replaces the inhomogeneous wave with a Green's function-based model. For a thin plate of infinite dimensions subject to a harmonic point excitation, the Green's function is described as [38, 27]:

$$G_\infty(\hat{k},r) = \frac{\mathrm{i}}{8\hat{k}^2 D}[H_0^{(1)}(\hat{k}r) - H_0^{(1)}(\mathrm{i}\hat{k}r)] \quad , \tag{III.3}$$

where G_∞ is the Green's function of the infinite plate, $\hat{k}$ is the complex wavenumber defined by $\hat{k} = k_R + \mathrm{i}k_I$, D is the flexural stiffness defined by $D = \frac{Eh^3}{12(1-\nu^2)}$, E is the Young's modulus, h is the thickness, ν is the Poisson's coefficient and $H_0^{(1)}$ is the zero order Hankel's function of the first kind. The radius, r, is defined as the distance between the excitation point and the observation point.

The flexural stiffness in Eq. III.3 can be eliminated by introducing the dispersion relation of the flexural wavenumber:

$$k^2 = \sqrt{\frac{m_s}{D}}\omega \quad , \tag{III.4}$$

where m_s is the mass per unit area and ω is the angular frequency. Adding an angle dependency of the governing equation, the proposed Green's function-based model is [10]:

$$G(\hat{k},r,\theta) = \frac{\mathrm{i}\hat{k}^2(\theta)}{8m_s\omega^2}[H_0^{(1)}(\hat{k}(\theta)r) - H_0^{(1)}(\mathrm{i}\hat{k}(\theta)r)] \quad . \tag{III.5}$$

This function does not verify the anisotropic infinite plate equation but enables to estimate the equivalent elastic parameters of complex structures at different propagation angles.

In polar coordinates, the correlation function writes:

$$\mathrm{GFC}(\hat{k},r,\theta) = \frac{|\sum_{i=1}^{N} \hat{w}(r,\theta)G^*(\hat{k},r,\theta)\rho_i S_i|}{\sqrt{\sum_{i=1}^{N}|\hat{w}(r,\theta)|^2\rho_i S_i \sum_{i=1}^{N}|G(k,r,\theta)|^2\rho_i S_i}} \quad . \tag{III.6}$$

The identification of the complex wavenumber is obtained by maximizing GFC($\hat{k}, r, \theta$) at each angle and each frequency. The complex wavenumber can also be defined as $\hat{k}(\theta) = k(\omega, \theta)(1 + \mathrm{i}\gamma(\omega, \theta))$ where γ is the attenuation factor.

The estimation is done in two steps. First, the algorithm estimates the real part of the wavenumber $k(\gamma, \theta)$ and then, the attenuation factor $\gamma(\omega, \theta)$ is quantified. The dispersion maps shown in this paper are obtained by calculating just the real part in the GFC criterion.

III. 2. 3 Damping loss factor

Based on the method described in the previous section, the damping loss factor is determined using the following equation [53, 47, 56]:

$$\eta(\omega, \theta) = -2\frac{\mathrm{Im}(\hat{k}(\theta))}{\mathrm{Re}(\hat{k}(\theta))}\frac{c_g}{c_\varphi} \quad , \tag{III.7}$$

where $c_g = \partial\omega/\partial k$ is the group velocity and $c_\varphi = \omega/k$ is the phase velocity. Both group and phase velocities can be estimated from the dispersion curve. Note that to better calculate both group and phase velocities, a smoothing of the wavenumber is necessary. Using the attenuation factor introduced in Eq. I.22, Eq. III.7 is rewritten as:

$$\eta(\omega, \theta) = -2\gamma(\omega, \theta)\frac{c_g}{c_\varphi} \quad . \tag{III.8}$$

In general, the group velocity and the phase velocity are related by $c_g = 2c_\varphi$ for a pure bending wave propagation. For longitudinal wave or shear wave propagation, the medium is not dispersive thus $c_g = c_\varphi$.

Average loss factor

This section describes the method to calculate the average damping loss factor of non-isotropic structures [54]. The average damping loss factor of an isotropic panel can be described as:

$$< \eta(\omega) >= \frac{\int_0^{2\pi} \eta(\omega, \theta)\mathrm{d}\theta}{\int_0^{2\pi} \mathrm{d}\theta} \quad . \tag{III.9}$$

However, the relation is not applicable to non-isotropic structures because the number of modes are different in each directions and the damping loss factor varies in each direction. Therefore, a more general average loss factor formulation is given by:

$$\bar{\eta}(\omega) = \frac{\int_0^{2\pi} \eta(\omega, \theta)n(\omega, \theta)\mathrm{d}\theta}{\int_0^{2\pi} n(\omega, \theta)\mathrm{d}\theta} \quad , \tag{III.10}$$

where $n(\omega, \theta)$ is the angular modal density for each direction given by [53]:

$$n(\omega,\theta) = \frac{S}{\pi^2}\frac{k(\omega,\theta)}{c_g(\omega,\theta)} \quad . \tag{III.11}$$

Here S is the area of the structure and $k(\omega,\theta)$ and $c_g(\omega,\theta)$ are the wavenumber and the group velocity at each angle and each frequency. Finally, the average loss factor of non-isotropic structures is written as:

$$\bar{\eta}(\omega) = \frac{\int_0^{2\pi} \eta(\omega,\theta)\frac{k(\omega,\theta)}{c_g(\omega,\theta)}\mathrm{d}\theta}{\int_0^{2\pi} \frac{k(\omega,\theta)}{c_g(\omega,\theta)}\mathrm{d}\theta} \quad . \tag{III.12}$$

In this paper, the damping loss factor as function of the frequency and the angle is estimated only for the numerical orthotropic sandwich graphite-epoxy with a viscoelastic core panel, the numerical sandwich aluminium with a shape memory polymer (SMP) core panel and the experimental sandwich carbon fiber honeycomb panel. For other panels, the global average damping loss factor given in Eq. III.12 is studied and compared to reference methods.

III. 3 Numerical validations

The method described in the previous section is applied to four plane structures with different complexities: the first one is a sandwich laminated glass with a frequency dependant PVB core panel [89], the second one is an anisotropic laminate carbon fiber plate with different orientation of the fibers [56] , the third one is an orthotropic sandwich graphite-epoxy with a viscoelastic core panel [36] and the fourth one is a very high damping aluminium sandwich with a shape memory polymer core panel.

For each case, the specific objective is described as follow: 1) to investigate the limitation of the proposed method for a low damping structure; 2) to investigate the accuracy of the method for an anisotropic panel with a higher damping loss factor; 3) to investigate the ability of the proposed method to estimate the damping loss factor as function of the frequency and the heading angle of an orthotropic panel; 4) and to investigate the ability of the proposed method to estimate the damping loss factor of a very highly damped structure.

The simulations of the first, third and fourth panels are done using an in-house finite element software with solid HEXA20 elements [69, 4] and the simulations of the second panel are done using an in-house finite element software with ZPST elements [16, 51].

All the panels are subject to a central excitation with free-free boundary conditions. The calculation area of the correlation factor in Eq. III.6 is reduced by 5 cm from each boundary to minimise the effect waves generated by the reflection at boundaries. The excitation point is rejected in the correlation function due to the singularity of the Green's function at $r = 0$ (see Eq. III.5).

III. 3. 1 Sandwich laminated glass with a frequency dependent PVB core

The method is first applied to a 1 m $\times$ 1.2 m sandwich laminated glass panel with a viscoelastic polyvinyl butyral (PVB) polymer core [89, 92]. The skins are 5 mm thick glass panels (Density $\rho = 2500$ kg/m^3, Young's modulus E = 71.04 GPa, Poisson's coefficient $\nu = 0.2$ and damping $\eta_{skin} = 0.1\%$). The PVB viscoelastic core (Density $\rho_{core} = 1020$ kg/m^3 , Poisson's coefficient $\nu_{core} = 0.449$) is 0.38 mm thick and has frequency dependant Young's modulus, shear modulus, and damping ratio defined in Table III.1.

The GFC wavenumber maps at 1850 Hz and 6100 Hz are shown in Fig. III.1a-b respectively. At 1850 Hz, the maximum of the amplitude varies in function of the angle and the privileged directions of propagation is visible. At 6100 Hz, the isotropic behavior of the panel is identified. The wavenumber estimated in Fig. III.2 correlates well in the frequency range compared to the GLM.

The ratio of the group velocity over the phase velocity estimated from the dispersion curve of the laminated glass panel is shown in Fig. III.3. Below 6000 Hz, the ratio approaches 2 which corresponds to pure bending wave. Above 6000 Hz, the ratio approaches 1, the shear wave propagation dominates the global behavior of the system.

The damping loss factor identification is presented in Fig. III.4. The result is compared

Frequency (Hz)	Shear Modulus (Pa)	Damping	Young's Modulus (Pa)
10	5.50E+07	0.46	1.65E+00
50	8.30E+07	0.27	2.49E+08
100	9.17E+07	0.24	2.75E+08
200	1.03E+08	0.21	3.08E+08
500	1.14E+08	0.15	3.42E+08
1000	1.21E+08	0.14	3.63E+08
2000	1.30E+08	0.12	3.90E+08
5000	1.38E+08	0.07	4.13E+08
10000	1.40E+08	0.04	4.19E+08
20000	1.41E+08	0.02	4.23E+08
30000	1.42E+08	0.02	4.24E+08

Table III.1: Properties of the sandwich laminated glass core.

with the GLM in which a power balance equation is used to estimate the loss factor [36]. The estimation using the Green's function-based model is in good agreement with the reference solution above 1000 Hz. Below 1000 Hz, the GFC overestimates the damping loss factor due to the modal behavior of the panel.

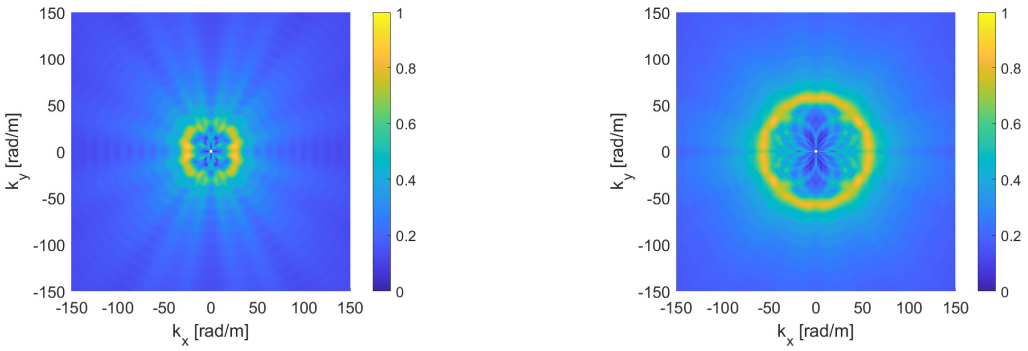

(a) 1850 Hz (b) 6100 Hz

Figure III.1: GFC wavenumber maps of the numerical sandwich laminated glass panel at 1850 Hz and 6100 Hz.

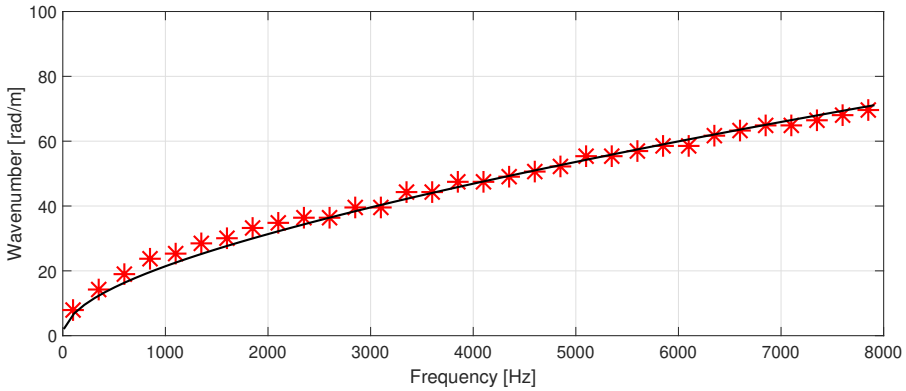

Figure III.2: Comparison of the dispersion curve of the numerical sandwich laminated glass panel. - GLM and * GFC.

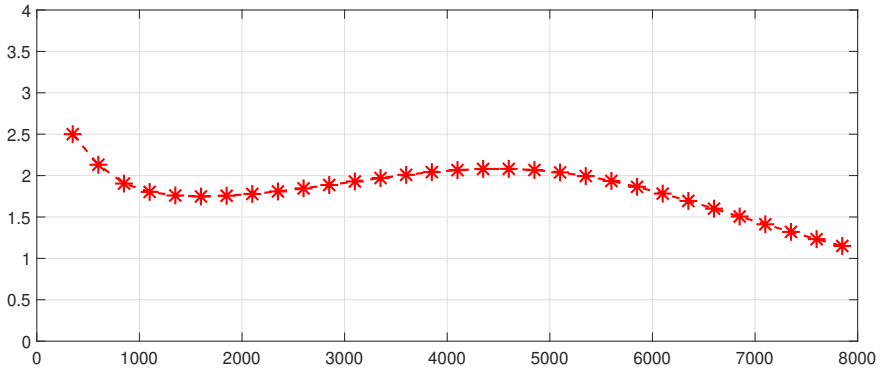

Figure III.3: Ratio of the group velocity over the phase velocity of the numerical sandwich laminated glass panel.

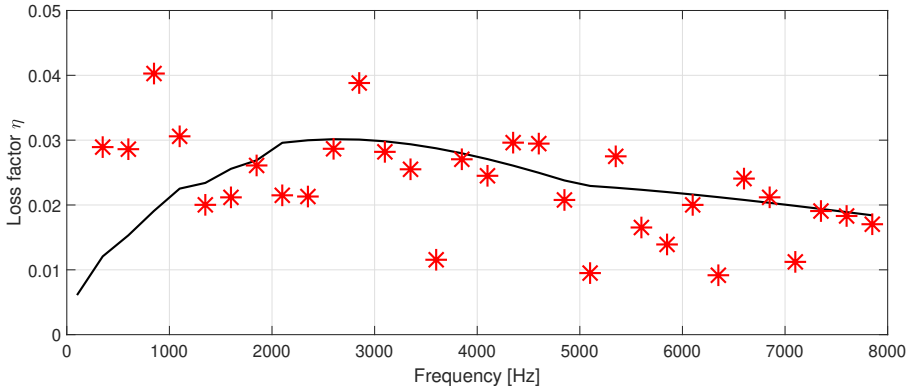

Figure III.4: Comparison of the damping loss factor of the numerical sandwich laminated glass panel.- GLM and * GFC.

III. 3. 2 Anisotropic laminate composite panel

The proposed method is applied to a 1 × 1.2 m^2 carbon fiber composite panel with different orientations of the fibers (60°/-60°/-60°/60°) [56]. The mechanical properties of the panel are shown in Table III.2.

The GFC wavenumber maps at 3600 Hz and 6100 Hz of the proposed method are shown in Fig. III.5a-b respectively. For both frequencies, the anisotropic behavior of the panel is visible and a good agreement with the GLM is demonstrated. The dispersion curves at 0°, 30°, 60° and 90° are shown in Fig. III.6. The results show a very good agreement compared to the GLM on the entire frequency range and for all four directions.

The damping loss factor is compared to the GLM energy based estimation in Fig. III.7. The proposed method shows a good correlation compared to the GLM above 1500 Hz. Below 1500 Hz, the GFC method shows some discrepancies due to the modal behavior of the panel which is ignored in the free field Green's function used in the proposed method.

	h	ρ	E_x	E_y	G_{xy}	ν_{xy}	η
Parameters	0.187 mm	1540 kg/m^3	133 GPa	8.8 GPa	6.6 GPa	0.31	5%

Table III.2: Optimal material parameters of one layer of the composite plate given by Marchetti et al. [56].

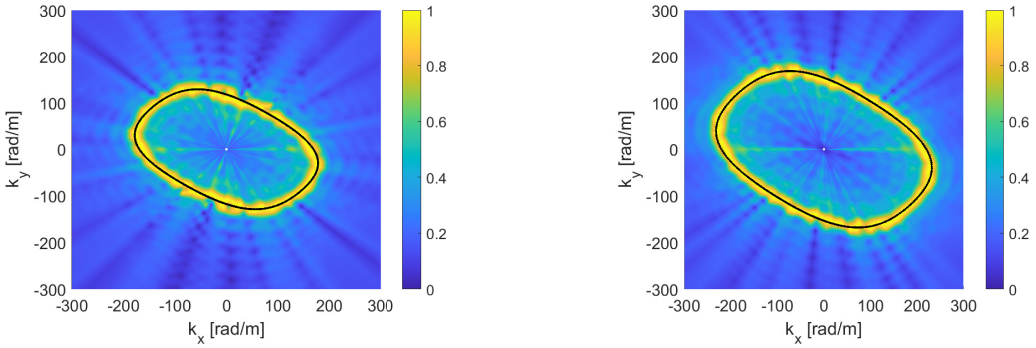

(a) 3600 Hz (b) 6100 Hz

Figure III.5: GFC wavenumber maps of the numerical laminated composite panel at 3600 Hz and 6100 Hz. The black line shows the flexural wavenumber estimation using the GLM.

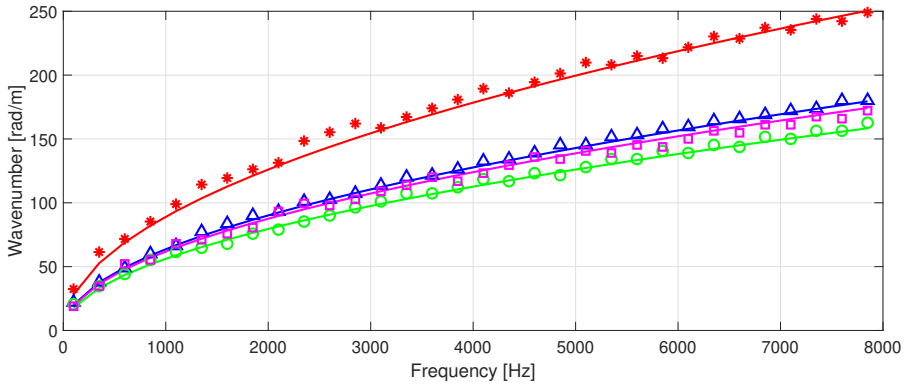

Figure III.6: Comparison of the dispersion curve of the numerical laminated composite panel. — 0° GLM, — 30° GLM, — 60° GLM and — 90° GLM. ∗ 0° GFC, △ 30° GFC, ○ 60° GFC and □ 90° GFC.

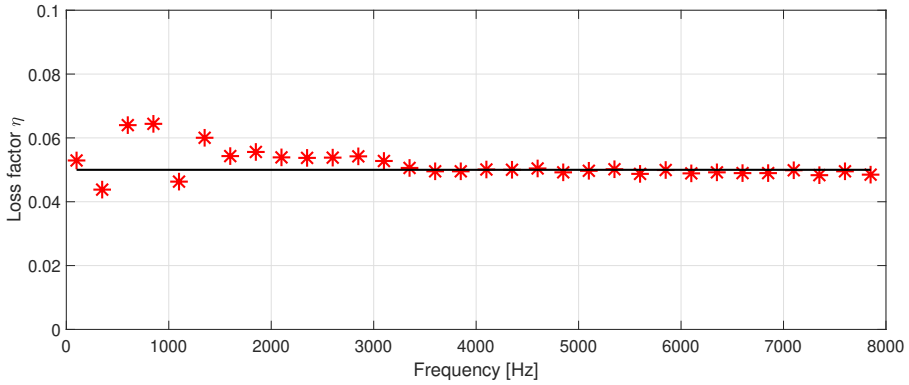

Figure III.7: Comparison of the damping loss factor of the numerical laminated composite panel. - GLM and ∗ GFC.

III. 3. 3 Orthotropic sandwich graphite-epoxy with a viscoelastic core

The method is applied to an orthotropic 1 m × 1.2 m sandwich graphite-epoxy with a viscoelastic core. The mechanical properties of the panel are defined in Table III.3.

The wavenumbers estimation at two different angles, 0° and 90°, are shown in Fig. III.8. The proposed method shows a good correlation in both directions compared with the GLM on the entire frequency range.

The damping loss factor as function of the heading angle from 0 to $\pi/2$ is shown in Fig. III.9b and compared to the GLM in Fig. III.9a [36]. In the low frequency range below 250 Hz, the maxima of the damping loss factor from 0 to $\pi/2$ shows discrepancies compared to the GLM due to the free field behavior assumed in the Green's function which is not respected in practice. Above 250 Hz, the variation of the overall damping from 0 to $\pi/2$ shows the effect of the orthotropy of the skin on the estimation of the damping loss factor. The damping loss factor maxima vary in function of the frequency and the heading angle.

The estimation of the damping loss factor of the panel along three different directions (0°, 45° and 90°) is shown in Fig. III.10. At 0°, the result shows a good correlation

	Skins	Core
h (mm)	1.52	0.127
E_1 (GPa)	125	0.0021
E_2 (GPa)	12.5	0.0021
E_3 (GPa)	125	0.0021
G_{12} (GPa)	5.9	0.0007
G_{13} (GPa)	3	0.0007
G_{23} (GPa)	5.9	0.0007
ν_{12}	0.4	0.499
ν_{13}	0.032	0.499
ν_{23}	0.4	0.499
ρ (kg/m^3)	1600	970
η (%)	1	50

Table III.3: Mechanical properties of the orthotropic sandwich graphite-epoxy with a viscoelastic core panel [36].

compared to the GLM above 1500 Hz. Below, the proposed method overestimates the damping loss factor. At 45°, a good correlation above 500 Hz compared to the GLM is visible. At 90°, the proposed method shows a good correlation compared to the GLM above 500 Hz.

The heading angle modal density averaged (see Eq. 12) damping loss factor is presented in Fig. III.11. A good correlation compared to the GLM in the frequency range above 500 Hz is visible.

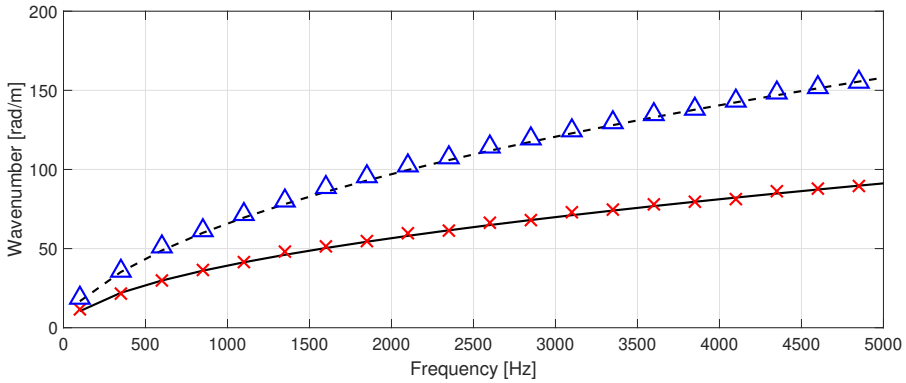

Figure III.8: Comparison of the dispersion curve of the numerical sandwich graphite-epoxy with a visceolastic core. - 0° GLM ,- - 90° GLM, × 0° GFC and △ 90° GFC.

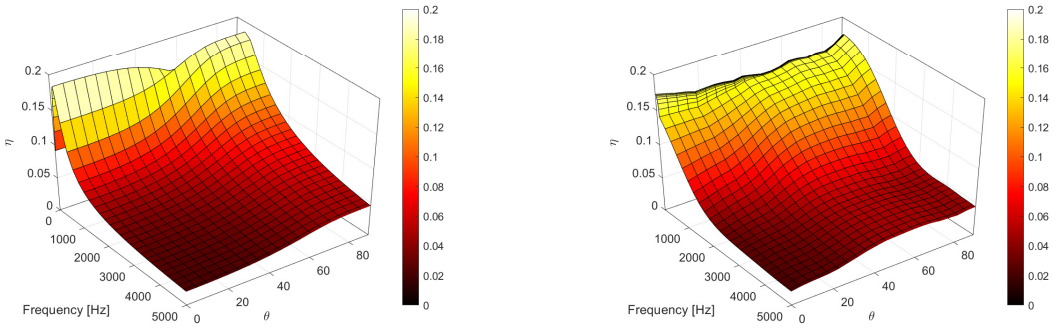

(a) GLM [36]. (b) GFC.

Figure III.9: Comparison of the damping loss factor of a sandwich graphite-epoxy with a viscoelastic core panel as function of the frequency and the heading angle from 0 to $\pi/2$.

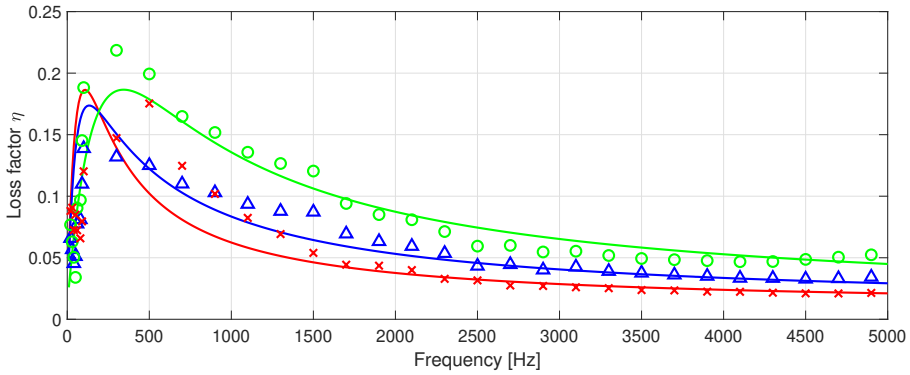

Figure III.10: Damping loss factor at 0°, 45° and 90° of a sandwich graphite-epoxy with a viscoelastic core panel. — 0° GLM, — 45° GLM and — 90° GLM. × 0° GFC, △ 45° GFC and ○ 90° GFC.

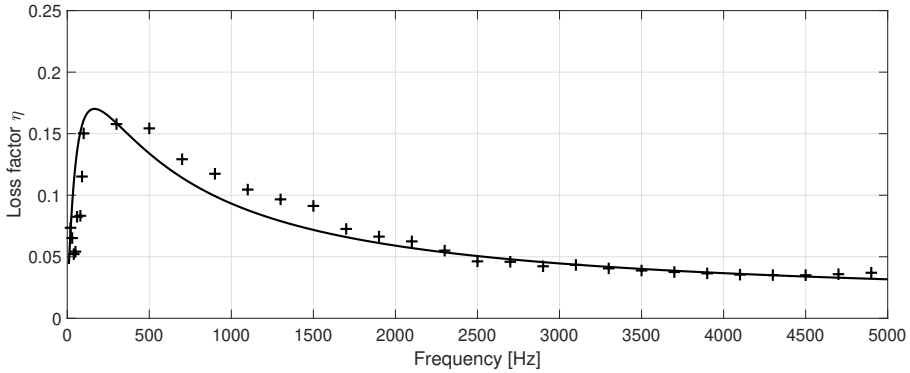

Figure III.11: Heading angle modal density averaged damping loss factor panel of a sandwich graphite-epoxy with a viscoelastic core panel. — GLM and + GFC.

III. 3. 4 High damping loss factor sandwich aluminium with a shape memory polymer (SMP) core panel

The method is applied to a 0.5 m × 0.6 m aluminium sandwich with a Shape Memory Polymer (SMP) viscoelastic core at 65°C [14]. This structure has a very high damping loss factor. The skins are 0.5 mm thick aluminium panel (Density ρ = 2700 kg/m^3, Young's modulus E = 70 GPa, Poisson's coefficient ν= 0.33 and damping η_{skin}=0.1%). The rheological properties of the 2.2 mm SMP viscoelastic is described by Butaud [15]:

$$E^*(\omega, T) = E_0 + \frac{E_\infty - E_0}{1 + \gamma(j\omega\tau)^{-k} + (j\omega\tau)^{-h} + (j\omega\beta\tau)^{-1}} \quad , \tag{III.13}$$

where E_0 is the rubber modulus when $\omega \to 0$, E_∞ is the glassy modulus when $\omega \to \infty$, τ is the characteristic time, estimate by the Time-Temperature Superposition Principle:

$$\tau(T) = a_T(T).\tau_0 \quad , \tag{III.14}$$

where $a_T(T)$ is the shift factor at the temperature T and $\tau_0 = \tau(T_0)$ is determined at the reference temperature T_0. The constants k, h, γ and β defined in Eq. III.13 are represented in Table III.4. The Young's modulus and the damping loss factor of the SMP viscoelastic core are shown in III.12.

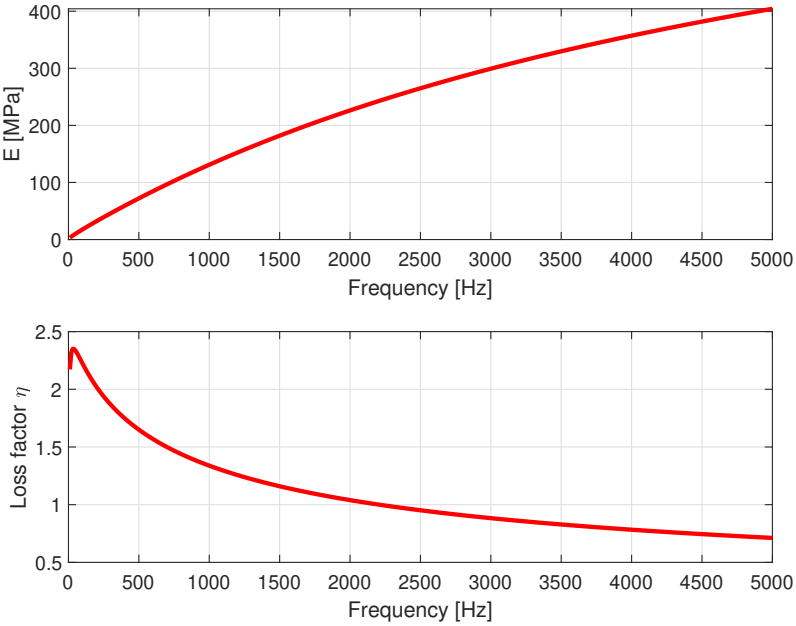

Figure III.12: The Young's modulus and the damping loss factor of the Shape Memory Polymer(SMP) viscoelastic at 65°C.

The GFC wavenumber maps at 500 Hz and 1900 Hz are demonstrated in Fig III.13a-b respectively. The isotropic behavior of the panel are visible in both frequencies. The wavenumber estimated in Fig. III.14 is compared to the GLM and the classical IWC method. For the IWC method, the panel is subject to an excitation near the edge (x_0 = 0.1 m, y_0 = 0.1 m) and the observation window of the IWC calculation is taken outside of the

source for the best condition of the plane wave hypothesis. The wavenumber identification of both IWC and GFC methods shows good agreement compared to the theoretical model.

The average damping loss factor estimation is presented in Fig. III.15. The GFC method shows a very good agreement in the frequency range above 500 Hz compared to the GLM. Below 500 Hz, the method shows some discrepancies due to the modal behavior of the panel which is ignored in the free field Green's function used in the proposed method. The classical IWC method shows discrepancies below 4500 Hz due to the limitation of the plane wave hypothesis. The reliability of the GFC method is estimating the damping loss factor is demonstrated in this very high damping loss factor configuration where the contribution of the reflection waves at boundaries are very low.

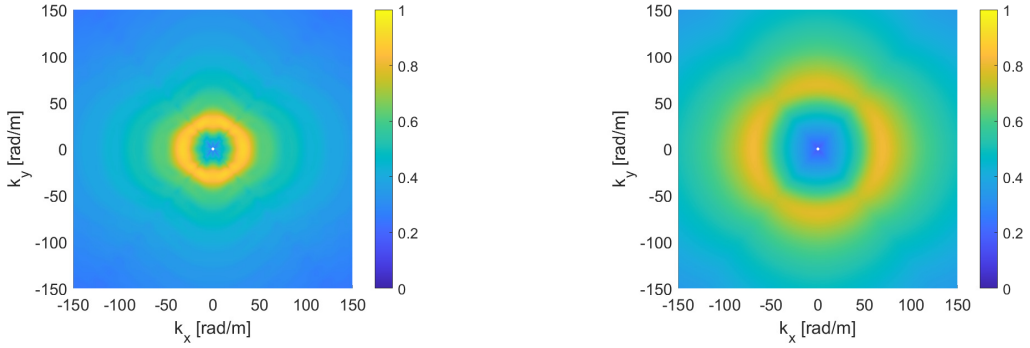

(a) 500 Hz (b) 1900 Hz

Figure III.13: GFC wavenumber maps of the numerical sandwich aluminium SMP panel at 500 Hz and 1900 Hz.

E_0(MPa)	E_∞(MPa)	k	h	γ	β	τ_0(s)
0.67	2211	0.16	0.79	1.68	3.8e4	0.61

Table III.4: Parameters of the constants of the aluminium SMP core [15].

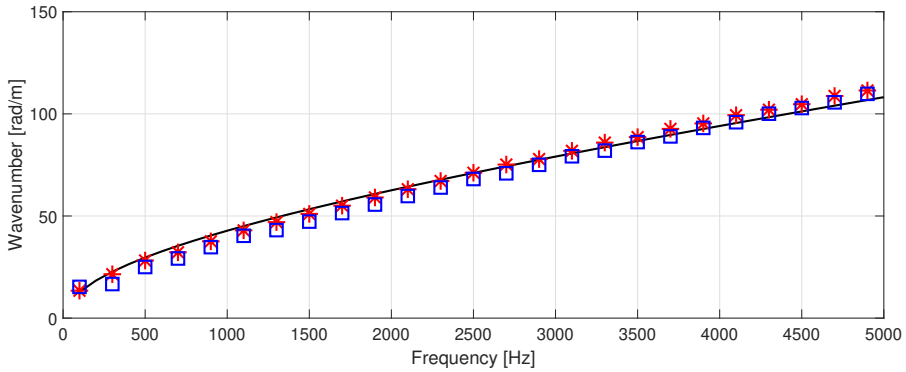

Figure III.14: Comparison of the dispersion curve of the numerical sandwich aluminium SMP panel. - GLM, □ IWC and * GFC.

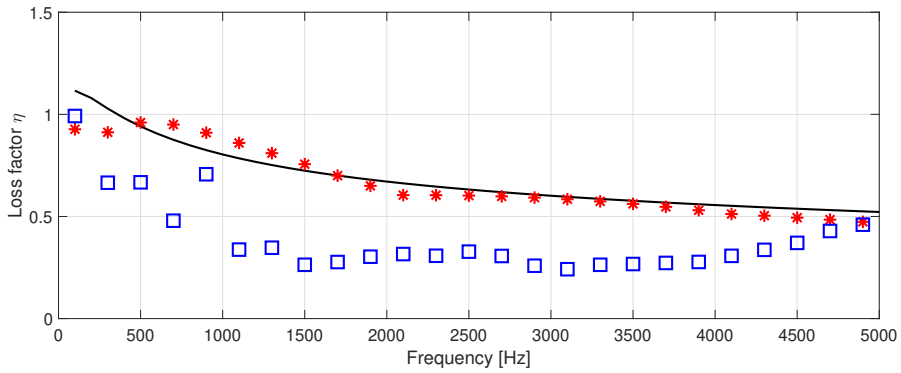

Figure III.15: Comparison of the damping loss factor of the numerical sandwich aluminium SMP panel.- GLM, □ IWC and ∗ GFC.

III. 4 Experimental validation

A sandwich carbon fiber honeycomb panel (Fig. III.17) of dimensions 1 m × 1.5 m and total thickness of 27.3 mm has been experimentally investigated. The plate was excited by a point mechanical force via a stringer and an impedance head using a SmartShaker™ K2007E01 with a maximum frequency range of 9000 Hz. The study is conducted in a large frequency band from 50 Hz to 8000 Hz with $\Delta f = 6.25$ Hz using white noise signal. The panel was freely hung with flexible cords and the shaker is attached at the back of the panel. The out of plane vibrational field is measured using a Polytec PSV-500 Scanning Vibrometer. The scan is performed with the mesh size of 17 mm × 17 mm and the measurement is averaged over 25 times for each point. The schematic diagram of the experimental set up is shown in Fig. III.16.

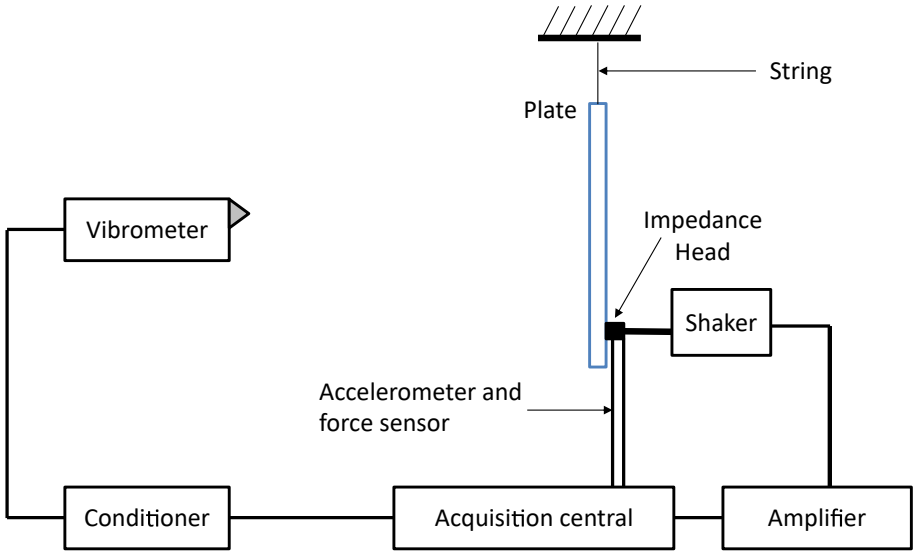

Figure III.16: Schematic diagram of the experimental set up.

Figure III.17: Sandwich carbon fiber honeycomb panel.

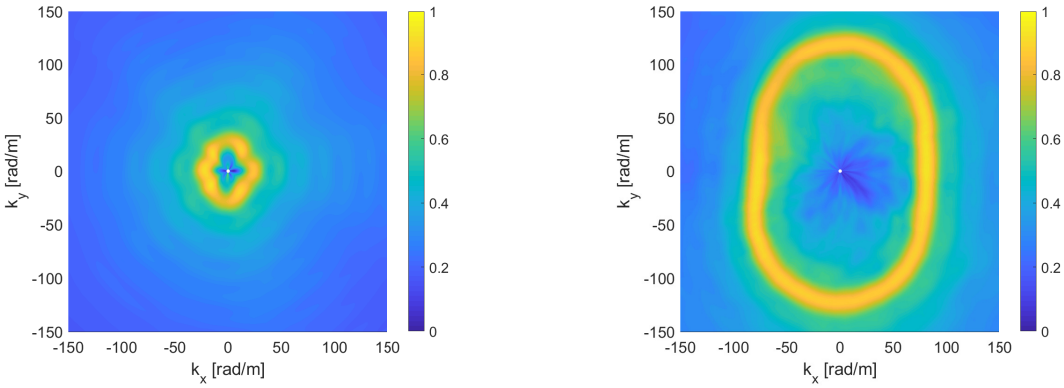

(a) 1300 Hz (b) 7550 Hz

Figure III.18: GFC wavenumber maps of the dispersion of the experimental sandwich carbon fiber honeycomb panel at 1300 Hz and 7550 Hz.

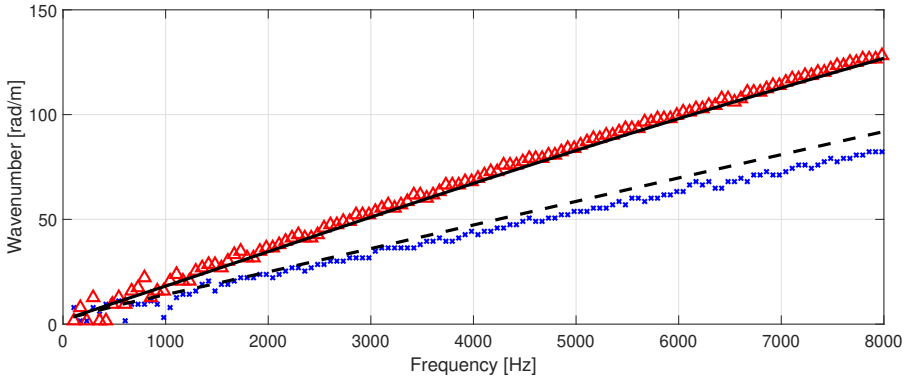

Figure III.19: Comparison of the dispersion of the experimental sandwich carbon fiber honeycomb panel. - - GLM 0°,- GLM 90°, x GFC 0° and △ GFC 90°.

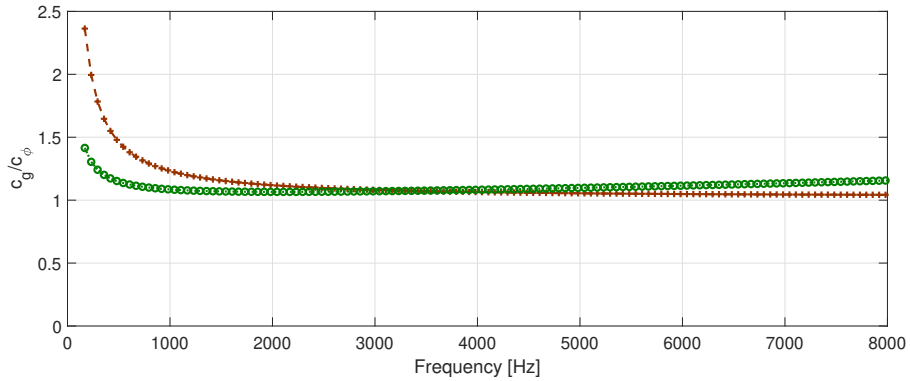

Figure III.20: Ratio of the group velocity over the phase velocity (c_g/c_φ). -+- ratio at 0° and - ○ - ratio at 90° of the experimental sandwich carbon fiber honeycomb panel.

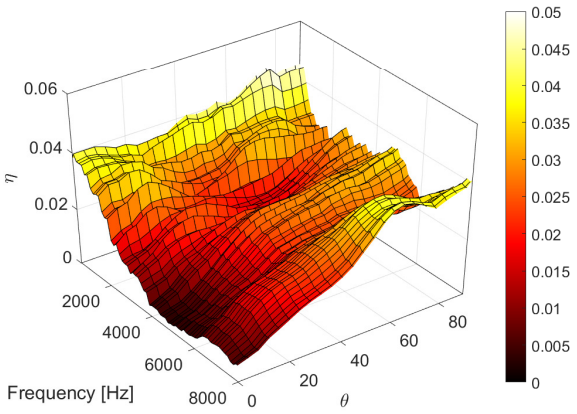

Figure III.21: Damping loss factor of the experimental sandwich carbon fiber honeycomb panel as function of the frequency and the heading angle from 0 to $\pi/2$.

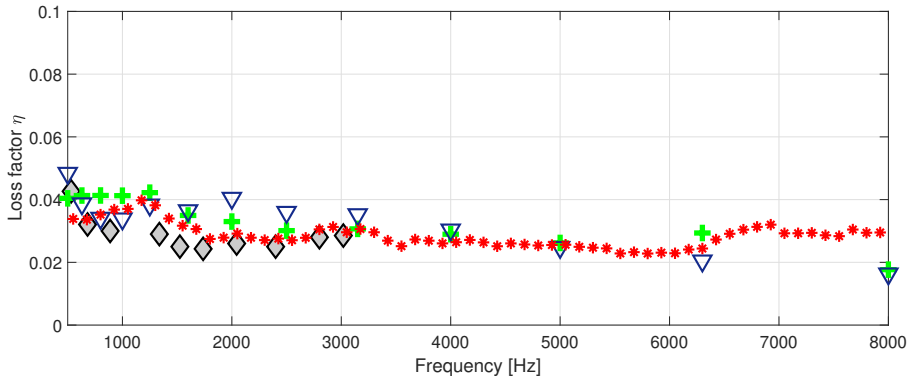

Figure III.22: Heading angle modal density averaged damping loss factor estimation of the experimental sandwich carbon fiber honeycomb panel compared to reference methods. ◇ 3dB method, + power input method, ▽ decay rate method and * GFC method.

Results and discussion

The GFC wavenumber maps at 1300 Hz and 7550 Hz are presented in Fig. III.18a-b respectively. The non-isotropic behavior of the panel is visible at both frequencies. The wavenumbers measurement of the experimental panel at 0° and 90° are shown in Fig. III.19. The results are compared to the reference solution based on the general laminate model (GLM) [36] using the properties defined in Table III.5.

	Skins	Core
h (mm)	0.96	25.4
E_1 (GPa)	46	0.001
E_2 (GPa)	46	0.001
E_3 (GPa)	46	0.179
G_{12} (GPa)	17.6	1
G_{13} (GPa)	17.6	26
G_{23} (GPa)	17.6	56
ν_{12}	0.3	0.45
ν_{13}	0.3	0.01
ν_{23}	0.3	0.01
ρ (kg/m3)	1900	64

Table III.5: The mechanical properties of the sandwich carbon fiber honeycomb panel [21].

In the frequency domain below 1000 Hz, the estimation is less accurate compared to the GLM model due to the modal behavior of the panel. Besides the localisation of the maximum for each direction is difficult at these frequencies. Between 1000 Hz and 5000 Hz, the wavenumber at 0° shows good agreement compared to the reference. Above 5000 Hz, both experimental and theoretical dispersion curves at 0° show small divergence. This error maybe due to the uncertainty of the material properties used in the reference GLM model predictions. At 90°, the estimation of the wavenumber shows good agreement compared to the theoretical dispersion in the full frequency range.

The ratio c_g/c_φ is shown in Fig. III.20. In the low frequency range, the ratio approaches 2 which corresponds to the flexural wavenumber of the entire panel cross section. In the mid frequency range, the ratio approaches 1 indicating that the wave propagation is controlled by the shear stiffness of the core.

The damping loss factor as function of the frequency and the heading angle from 0 to $\pi/2$ is presented in Fig. III.21. The fluctuations of the damping loss factor in some of the directions are certainly due to the measurement errors. The variation of the damping loss factor in function of the frequency and the heading angle is visible. The scatter of the damping loss factor maxima is due to a non-isotropic behavior of the core.

The average damping loss factor estimation using Eq. III.12, is presented in Fig. III.22 and compared to the 3dB method, the decay rate method and the power input method. The 3dB method is limited to the low frequency range. The decay rate method and the power input method are expressed in a third octave frequency band.

In the mid frequency range, the power input, the decay rate and the proposed method show good agreement. At low frequency below 500 Hz, the power input method overes-

timates the damping loss factor due to the low number of modes which is the limitation of the Statistical Energy Analysis (SEA) method [53]. At high frequency range above 2000 Hz, a good agreement between the proposed method, the decay rate method and the power input method can be demonstrated. The discrepancies observed above 6000 Hz are certainly associated with the limitation of the mesh used to scan the displacement field.

III. 5 Conclusion of the paper

A wave correlation method is proposed to estimate the wavenumber and in particular, the damping loss factor of non-isotropic planar structures as a function of the heading angle. The efficiency of the method is demonstrated both numerically and experimentally by comparison with reference methods.

In general, the comparison of the dispersion curve and the damping loss factor between the proposed identification technique and the reference solution are good for both numerical and experimental studies. For the dispersion relation, the technique is able to predict precisely the wavenumber on the entire frequency range. For the damping loss factor, the method is much more accurate in high damping structures due to the assumption of the technique itself where only direct field is considered in the correlation calculation. For low damping structures and low frequency range, the method shows some discrepancies and is relatively less accurate due to the reflection at boundaries. An application of the image source method can be done to take into account the reflection at boundaries and to improve the damping loss factor estimation especially for low damping structures.

The experimental demonstration of the efficiency of the proposed method on the sandwich carbon fiber with a honeycomb core opens the possibility to apply this technique experimentally on more complex structures such as stiffened panels and curved structures.

Acknowledgement The authors would like to thank the Hauts-de-France Region, the Natural Sciences and Engineering Research Council of Canada (NSERC) and the Consortium for Aerospace Research and Innovation of Québec (CRIAQ) for their financial support.

End of the paper

In the wavenumber domain, the damping loss factor is related to its imaginary and is very sensitive to measurement uncertainties. Usually, a central excitation is considered in applying the Green's function to avoid any privileged directions of wave propagation.

This part is a complementary work to this chapter investigating the impact of different excitation locations on the estimation of the wavenumber and the damping loss factor. A correction of the estimation of the damping loss factor based on the precision of the wavenumber maps is applied. Based on the results, the choice of the excitation location is very important in applying the Green's function correlation method.

III. 6 Effect of the excitation location on the damping loss factor estimation using Green's function correlation method

The estimation of the flexural wavenumber and the damping loss factor is very crucial as both of them are strongly related to the sound radiation and the noise level generated by this radiation. Methods such as the High Resolution Wavenumber Analysis [59, 60], the Inhomogeneous Wave Correlation Method [7] and the Green's function [75, 85, 57] have been successfully developed to estimate the real and the imaginary parts of the wavenumber of complex structures. However, uncertainties of the estimation of the wavenumber and the damping loss factor due to the selection of the excitation locations are less discussed whereas these uncertainties may impact the validity of the results.

In most cases, a central excitation is considered to avoid any privileged direction of wave propagation. In reality, a central excitation of the panel can sometimes be inaccessible and may not excite all modes. In this chapter, the effect of the excitation locations on the estimation of the wavenumber and the damping loss factor as a function of the wave propagating angle is investigated. Three different excitation coordinates are used. The first is near the boundaries, the second is at the center and the third is near a corner. The performance of each excitation position to estimate the wavenumber and the damping loss factor is investigated.

A methodology to rectify the error on the estimation of the damping loss factor in function of the excitation coordinates is introduced. This rectification allows a good estimation of the average damping loss factor for any excitation coordinates. The method is investigated numerically using an isotropic sandwich aluminium panel with a viscoelastic core and is tested experimentally on a thick sandwich composite panel with a honeycomb core.

III.7 Excitation location: numerical investigation

Three different excitation coordinates are defined. The first one is at $x_{0_1} = 0.2$ m and $y_{0_1} = 0.4$ m. The second one is the central excitation at $x_{0_2} = 0.5$ m and $y_{0_2} = 0.6$ m . The third one is an excitation near the edge at $x_{0_3} = 0.8$ m and $y_{0_3} = 0.2$ m.

The calculation area of the correlation factor in Eq. III.6 is reduced by 5 cm from each boundary to minimise the effect of waves generated by the reflection at boundaries. The excitation point is rejected in the correlation function due to the singularity of the Green's function at $r = 0$ (see Eq. III.5). The schematic presentation of the three excitation points is shown in Fig. III.23.

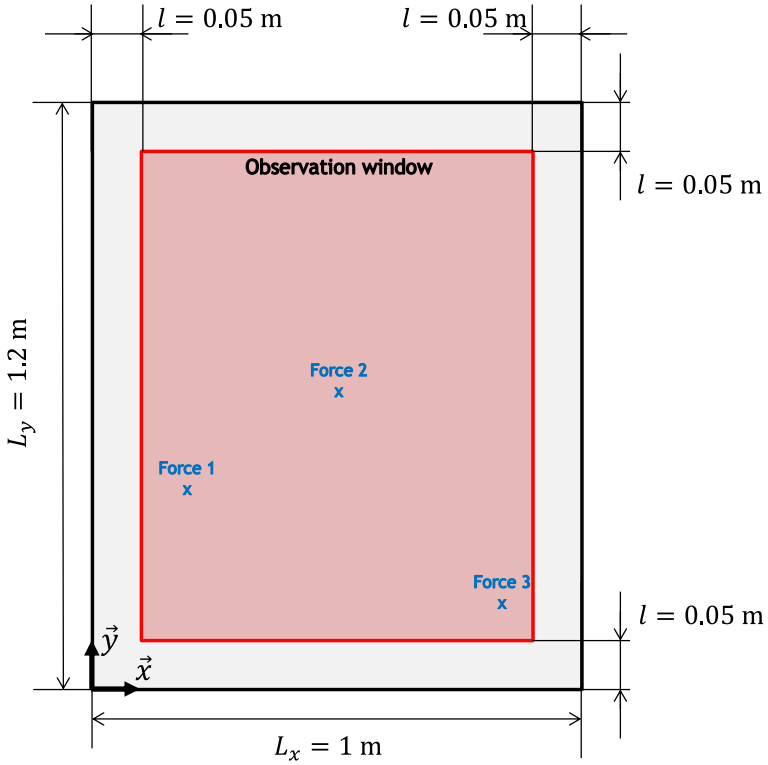

Figure III.23: Schematic presentation of the panel with three different excitation points.

The method is first applied to a 1 m × 1.2 m sandwich aluminium panel with a viscoelastic core. The skins are 2 mm thick aluminium (Density $\rho = 2700$ kg/m^3, Young's modulus E = 71 GPa, Poisson's coefficient ν= 0.33 and damping η_{skin}=1%). The core is a 0.76 mm thick viscoelastic material (Density $\rho = 900$ kg/m^3, Young's modulus E = 1 GPa, Poisson's coefficient ν= 0.49 and damping η_{core}=20%).

The normal displacements **w** of the panel for three point load locations at 7100 Hz are shown in Fig. III.24a-b and the Green's function-based model correlation (GFC) wavenumber maps at 2350 Hz and 7100 Hz are shown in Figs. III.25 and III.26 respectively.

At 2350 Hz, the maximum of the amplitude in the $-k_x$ area for the first excitation and the maximum of the amplitude in the $(+k_x, -k_y)$ area for the third excitation are

noisy as shown in Fig. III.25a and in Fig. III.25c respectively. The isotropic behavior is less pronounced and the maximum amplitude for each angle is not easily identifiable. The discrepancies are due to the limitation of the panel length in these directions. For the second excitation where the panel is subject to a central excitation, the maximum of amplitude is constant in all directions and the isotropic behavior is clearly visible as shown in Fig. III.25b.

At 7100 Hz, the maximum of the amplitude in the $-k_x$ area for the first excitation and the maximum of the amplitude in the $(+k_x, -k_y)$ area for the third excitation depict more incertitude as shown in Fig. III.26a and in Fig. III.26c respectively. Nevertheless, the isotropic behavior of the panel are still identifiable compared to the case at 2350 Hz. The maximum of the wavenumber for each angle is visible on the wavenumber maps. For the second excitation, the maximum of amplitude is constant in all directions and the isotropic behavior is clearly visible as shown in Fig. III.26b.

The estimation of the average damping loss factor is demonstrated in Fig. III.27. As can be seen, the estimation of the imaginary part related to the damping loss factor is much more sensitive to measurement uncertainties compared to the real part. The estimation of the damping loss factor using the central excitation location shows a very good correlation compared to the reference solution based on the generate laminate model (GLM) [36]. For the first excitation, the average damping loss factor shows a good correlation above 6000 Hz. Below 6000 Hz, the result is less precise. For the third excitation, the result is less accurate on the entire frequency range. The discrepancies for both first and third excitation locations are due to the erroneous estimation of the attenuation factor $\gamma(\theta, \omega)$ in some of the wave propagation angle. A spatial angular filter is clearly needed for these latter configurations.

In order to visualize clearly the effect, the damping loss factor as a function of the frequency and the wave propagating angle map is shown in Fig. III.28a-c. For the second excitation in which the estimation is the most accurate as shown in Fig. III.28b, the damping loss factor is relatively constant for all wave propagating angles above 2000 Hz due to the quasi-constant wave propagation radius of the panel in all directions. However for the first and the third excitation as shown in Fig. III.28a and Fig. III.28c respectively, the damping loss factor estimations show discrepancies along some wave propagation angles. These erroneous values cause divergence in the average damping loss factor calculation using Eq. III.12. To overcome this limitation, a methodology to rectify the discrepancies as function of the domain of applicability is proposed in the next section.

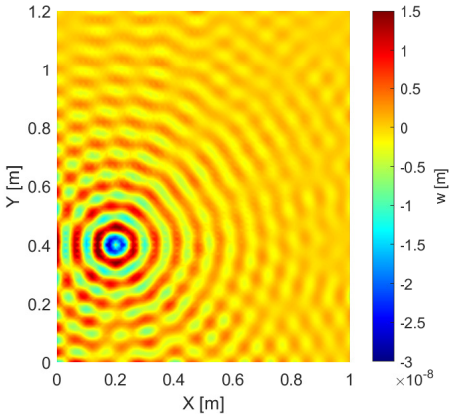

(a) $x_{0_1} = 0.2$ m and $y_{0_1} = 0.4$ m.

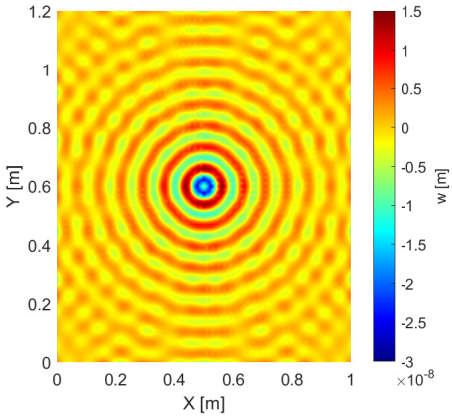

(b) $x_{0_2} = 0.5$ m and $y_{0_2} = 0.6$ m.

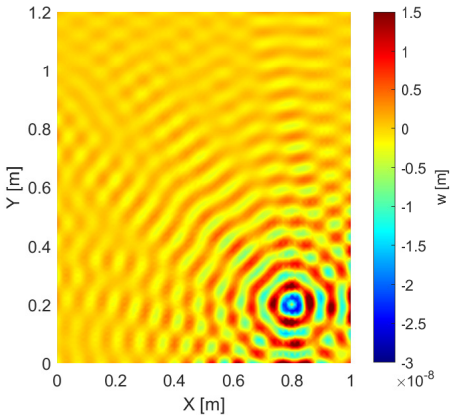

(c) $x_{0_3} = 0.8$ m and $y_{0_3} = 0.2$ m.

Figure III.24: Normal displacements **w** of the aluminium viscoelastic panel at 7100 Hz for three point load locations.

Correction of the estimation of the damping loss factor

Based on the damping loss factor as a function of the frequency and the wave propagating angle maps shown in Fig. III.28, a rectification on the estimation of the damping loss factor is applied. Instead of calculating the average damping loss factor by taking the damping values of all directions, the estimation is made only in the domain where the result is not erroneous due to the limitation of the panel length in certain directions. Red lines and arrows in Figs. III.25-III.26 define the applicable domain for the correction of the estimation of the damping loss factor.

For each case, the domain of the angle to calculate the average damping loss factor is defined in Table. III.6. The definition of the domain is made based on the precision of the amplitude of the GFC wavenumber maps (see Figs. III.25a-c and Figs. III.26a-c).

The result of the rectified average damping loss factor is shown in Fig. III.29. The estimation of the damping loss factor for the first and third excitation have been globally improved compared to the previous estimation in Fig. III.27.

The GFC method performs at best when the panel is subjected to a mechanical point load excitation at the center of the panel. In reality, a central excitation of the panel can

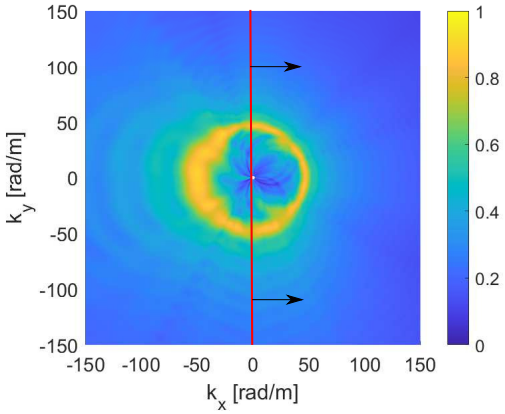

(a) $x_{0_1} = 0.2$ m and $y_{0_1} = 0.4$ m.

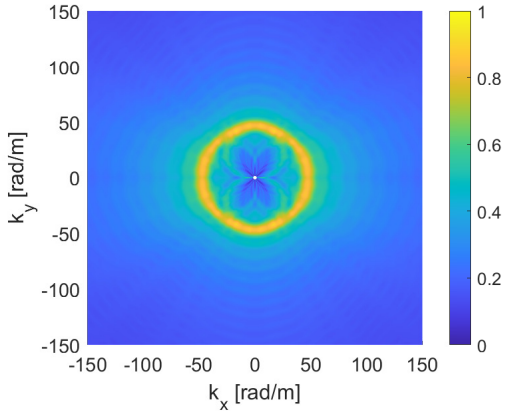

(b) $x_{0_2} = 0.5$ m and $y_{0_2} = 0.6$ m.

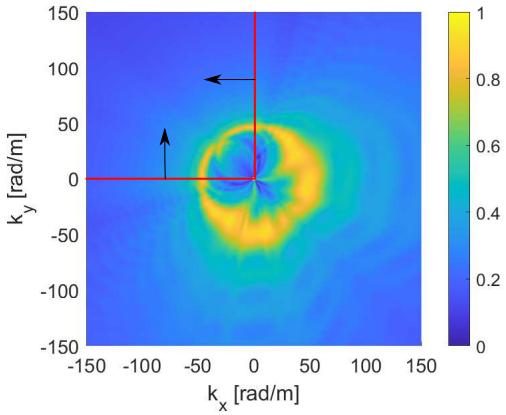

(c) $x_{0_3} = 0.8$ m and $y_{0_3} = 0.2$ m.

Figure III.25: GFC wavenumber maps of the aluminium viscoelastic panel at 2350 Hz for three point loads locations. Red lines and arrows define the applicable domain for the correction of the estimation of the damping loss factor.

Case	Applicable domain θ
1	$[-\frac{\pi}{2}; \frac{\pi}{2}]$
2	$[0; 2\pi]$
3	$[\frac{\pi}{2}; \pi]$

Table III.6: Applicable domain in calculating the average damping loss factor.

sometimes be inaccessible and may not excite all modes. The interest of the correction method is to be able to apply the GFC method for other excitation locations. For the first excitation, a very good correlation between the estimated result and the reference solution is observed above 1000 Hz. The performance of the proposed method to estimate the damping loss factor is as good as the first case. For the third excitation, a good agreement is seen above 3000 Hz and below this frequency, the method underestimates the damping loss factor. The discrepancies shown by the third excitation is certainly due to the impact of the excitation near the corner that causes greater reflections of boundaries.

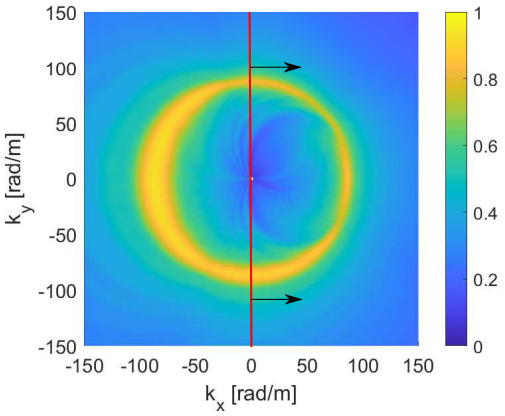

(a) $x_{0_1} = 0.2$ m and $y_{0_1} = 0.4$ m.

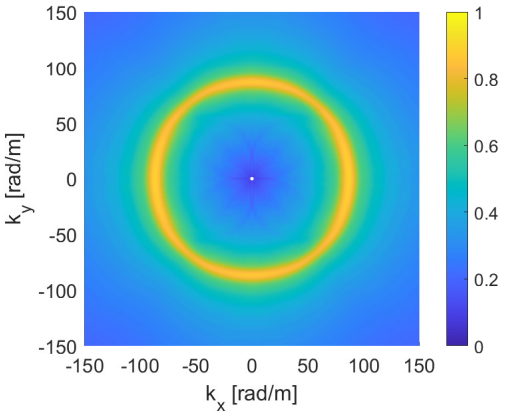

(b) $x_{0_2} = 0.5$ m and $y_{0_2} = 0.6$ m.

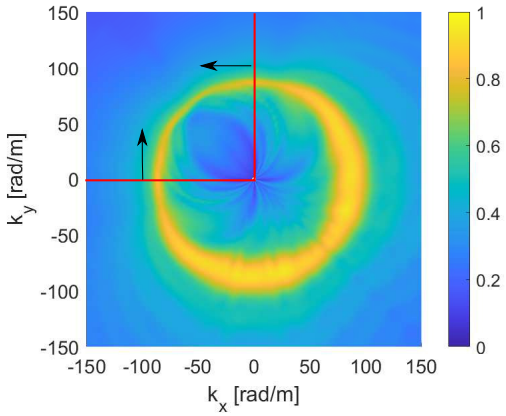

(c) $x_{0_3} = 0.8$ m and $y_{0_3} = 0.2$ m.

Figure III.26: GFC wavenumber maps of the aluminium viscoelastic panel at 7100 Hz for three point loads locations. Red lines and arrows define the applicable domain for the correction of the estimation of the damping loss factor.

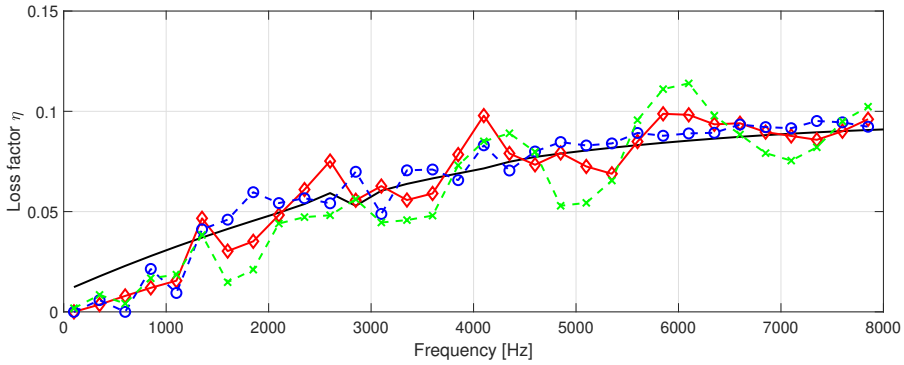

Figure III.27: Average damping loss factor of the aluminium viscoelastic panel. —◇— $x_{0_1} = 0.2$ m and $y_{0_1} = 0.4$ m, — ○ — $x_{0_2} = 0.5$ m and $y_{0_2} = 0.6$ m, -×- $x_{0_3} = 0.8$ m and $y_{0_3} = 0.2$ m and - GLM.

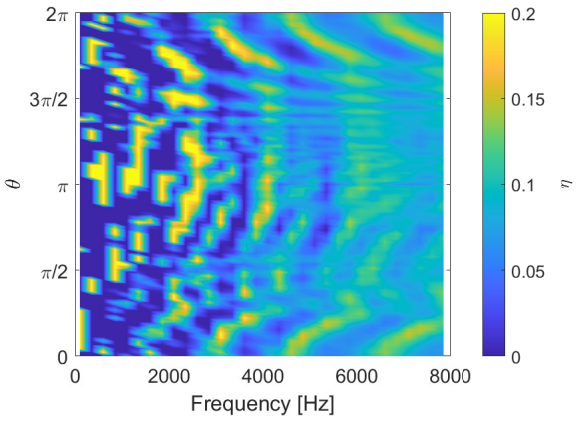

(a) $x_{0_1} = 0.2$ m and $y_{0_1} = 0.4$ m.

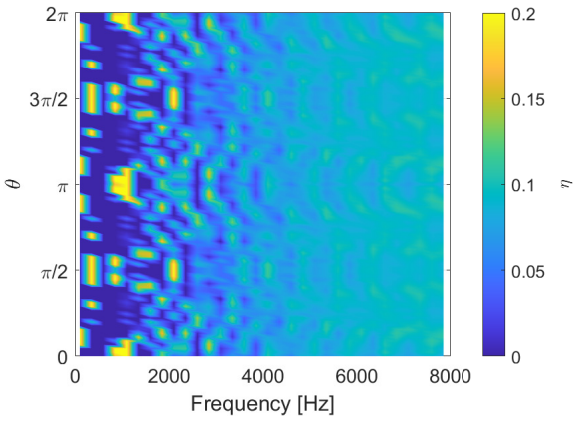

(b) $x_{0_2} = 0.5$ m and $y_{0_2} = 0.6$ m.

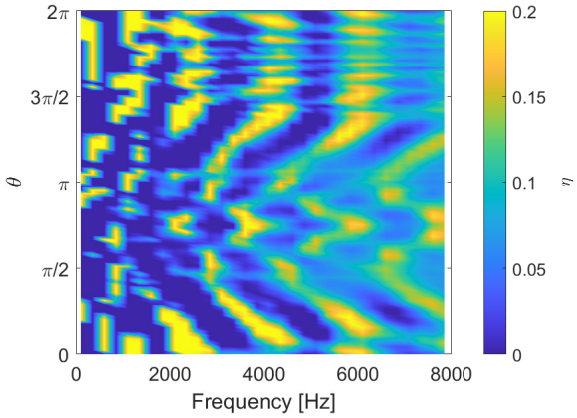

(c) $x_{0_3} = 0.8$ m and $y_{0_3} = 0.2$ m.

Figure III.28: Damping loss factor as a function of the frequency and the wave propagating angle of the sandwich aluminium viscoelastic panel.

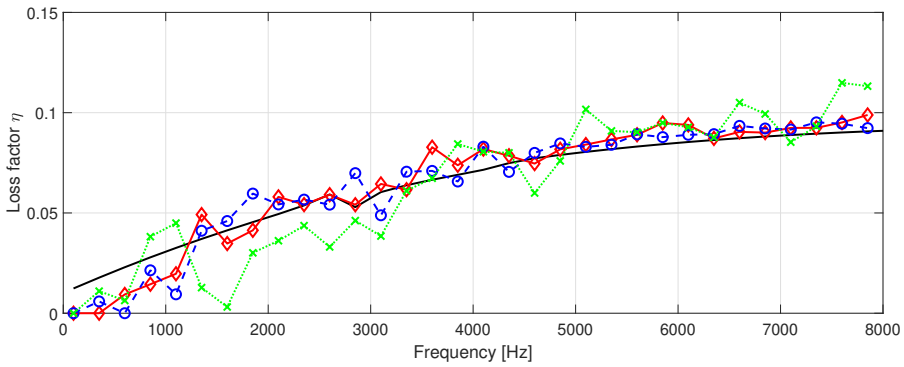

Figure III.29: Rectified average damping loss factor for the first and third excitation of the sandwich aluminium viscoelastic panel. —◇— $x_{0_1} = 0.2$ m and $y_{0_1} = 0.4$ m, — ○ — $x_{0_2} = 0.5$ m and $y_{0_2} = 0.6$ m, -×- $x_{0_2} = 0.8$ m and $y_{0_2} = 0.2$ m and - GLM.

III. 8 Excitation location: experimental validation

The effect of the excitation location is investigated experimentally on a sandwich carbon fiber honeycomb panel of dimensions 1 m × 1.5 m and total thickness of 27.3 mm. The experimental set up is described in details in Section III. 4. Three different excitation locations are marked with a red cross with their number in Fig. III.30.

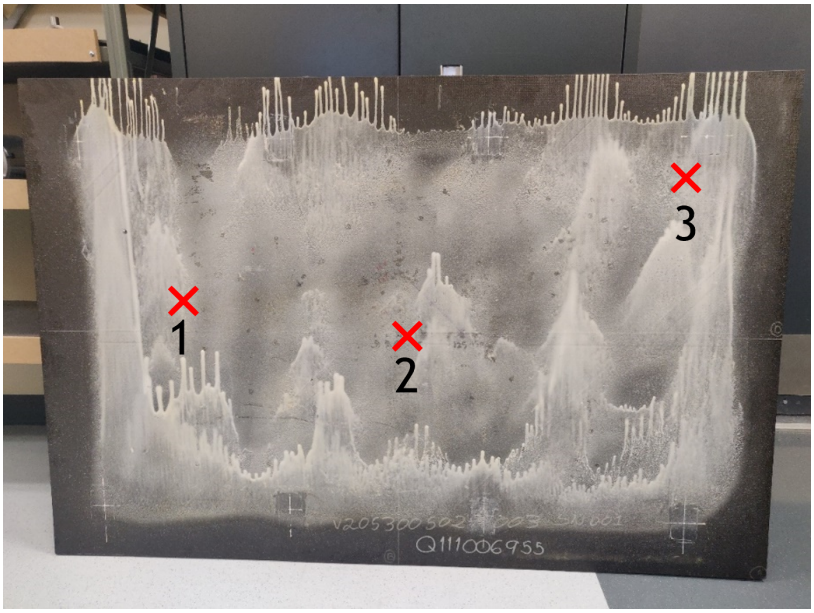

Figure III.30: Definition of the three excitation points of the sandwich carbon fiber honeycomb panel.

Results and discussion

The normal displacements $\mathbf{w}$ of the panel for each case at 3800 Hz are shown in Fig. III.31a-c respectively. For the first case, the excitation point is at $x_{0_1} = 0.28$ m and $y_{0_1} = 0.56$ m. For the second case, the excitation point is at $x_{0_2} = 0.77$ m and $y_{0_2} = 0.46$ m. For the third case, the excitation point is at $x_{0_3} = 1.17$ m and $y_{0_3} = 0.68$ m.

The Green's function-based model correlation(GFC) wavenumber maps for three excitation points at 3800 Hz are shown in Fig. III.32. The orthotropic behavior of the panel is visible for the second excitation where the panel is subject to a central excitation as shown in Fig. III.32b. For the first excitation, the maximum of the amplitude is less precise in the $-k_x$ area as shown in Fig. III.32a. For third excitation, the maximum of the amplitude is less precise from $-\pi$ to π as shown in Fig. III.32c. The discrepancies are due to the limitation of the panel length in these directions. Red lines and arrows in Fig. III.32a and Fig. III.32c define the applicable domain for the correction of the estimation of the damping loss factor.

Fig. III.33 and Fig. III.34 show the dispersion curves of the experimental sandwich carbon fiber at 0° and 90° respectively. In the high frequency range, a small divergence

between experimental results and the GLM is observed at 0°. This error maybe due to the uncertainty of the material properties defined in Table III.5.

For the dispersion curve at 0°, the estimation of the wavenumber for the first and second excitation show good correlation compared to the reference solution based on the general laminate model (GLM) above 1000 Hz. Below, the estimation is less accurate compared to the GLM due to the modal behavior of the panel. For the third excitation, the estimation of the wavenumber shows good correlation above 4000 Hz. Below 4000 Hz, the estimation is less accurate due to the limited measurement length of the panel in the 0° direction.

For the dispersion curve at 90°, the estimation of the wavenumber for the second case where the panel is subject to a central excitation is accurate compared to the GLM above 500 Hz. For the first and third excitation, the estimation below 3000 Hz shows discrepancies due to the limited measurement length of the panel in the 90° direction for both locations.

The estimation of the averaged damping loss factor using Eq. III.12 is shown in Fig. III.35. The result is compared to the reference experimental steady-state power input method expressed in a third octave frequency band and is averaged over three excitation points [21]. For the first excitation, the proposed method underestimates the damping loss factor below 2500 Hz. From 2500 Hz to 5000 Hz, the result is satisfactory compared to the power input method. Above 5000 Hz, the damping loss factor is overestimated.

For the second excitation where the panel is subject to a central excitation, a good agreement between the proposed method and the power input method is visible at high frequency above 1500 Hz. The discrepancies observed above 6000 Hz are certainly associated with the limitation of the mesh used to scan the displacement field. The wavenumber at 90° for 6000 Hz is approximately around 100 rad/m, considering a minimum of 4 elements per wavelength λ is required to estimate correctly the parameters [46], the minimum wavelength required is then $\lambda_{min} = 15$ mm. In this case, the mesh size described for the experimental validation (17 mm $\times$ 17 mm) is superior to the minimum wavelength required and explains the discrepancies observed above 6000 Hz.

For the third excitation, the proposed method shows discrepancies above 5000 Hz. The error is due to the erroneous value in some of the wave propagating angle. Between 1500 Hz and 5000 Hz, the result is satisfactory compared to the power input method.

Fig. III.36a-c shows the damping loss factor of the sandwich carbon fiber honeycomb panel as function of the frequency and the wave propagating angle from 0 to 2π. For the experimental case, the estimation of the damping loss factor as function of the wave propagating angle of the central excitation (see Fig. III.36b) is considered as reference. For the three cases, the damping loss factor below 500 Hz shows discrepancies. The error is associated to the modal behavior of the panel in the low frequency range. For the first excitation as shown in Fig. III.36a, the damping loss factor estimation is overestimated from $\frac{\pi}{2}$ to $\frac{3\pi}{2}$. For the third excitation as shown in Fig. III.36c, the discrepancies in estimating the damping loss factor are visible from 0 to π and from $\frac{3\pi}{2}$ to 2π. The discrepancies for both cases are associated to the limited length of the panel in these directions.

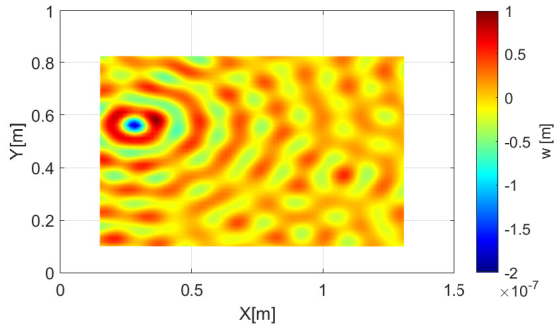

(a) First excitation point.

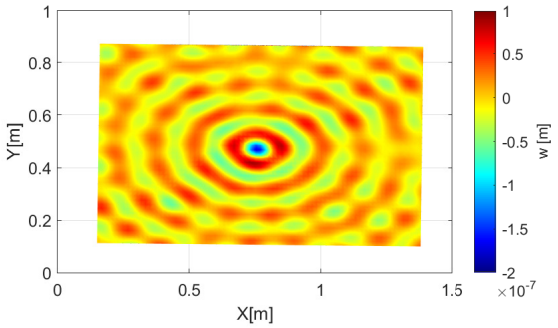

(b) Second excitation point.

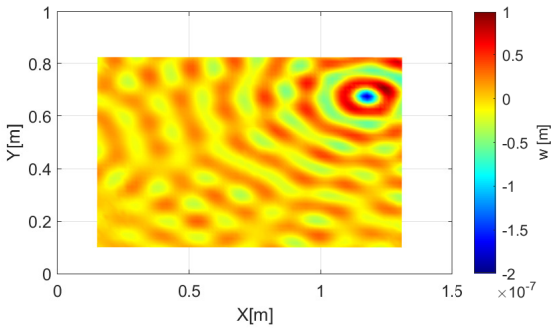

(c) Third excitation point.

Figure III.31: Measured normal displacements **w** of the sandwich carbon fiber honeycomb panel at 3800 Hz for three excitation points.

Correction of the estimation of the damping loss factor

Based on the damping loss factor as a function of frequency and the wave propagating angle maps shown in Fig. III.36, the rectification of the experimental result is applied. For each case, the domain of the angle used to calculate the average damping loss factor is defined in Table. III.7. The definition of the domain is made based on the precision of the GFC wavenumber maps (see Fig. III.32a and Fig. III.32c).

Case	Applicable domain θ
1	$\left[-\frac{\pi}{2};\frac{\pi}{2}\right]$
2	$[0;\ 2\pi]$
3	$[\pi;\ \frac{3\pi}{2}]$

Table III.7: Applicable domain in calculating the average damping loss factor.

The result of the rectified average damping loss factor is shown in Fig. III.37. The estimation of the damping loss factor for the first and third excitation show a better agreement globally compared to the previous estimation in Fig. III.35. For both first and second excitation, the results show a good correlation compared to the reference solution

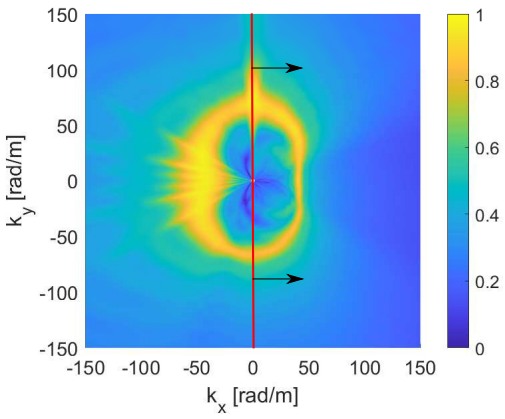

(a) First excitation point.

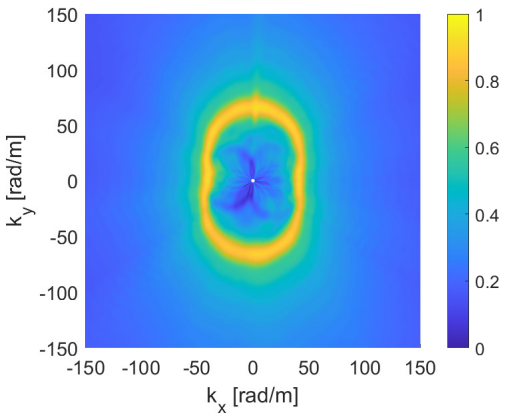

(b) Second excitation point.

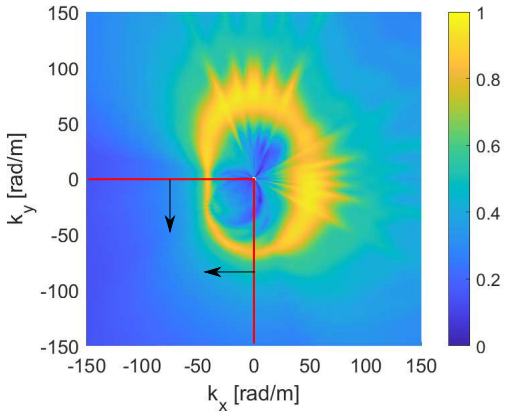

(c) Third excitation point.

Figure III.32: GFC wavenumber maps of the experimental sandwich carbon fiber honeycomb panel at 3800 Hz for three excitation points. Red lines and arrows define the applicable domain for the correction of the estimation of the damping loss factor.

based on the power input method.

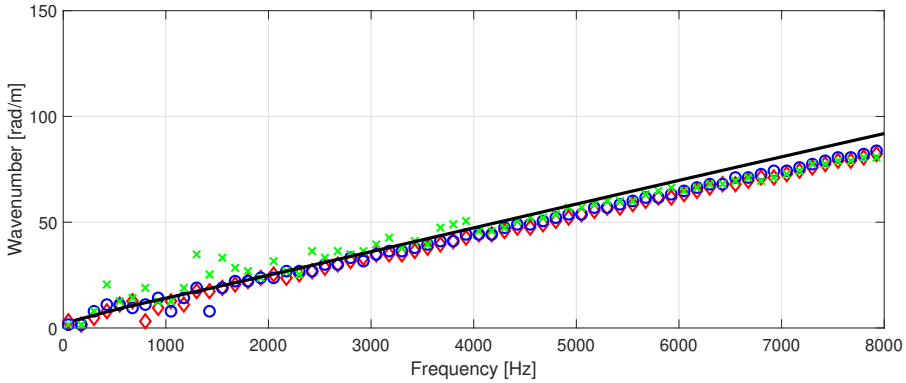

Figure III.33: Measured dispersion curves of the sandwich carbon fiber honeycomb panel at 0°. ◇ first excitation point, ○ second excitation point, × third excitation point and - GLM.

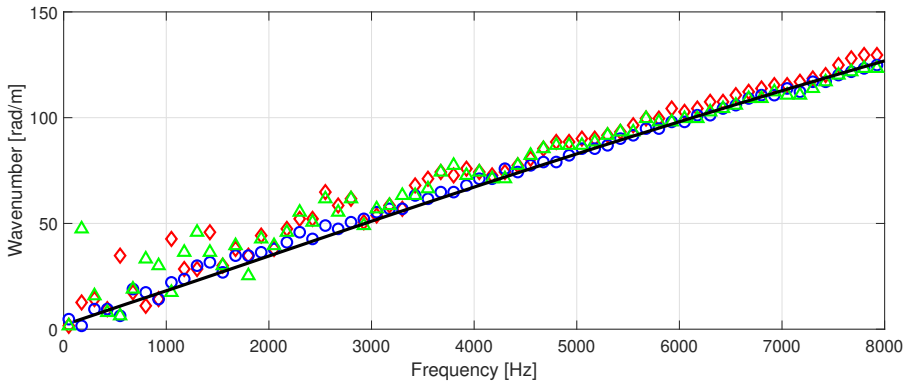

Figure III.34: Measured dispersion curves of the sandwich carbon fiber honeycomb panel at 90°. ◇ first excitation point, ○ second excitation point, × third excitation point and - GLM.

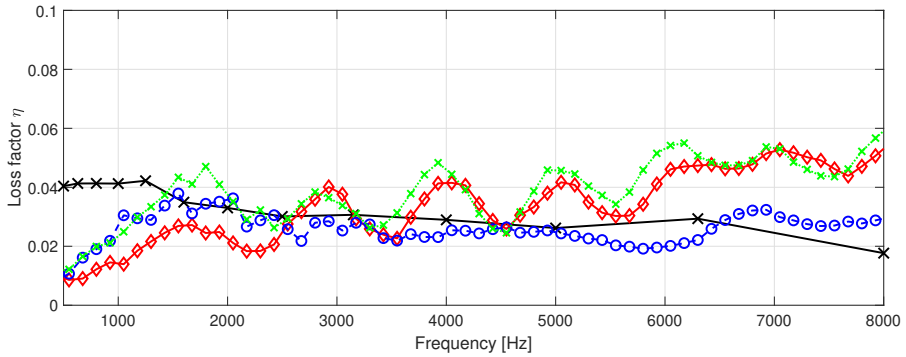

Figure III.35: Average damping loss factor of the experimental sandwich carbon fiber honeycomb panel. —◇— First excitation point, — ○ — Second excitation point, -x- Third excitation point and -×- Power input method.

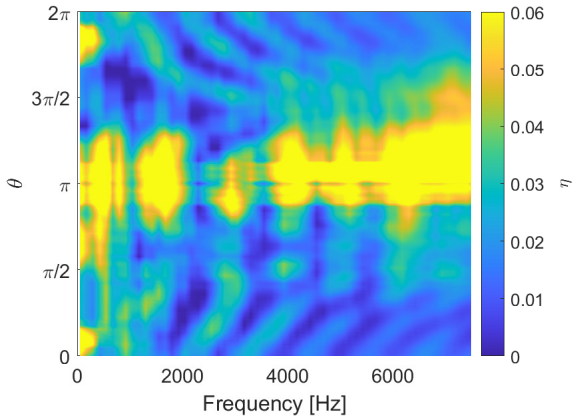

(a) First excitation point.

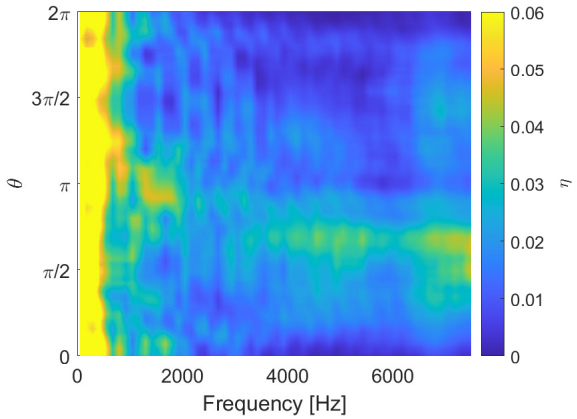

(b) Second excitation point.

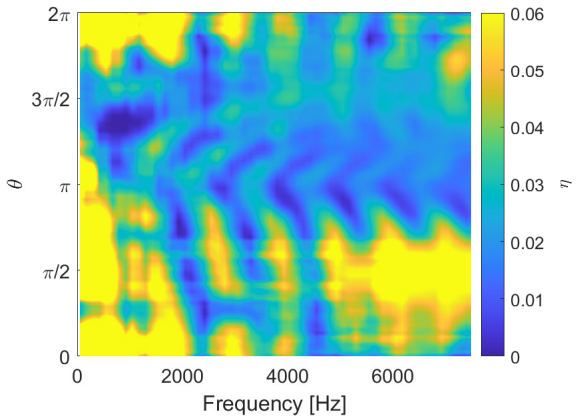

(c) Third excitation point.

Figure III.36: Damping loss factor η as function of the heading angle of the experimental sandwich carbon fiber honeycomb panel.

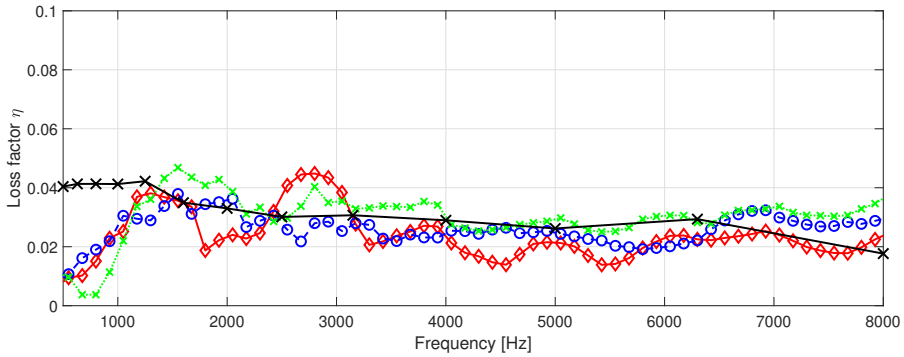

Figure III.37: Rectified average damping loss factor for the first and third excitation of the experimental sandwich carbon fiber honeycomb panel. —◇— First excitation point, —○— Second excitation point, -×- Third excitation point and -×- Power input method.

III.9 Conclusion of the chapter

A Green's function based-model correlation method able to estimate the damping loss factor as a function of the frequency and the heading angle is proposed in this chapter. In the first part, the proposed method estimates accurately the damping loss factor as a function of the frequency and the heading angle in the mid to high frequency range for highly damped structures. The effect of the orthotropy of the skin on the estimation of the damping loss factor is well demonstrated numerically and experimentally. However, the method is less accurate for lightly damped structures in the low frequency range, the image source method is proposed in Chapter IV to overcome this limitation.

In the second part, the performance of the method is observed on three different excitation locations: the first is near one of the boundaries, the second is the central excitation and the third is near the corner. The Green's function correlation method performs at best when the panel is subjected to a mechanical point load excitation at the center of the panel. In reality, a central excitation of the panel can sometimes be inaccessible and may not excite all modes. If the excitation point varies from the centre, the application of the method may cause discrepancies in some of the wave propagating angle and a rectification of the results is needed. A spatial angular filtering is introduced and improves the estimation of the damping loss factor. The efficiency of the filtering is demonstrated numerically and experimentally.

Chapter IV

Estimation of the damping loss factor in the low frequency range using the image source method

IV. 1 Introduction

In Chapter III, the Green's function-based model correlation (GFC) method was used to estimate accurately the damping loss factor of highly damped structures in the high frequency range. However, the GFC model considers only the direct field in the formulation which makes the estimation of the damping loss factor less accurate in the low frequency range and for lightly damped structures.

To take into account the reflection at boundaries, Gunda et al. [37] uses the combination of the image source method and the Hankel's functions to construct the Green's function of a finite plate with simply supported and roller supported boundary conditions. This method describes the field as a superposition of contributions from the original source and virtual sources located outside of the plate. Later, Gunda et al. [38] introduced the image source method for clamped and free edges, which is developed starting from either simply supported or roller supported solutions and applying corrections to account for boundary excitation.

Cuenca et al. [28] introduced analytical solutions of the reflection matrix on various boundary conditions such as clamped free edges for the first order image source model and introduced a high-frequency approximation method for the second and subsequent orders. Compared to the method of Gunda, the approach proposed by Cuenca is more general for arbitrary boundary conditions. Roozen et al. [75] applied the method experimentally to estimate the reflection coefficient, the wavenumber and the damping loss factor of a thin isotropic plate. The work of Roozen concentrated mainly on the development of the reflection coefficient as a function of the frequency. However, the accurate estimation of the damping loss factor in the low frequency range remains still an open issue.

This chapter investigates the performance of the combination of the image source model and the Green's function correlation (GFC-ISM) method for the estimation of the damping loss factor. The reflection coefficient of the image source model is determined with the theoretical definition introduced by Gunda [37] for a simply supported boundary conditions panel and Cuenca [28] for a free-free boundary conditions panel. The proposed method is compared to the previous GFC method [10] and to the analytical discrete general laminate model (GLM) [36] using numerical simulations. Based on the result, the approach improves tremendously the estimation of the damping loss factor in the low frequency range and for lightly damped structures.

In Section IV. 2, the image source method for simply supported panels is introduced. The application of the GFC-ISM on an isotropic steel panel with two different damping loss factor is investigated. In Section IV. 4, the image source method for free-free boundary conditions is introduced. The numerical validation on two different panels is descried: 1) a sandwich aluminium panel with a viscoelastic core and 2) a sandwich laminated glass panel with a frequency dependent PVB core.

IV. 2 Image source method for simply supported panels

The application of the image source method for simply supported panels is described in details in Section I. 6. 1. To recall, the harmonic Green's function of a rectangular plate with simply supported boundary conditions can be described as a linear combination of the original source and the image sources:

$$G_\Omega(\hat{k}, \mathbf{r}) = G_\infty(\hat{k}; \mathbf{r}, \mathbf{r_0}) + \sum_{i=1}^{N_v} \alpha(i) G_\infty(\hat{k}; \mathbf{r}, \mathbf{r_i}) \quad , \tag{IV.1}$$

where N_v is the number of image sources, $\mathbf{r_i}$ is the distance between the point of the panel and the image source and α is the source strength equaling +1 or -1 for a rectangular simply supported panel [37].

Using the idea described in Section III. 2. 2, the harmonic Green's function (see Eq. IV.1) is then correlated with the measured displacement field:

$$\mathrm{GFC}_{ISM}(\hat{k}, \mathbf{r}) = \frac{|\sum_{i=1}^{N} \hat{w}_i(\mathbf{r}) G_\Omega{}^*(\hat{k}, \mathbf{r}) \rho_i S_i|}{\sqrt{\sum_{i=1}^{N} |\hat{w}_i(\mathbf{r})|^2 \rho_i S_i \sum_{i=1}^{N} |G_\Omega(k, \mathbf{r})|^2 \rho_i S_i}} \quad , \tag{IV.2}$$

where $\hat{w}_i(r)$ represents the measured displacement field, * denotes the complex conjugate, ρ_i is a surface integration weight at point i, S_i is an estimation of the surface around the point i and N is the total number of acquisition points.

The identification of the complex wavenumber is obtained by maximizing the correlation function at each frequency. The complex wavenumber can also be defined as $\hat{k} = k(\omega)(1 + \mathrm{i}\gamma(\omega))$ where γ is the attenuation factor. The estimation is done in two steps. First, the algorithm estimates the real part of the wavenumber $k(\gamma)$ and then, the attenuation factor $\gamma(\omega)$ is quantified by using the same algorithm, just as in the previous GFC method.

IV.3 Damping loss factor estimation of a simply supported isotropic panel

An example of a simply supported steel panel excited with a point force is used for the demonstration of the approach (Length along x direction $L_x = 1$ m, length along y direction $L_y = 1.2$ m, density $\rho = 7800$ kg/m^3, Young's modulus E = 210 GPa, Poisson's coefficient ν= 0.33 and damping η=1%, 5%). The panel is subjected to a central excitation at $x_0 = 0.5$ m and $y_0 = 0.6$ m.

The solution of the equation of motion is solved analytically using the modal decomposition method. The equation writes (time-harmonic convention of $e^{-\mathrm{i}\omega t}$) [39]:

$$w(x,y,\omega) = \sum_{m=1}^{m}\sum_{n=1}^{n} \frac{\varphi_{mn}(x_0,y_0)\varphi_{mn}(x,y)}{\omega_{mn}^2 - \omega^2 + \mathrm{i}\eta\omega\omega_{mn}} \frac{4}{\rho h L_x L_y} \quad , \tag{IV.3}$$

where the mode shapes are written as:

$$\varphi_{mn}(x,y) = \sin(\frac{m\pi x}{L_x})\sin(\frac{n\pi y}{L_y}) \quad , \tag{IV.4}$$

and the eigen frequencies are defined by:

$$\omega_{mn} = \sqrt{\frac{D}{\rho h}}\left(\left(\frac{m\pi}{L_x}\right)^2 + \left(\frac{n\pi}{L_y}\right)^2\right) \quad , \tag{IV.5}$$

where D is the complex bending stiffness defined by $D = \frac{E(1-\mathrm{i}\eta)h^3}{12(1-\nu^2)}$.

The normal displacement of the panel for $\eta = 1\%$ at 1000 Hz is illustrated in Fig. IV.1a and simulated fields with different number of sources are shown in Figs. IV.1b-f. The comparison between the normal displacement $\mathbf{w}$ and the simulated vibrational field is quantified using the normalized reconstruction error [52, 75]:

$$e = \frac{||\mathbf{w} - \mathbf{G_\Omega}||^2}{||\mathbf{w}||^2} \quad . \tag{IV.6}$$

The error between the measured field and the simulated field with 1 source (equivalent to the Green's function of an infinite plate) is about 87.75%. As can be seen, the error decreases when the number of sources increases. For this case, the variation of the amplitude due to the constructive and destructive interferences of the direct waves and the reflected waves starts to be visible with 441 sources ($e = 14.39\%$) and the simulated field with 2601 sources ($e = 0.95\%$) is very similar to the normal displacement.

The normal displacement of the panel for $\eta = 5\%$ at 1000 Hz is illustrated in Fig. IV.2a and simulated fields with different number of sources are shown in Figs. IV.2b-f. The error decreases tremendously from $e = 60.55\%$ for 1 source to $e = 23.53\%$ for 9 sources. The simulated field depicts a very similar vibrational field behavior with only 121 sources ($e = 0.60\%$). For 441 and 2601 sources, the error is as small as $e = 0.063\%$ and $e = 0.039\%$ respectively. As expected, the number of sources needed to achieve the

convergence of result for higher damping structures is lower compared to low damping structures.

The normalized reconstruction error maps as a function of the frequency (10 to 1000 Hz) and the number of sources (1 to 2601 sources) for $\eta = 1\%$ and $\eta = 5\%$ are shown in Fig. IV.3a-b. For $\eta = 1\%$, the error in the very low frequency below 200 Hz is still very high even if the number of sources is large, as illustrated in Fig. IV.3a. The error remains high on the entire frequency range for the number of sources below 250. On the contrary for the case where the damping loss factor is at $\eta = 5\%$, a lower number of sources is needed for the error to be lower than 5% even in the very low frequency range as shown in Fig. IV.3b.

The estimation of the damping loss factor using different number of image sources is shown in Fig. IV.4 for $\eta = 1\%$ and in Fig. IV.5 for $\eta = 5\%$, respectively. For $\eta = 1\%$, the estimation of the damping loss factor with 1 source shows discrepancies on the entire frequency range due to the modal behavior of the panel which is ignored in the free field Green's function used in the proposed method. The result shows a very good correlation compared to the exact value with 2601 sources on the entire frequency range. For $\eta = 5\%$, the damping loss factor can already be predicted in the high frequency range with only 1 source. A good correlation in the low frequency range is depicted with 121, 441 and 2601 sources.

To conclude, the image source method increases the performance of the estimation of the damping loss factor in the low frequency range. For low damping structures, a very high number of sources is needed to obtain good results. In the high frequency range, a lower number of sources is sufficient to estimate correctly the damping loss factor. Based on the observation, a good estimation of the damping loss factor can be achieved with a correlation error between the simulated and reconstructed fields below 25%.

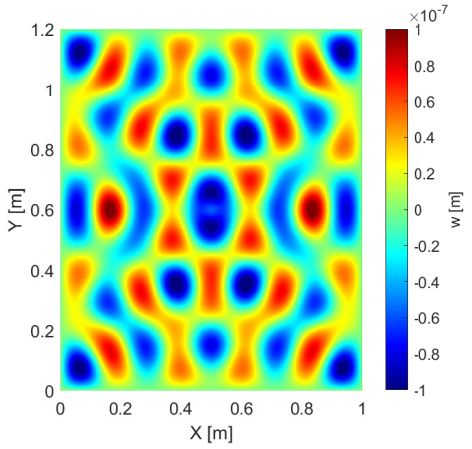

(a) Re{**w**}.

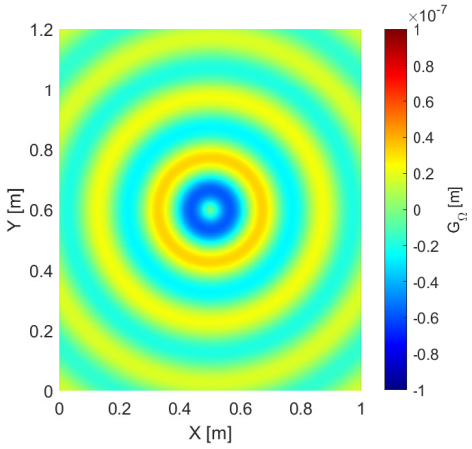

(b) 1 source ($e = 87.75\%$).

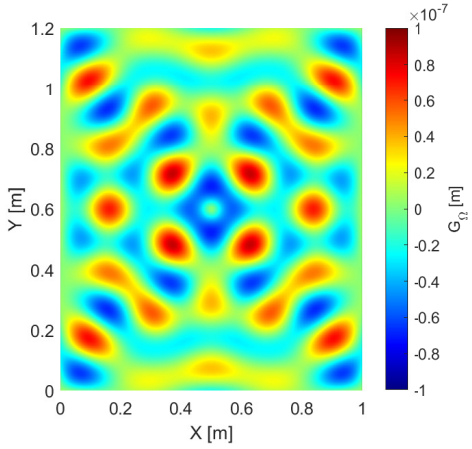

(c) 9 sources ($e = 73.25\%$).

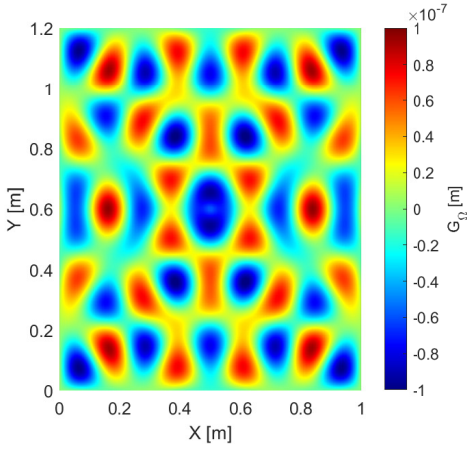

(d) 121 sources ($e = 34.45\%$).

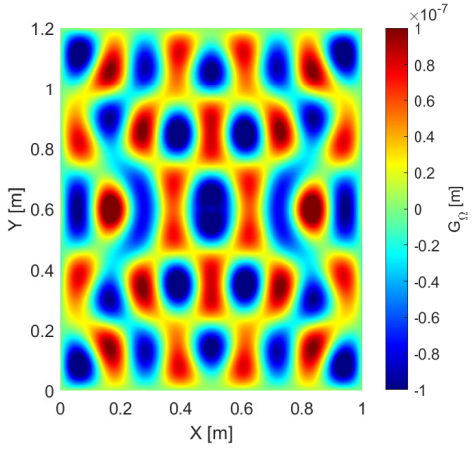

(e) 441 sources ($e = 14.39\%$).

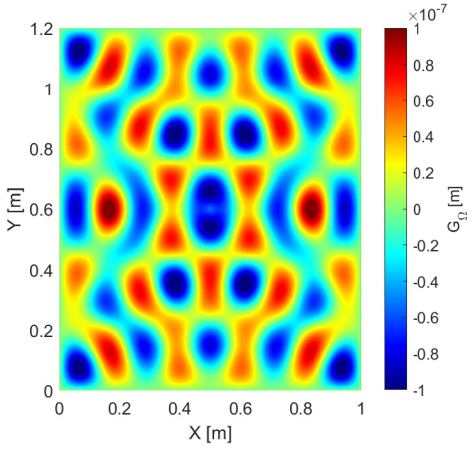

(f) 2601 sources ($e = 0.95\%$).

Figure IV.1: Real parts of the normal displacement obtained using Eq. IV.3 and image source models for $\eta = 1\%$ at 1000 Hz. The reference theoretical displacement is given in (a).

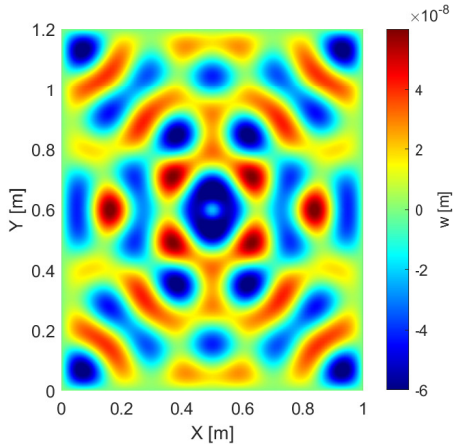

(a) Re{**w**}.

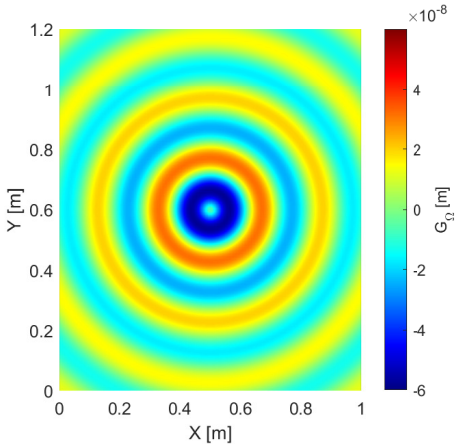

(b) 1 source ($e = 60.55\%$).

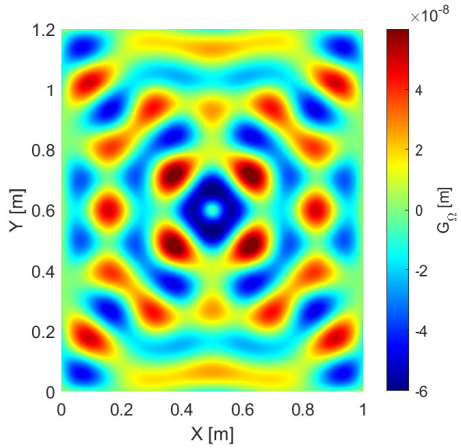

(c) 9 sources ($e = 23.53\%$).

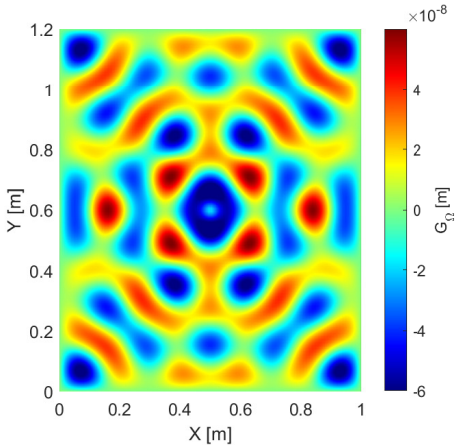

(d) 121 sources ($e = 0.60\%$).

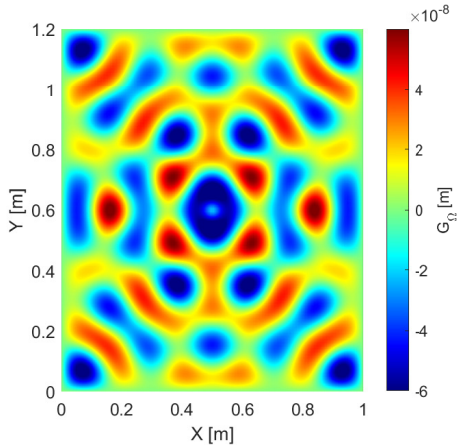

(e) 441 sources ($e = 0.063\%$).

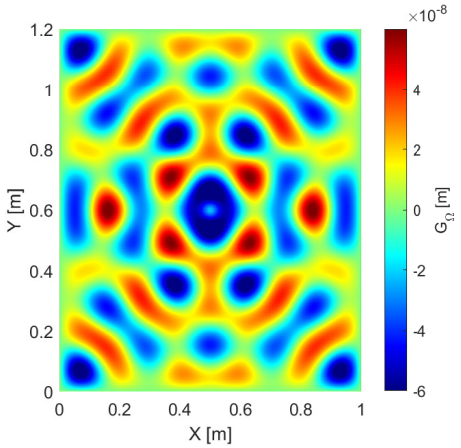

(f) 2601 sources ($e = 0.039\%$).

Figure IV.2: Real parts of the normal displacement obtained using Eq. IV.3 and image source models for $\eta = 5\%$ at 1000 Hz. The reference theoretical displacement is given in (a).

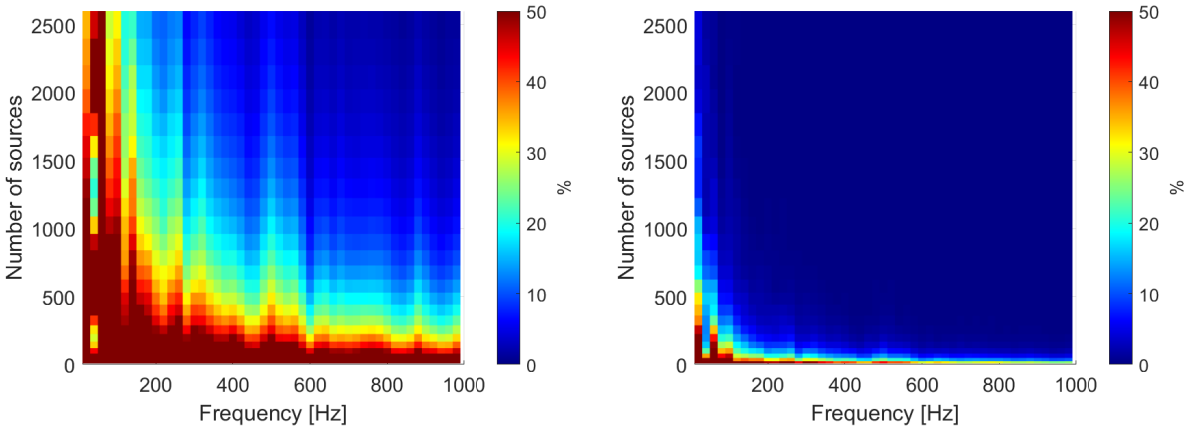

(a) $\eta = 1\%$. (b) $\eta = 5\%$.

Figure IV.3: Normalized reconstruction error maps between the measured displacement field and the simulated field of the panel as a function of frequency and the number of sources.

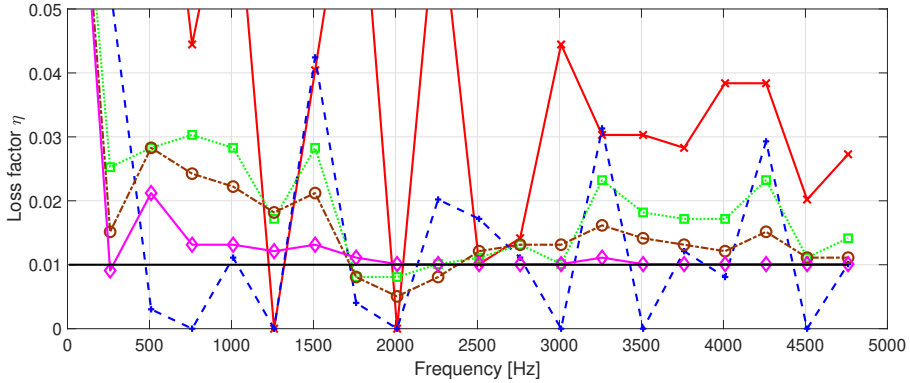

Figure IV.4: Estimation of the damping loss factor using different number of image sources of the steel panel with $\eta = 1\%$. - Exact, × 1 source, + 9 sources, □ 121 sources, ○ 441 sources and ◇ 2601 sources.

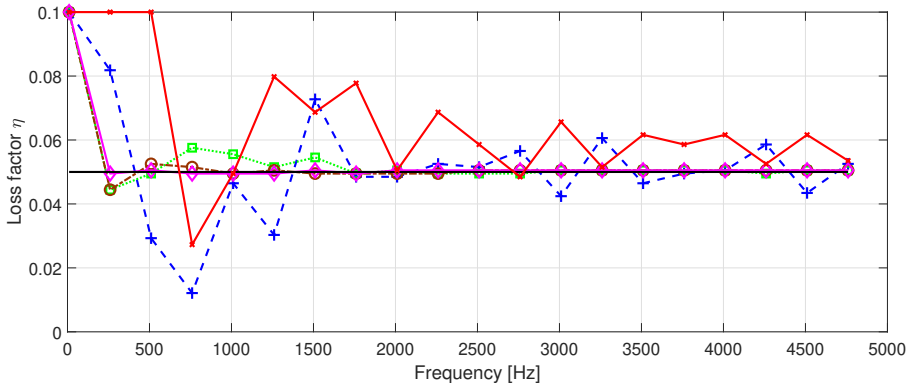

Figure IV.5: Estimation of the damping loss factor using different number of image sources of the steel panel with $\eta = 5\%$. - Exact, × 1 source, + 9 sources, □ 121 sources, ○ 441 sources and ◇ 2601 sources.

IV. 4 Image source method for free-free boundary conditions panels

In the previous section, the application of the image source method for a simply supported panel on the estimation of the damping loss factor is investigated and a good performance of the method is demonstrated. In reality, the experimental implementation of simply supported boundary conditions is quite difficult even if it is possible [74]. In most cases, experimental applications of wave fitting approaches use freely hanged structures.

For simply supported boundary conditions, the reflection coefficient or the source strength are directly ± 1. However, the reflection coefficient for free-free boundary conditions panel where the bending moment and the shear force are zeros is not so simple because the reflected wave has a local near field response which contains waves propagation along the edge of plate and evanescent waves in orthogonal directions [18].

The development of the image source method for free-free boundary conditions is described in Section I. 6. 2. The image sources of first order are developed analytically and an approximate method for calculating the contribution of image sources of second and higher orders was introduced by Cuenca in [28]. The method considers the wavelength as sufficiently short compared to plate dimensions and considers only propagating components of plane waves of Eq. I.67.

It is observed that the hypothesis made by Cuenca deteriorates the result in the low frequency range. The objective is to improve the estimation of the damping loss factor in the low frequency range where the wavelength can not be considered short. Still, in this section, only the first order image sources is used. The approximate method for second and subsequent orders is ignored.

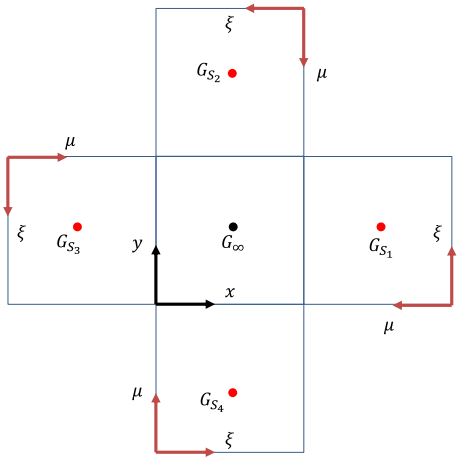

Figure IV.6: Image sources of a free-free boundary conditions panel.

Fig. IV.6 illustrates the reconstruction of the Green's function of an infinite plate G_∞ defined in global coordinates (x, y) and first order images sources G_s defined in local coordinates (ξ, μ). The harmonic Green's function of a rectangular plate with free edges is defined as:

$$G_\Omega(\hat{k};\mathbf{r},\mathbf{r_0}) = G_\infty(\hat{k};\mathbf{r},\mathbf{r_0}) + \sum_{i=1}^{4} G_{s_i}(\hat{k};\mathbf{r},\mathbf{r_{s_i}},\mu_{b_i}) \quad . \tag{IV.7}$$

Finally, the relation described in Eq. IV.7 is correlated with the measured displacement field using the correlation function defined in Eq. IV.2.

IV. 5 Damping loss factor estimation of isotropic sandwich panels with free-free boundary conditions

The method described in the previous section is now applied to two isotropic sandwich structures: the first is a sandwich aluminium panel with a viscoelastic core [10] and the second is a sandwich laminated glass panel with a frequency dependant PVB core [89].

The objective of the first simulations is to investigate the efficiency of the method on the estimation of the damping loss factor of a mid to high damped structure in the low frequency range and the objective of the second simulations is to investigate the efficiency of the method for a low damped structure.

IV. 5. 1 Isotropic aluminium sandwich with a viscoelastic core

The method is applied to a 1 m × 1.2 m sandwich aluminium panel with a viscoelastic core [63]. The skins are 2 mm thick aluminium (Density $\rho = 2700$ kg/m^3, Young's modulus E = 71 GPa, Poisson's coefficient $\nu = 0.33$ and damping η_{skin}=1%). The core is a 0.76 mm thick viscoelastic material (Density $\rho = 900$ kg/m^3, Young's modulus E = 1 GPa, Poisson's coefficient $\nu = 0.33$ and damping $\eta_{core} = 20\%$).

The normal displacement at 2100 Hz and 7600 Hz are shown in Fig. IV.7a and Fig. IV.7b respectively. Simulated fields with 1 source at 2100 Hz and 7600 Hz are shown in Fig. IV.7c and Fig. IV.7d, respectively. Simulated fields with 5 sources at 2100 Hz and 7600 Hz are shown in Fig. IV.7e and Fig. IV.7f.

At 2100 Hz, the error between the displacement field and the simulated field with 1 source is is 51.67% and is reduced to 47.25% with 5 sources. At 7600 Hz, the error between the displacement field and the simulated field with 1 source is 11.85% and the error between the measured displacement field and the simulated field with 5 sources is as low as 8.89%. The interference pattern between the direct and the reflected wave is visible in Fig. IV.7f.

The estimation of the average damping loss factor with the image source is shown in Fig. IV.8. In the high frequency range above 3000 Hz, both GFC and GFC-ISM methods with 5 sources show a very good correlation compared to the GLM in which a power balance equation is used to estimate the loss factor [36]. Between 500 Hz and 2000 Hz, the GFC-ISM method improves the estimation of the damping loss factor compared to the GFC method. Below 500 Hz, both GFC-ISM and GFC methods show discrepancies.

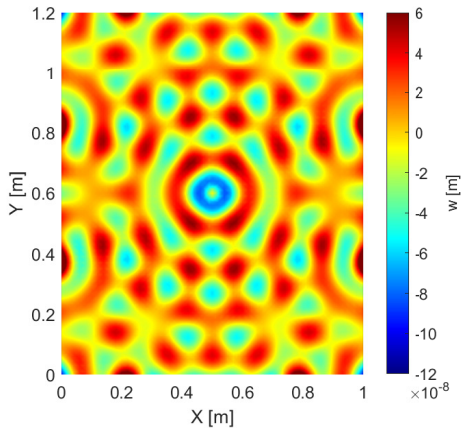

(a) Re{**w**} at 2100 Hz.

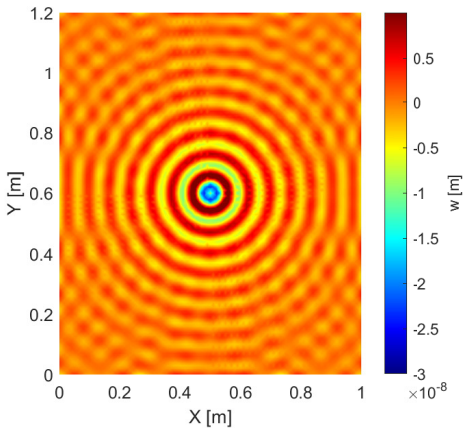

(b) Re{**w**} at 7600 Hz.

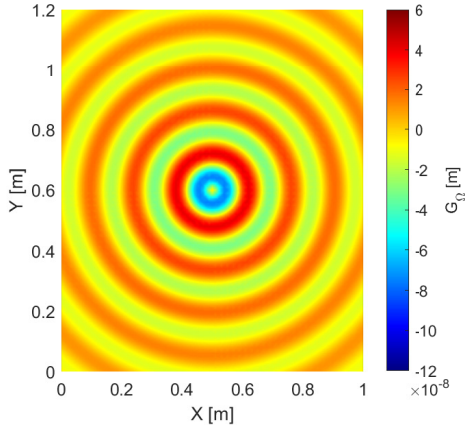

(c) 1 source at 2100 Hz ($e = 51.67\%$).

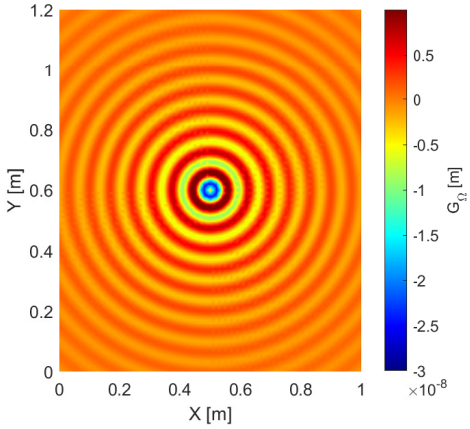

(d) 1 source at 7600 Hz ($e = 11.85\%$).

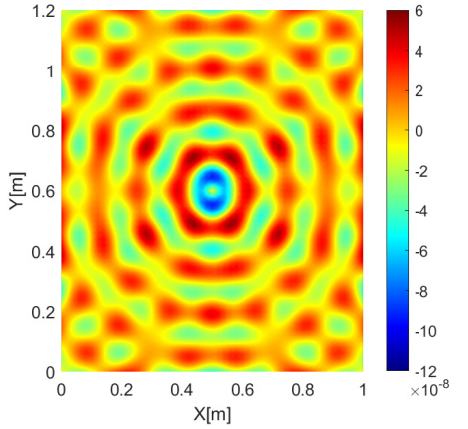

(e) 5 sources at 2100 Hz ($e = 47.25\%$).

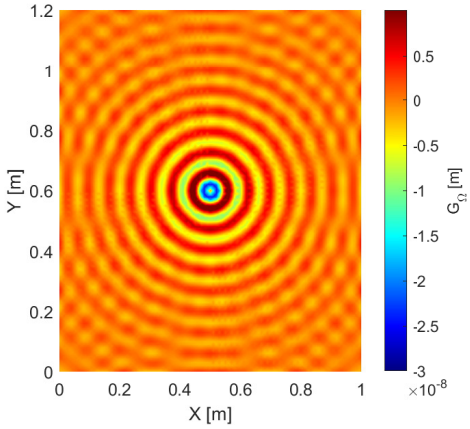

(f) 5 sources at 7600 Hz ($e = 8.89\%$).

Figure IV.7: Amplitude of the Green's function of the sandwich aluminium panel with a viscoelastic core. (a) - (b) Exact solution at 2100 Hz and 7600 Hz. (c) - (d) Green's function of an infinite plate at 2100 Hz and 7600 Hz. (e) - (f) Green's function of an infinite plate + 4 sources at 2100 Hz and 7600 Hz.

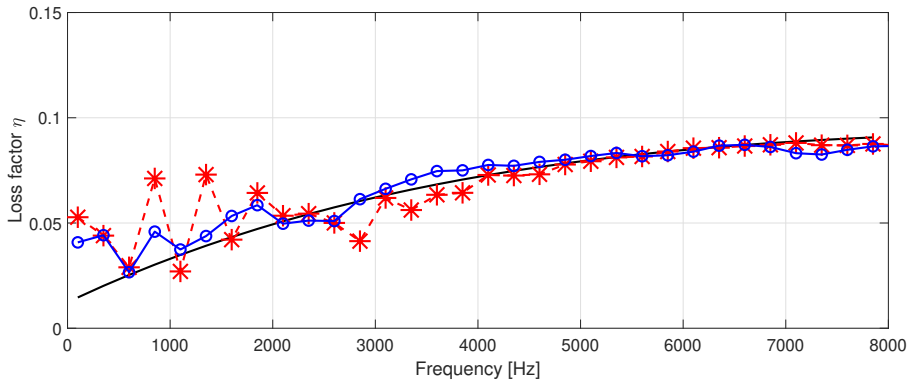

Figure IV.8: Comparison of the average damping loss factor of the sandwich aluminium panel with a viscoelastic core. - GLM, * 1 source and ⊖ 5 sources.

IV. 5. 2 Sandwich laminated glass panel with a frequency dependent PVB core

The method is then applied to a 1 m × 1.2 m sandwich laminated glass panel with a viscoelastic polyvinyl butyral (PVB) polymer core [89, 92]. The skins are 5 mm thick glass (Density $\rho = 2500$ kg/m^3, Young's modulus E = 71.04 GPa, Poisson's coefficient $\nu = 0.2$ and damping $\eta_{skin} = 0.1\%$). The PVB viscoelastic core material (Density ρ_{core}=1020 kg/m^3 , Poisson's coefficient $\nu_{core} = 0.449$) is 0.38 mm thick and has frequency dependant Young's modulus, shear modulus, and damping ratio defined in Table IV.1. The value of each parameter is interpolated for the simulations.

Frequency (Hz)	Shear Modulus (Pa)	Damping	Young's Modulus (Pa)
10	5.50E+07	0.46	1.65E+00
50	8.30E+07	0.27	2.49E+08
100	9.17E+07	0.24	2.75E+08
200	1.03E+08	0.21	3.08E+08
500	1.14E+08	0.15	3.42E+08
1000	1.21E+08	0.14	3.63E+08
2000	1.30E+08	0.12	3.90E+08
5000	1.38E+08	0.07	4.13E+08
10000	1.40E+08	0.04	4.19E+08
20000	1.41E+08	0.02	4.23E+08
30000	1.42E+08	0.02	4.24E+08

Table IV.1: The properties of the sandwich laminated glass core panel [89].

The normal displacement **w** at 1100 Hz and 7600 Hz are shown in Fig. IV.9a and Fig. IV.9b respectively. Simulated fields with 1 source at 1100 Hz and 7600 Hz are shown in Fig. IV.9c and Fig. IV.9d, respectively. Simulated fields with 5 sources at 1100 Hz and 7600 Hz are shown in Fig. IV.9e and Fig. IV.9f, respectively.

At 1100 Hz, the error between the displacement field and the simulated field with 1 source is about 74.41% and the error between the displacement field and the simulated field

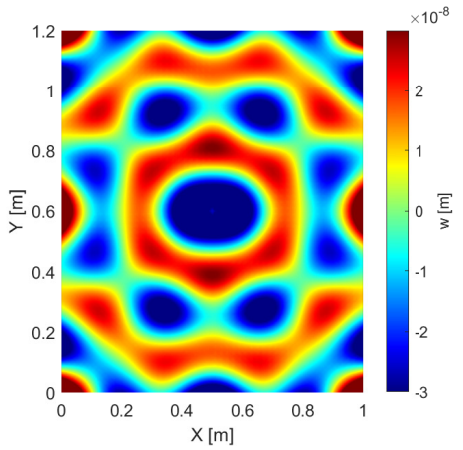

(a) Re{**w**} at 1100 Hz.

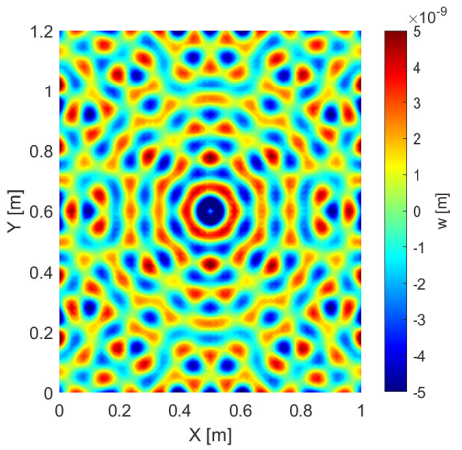

(b) Re{**w**} at 7600 Hz.

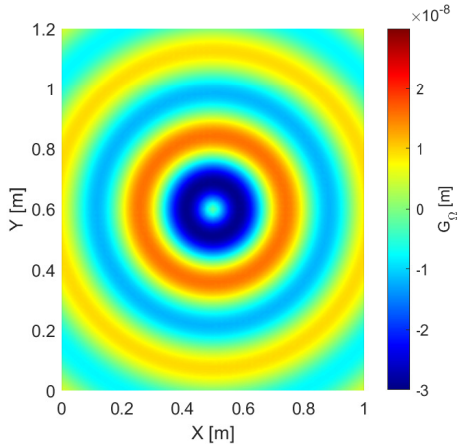

(c) 1 source at 1100 Hz ($e = 74.41\%$).

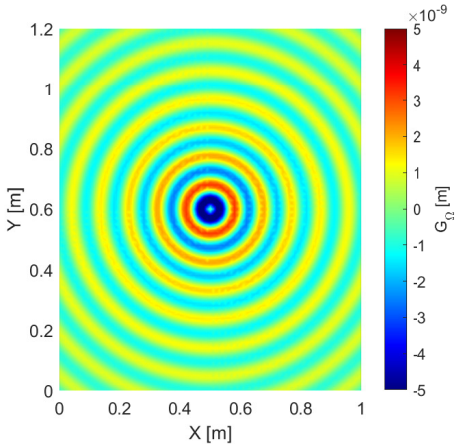

(d) 1 source at 7600 Hz ($e = 53.85\%$).

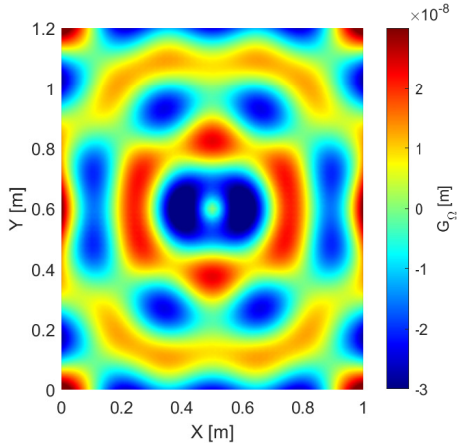

(e) 5 sources at 1100 Hz ($e = 58.82\%$).

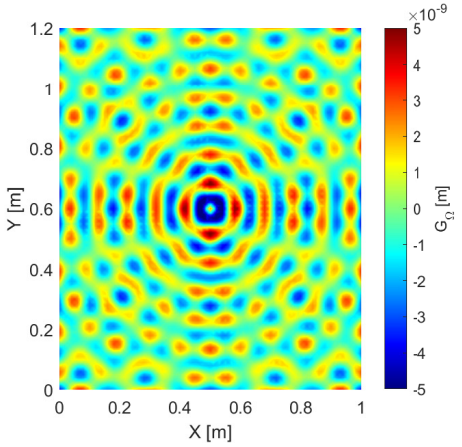

(f) 5 sources at 7600 Hz ($e = 42.03\%$).

Figure IV.9: Amplitude of the Green's function of the sandwich laminated glass with a frequency dependent PVB core panel. (a) - (b) Exact solution at 1100 Hz and 7600 Hz. (c) - (d) Green's function of an infinite plate at 2100 Hz and 7600 Hz. (e) - (f) Green's function of an infinite plate + 4 sources at 1100 Hz and 7600 Hz.

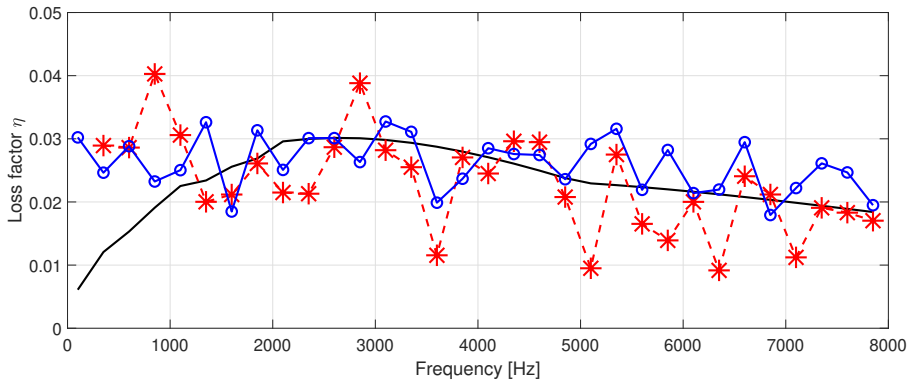

Figure IV.10: Comparison of the average damping loss factor of the sandwich laminated glass with a frequency dependent PVB core panel . - GLM, $*$ 1 source and $\ominus$ 5 sources.

with 5 sources is about 58.82%. As expected, the application of the image source method reduces the error between the measurement and the simulated vibrational field. Some parts of the variation of the amplitude due to the constructive and destructive interferences of the direct waves and the reflected waves is visible in Fig. IV.9e as compared to the normal displacement w in Fig. IV.9a. However, much more sources are needed to improve further the results.

At 7600 Hz, the error between the measured displacement field and the simulated field with 1 source is $e = 53.85\%$ and the error between the measured displacement field and the simulated field with 4 sources is $e = 42.03\%$. As can be seen, the application of the image sources reduces the error between the measurement and the simulated vibrational field.

The estimation of the average damping loss factor with the image sources is shown in Fig. IV.10. In the high frequency range above 2000 Hz, the ISM method shows a slightly better agreement with the GLM method [36] compared to the GFC method. Below 2000 Hz, the ISM method does not improve the estimation of the damping loss factor compared to the GFC method. The error is due to the limited number of image sources used for the correlation. A very high number of image sources is needed to estimate accurately the damping loss factor in the low frequency for low damping structures.

IV. 6 Conclusion of the chapter

A wave correlation GFC-ISM method has been proposed to estimate accurately the damping loss factor in the low frequency range and for lightly damped structures. The robustness of the method has been demonstrated numerically on isotropic structures with different boundary conditions by comparison with the previous GFC method and the analytical discrete general laminate model (GLM).

In general, a very high number of sources is needed for low damping structures as demonstrated for simply supported cases. For mid to high damped structures, a lower number of image sources is sufficient to predict accurately the damping loss factor. It is observed as well that even if the reduction in the correlation error between the simulated and reconstructed fields is not very significant, the improvement in the estimation of the damping is significant.

The efficiency of the method has also been demonstrated for panels with free edges. Despite the theoretical definition of the reflection coefficient being limited to first order only, the proposed method improves the estimation of the damping loss factor compared to the previous GFC method.

The efficiency of the present work on isotropic sandwich structures opens the possibility to apply this technique on non-isotropic structures by combining the angle-dependency Green's function described in Chapter III and the image source method.

General conclusion and perspectives

In the present work, inverse wave approaches have been adopted to estimate the complex wavenumber of flat thin and sandwich damped structures. The GFC method presented here is able to estimate accurately the damping loss factor as function of the frequency and the heading direction and overcomes limitations of previous methods.

An enhanced formulation of the inhomogeneous wave correlation (IWC) method has been introduced in the second chapter. This formulation takes into account the effects of the wave propagation around the excitation point by representing explicitly the associated exponential decay of the wave amplitude with distance from the source with the objective to improve the estimation of the damping loss factor. The proposed method has been applied to simple isotropic structures and complex anisotropic structures. The results have shown that the enhanced formulation improves slightly the estimation of the damping loss factor. Nevertheless, the robustness of the IWC method to estimate the damping loss factor in the presence of the excitation point remains questionable.

A Green's function-based model correlation (GFC) method able to estimate the damping loss factor as a function of the frequency and the heading angle has been introduced in the third chapter. This method eliminates the limitation of the free propagating plane wave hypothesis of the IWC method. Several results, with simulated and measured data, have been compared with an analytical discrete laminate model and have shown the accuracy of this Green's Function Correlation technique to recover the damping loss factor of complex structures with high damping and in the mid to high frequency range. An application of the method to an orthotropic structure has shown the effect of the orthotropy of the skin on the estimation of the damping loss factor. The proposed method is also able to estimate the damping loss factor of an anisotropic sandwich laminate panel accurately. The method has also been also investigated experimentally on a sandwich carbon fiber panel with a honeycomb core. The damping loss factor as a function of the frequency and the heading angle is well captured compared to classical methods such as the DRM and PIM.

The performance of the GFC method as a function of different point loads excitation has also been investigated in Chapter III. The proposed method performs at best when the panel is subjected to a mechanical point load excitation at the centre of the panel. If the excitation location varies from the centre, a correction factor is applied to estimate correctly the damping loss factor.

Finally, the classical image source method has been used in the GFC method (GFC-ISM) for two types of boundary conditions: simply supported and free edges. The former is useful for analytical validations and the latter is compatible with experimental tests. The method has been validated numerically using a steel panel with simply supported boundary conditions and two sandwich isotropic structures with free-free boundary conditions. The results have been compared to the previous GFC method. Based on the results, the application of the image source method improves the estimation of the damp-

ing loss factor. For low damping structures, a very high number of image sources is however needed to improve the estimation in the very low frequency range.

The presented work demonstrates the robustness of using correlation based methods to estimate the damping loss factor of planar complex structures. The perspective for future work would be the application of the image source method to non-isotropic structures with simply supported and free-free boundary conditions to improve the estimation of the damping loss factor as function of the angle of propagation in the low frequency range and for low damping structures. The development of the Green's function correlation method for curved structures to estimate the radial, axial, and azimuthal wavenumbers as well as the damping loss factor would be the second area of future work. Finally, an interesting case study would be the application of the Green's function to built-up structures such as stiffened and extruded panels.

Conclusion générale et perspectives

Dans cette thèse, la méthode de corrélation a été adoptée pour estimer le nombre d'onde complexe des structures minces ainsi que les structures en sandwich amorties. Le modèle présenté ici est capable d'estimer précisément l'amortissement en fonction de la fréquence et de la direction des propagations. Cette approche répond également aux limitations des méthodes précedentes.

Une variante de la méthode Inhomogeneous Wave Correlation (IWC) a été présentée dans le deuxième chapitre. Cette variante prend en compte la propagation de l'onde autour du point d'excitation en représentant explicitement la décroissance exponentielle de l'amplitude avec la distance à la source dans le but d'améliorer l'estimation de l'amortissement. Cette dernière a été appliquée aux structures isotropes ainsi qu'aux structures anisotropes laminées. La méthode présentée permet de prédire précisément le nombre d'onde en fonction de l'angle et améliore légèrement l'estimation de l'amortissement. Néanmoins, la robustesse de la méthode IWC pour estimer l'amortissement en présence du point d'excitation reste un point faible.

Une méthode de corrélation basée sur la fonction de Green (GFC) qui est capable d'estimer l'amortissement en fonction de l'angle et la direction de propagation est présentée dans le troisième chapitre. Cette méthode élimine la limitation de l'hypothèse d'onde plane à propagation libre de la méthode IWC. Plusieurs résultats, avec des données simulées et mesurées, sont comparés à un modèle analytique GLM et montrent la précision de cette technique de corrélation pour estimer l'amortissement des structures complexes en moyennes - hautes fréquences et des structures complexes fortement amorties. L'application de la méthode à une structure orthotrope montre bien l'effet de l'orthotropie de la peau sur l'estimation de l'amortissement. La méthode proposée est également capable d'estimer précisément l'amortissement d'une structure sandwich stratifiée. La méthode est également étudiée expérimentalement sur un panneau sandwich en fibre de carbone avec une âme en nid d'abeille. L'amortissement en fonction de la fréquence et de la direction des propagations est bien identifié par rapport aux méthodes classiques telles que le DRM et le PIM.

La performance de la méthode GFC en fonction des différents points d'excitation est également étudiée en complément dans ce chapitre. De manière générale, la méthode proposée fonctionne au mieux lorsque le panneau est soumis à une excitation ponctuelle en son centre. Si l'excitation n'est pas au centre, un filtre angulaire spatial est introduit pour rectifier le resultat.

Enfin, la méthode classique des sources images dans la méthode GFC (GFC-ISM) pour deux types de conditions aux limites : bords simplement appuyés et bords libres a été introduite. Le premier est utile pour les validations analytiques et le second est compatible avec les tests expérimentaux. La méthode a été validée numériquement en utilisant un panneau en acier avec des conditions aux limites simplement appuyées et deux structures sandwich isotropes avec des conditions aux limites libre-libre. Les résultats ont

été comparés à la méthode GFC précédente. Les résultats montrent que l'application de la méthode des sources images améliore l'estimation de l'amortissement. Pour les structures faiblement amorties, un très grand nombre de sources images est cependant nécessaire pour améliorer l'estimation de l'amortissement en très basses fréquences.

Le travail présenté démontre la robustesse pour estimer l'amortissement des structures planes complexes en utilisant la méthode de corrélation. La première perspective des futurs travaux serait l'application de la méthode des sources images à des structures non-isotropes avec des conditions aux limites simplement supportées et libres pour améliorer l'estimation de l'amortissement en fonction l'angle de propagation des ondes en basses fréquences et pour les structures faiblement amorties. Le développement de la méthode de corrélation de la fonction de Green pour les structures courbes afin d'estimer les nombres d'onde radial, axial et azimutal ainsi que le facteur de perte d'amortissement serait la deuxième perspective des futurs travaux. Enfin, l'application de la fonction de Green à des structures raidies et extrudées constituerait des cas d'études très intéressants et enrichissants.

List of Figures

List of Tables

Bibliography

[1] F. Ablitzer, C. Pézerat, J. M. Génevaux, and J. Bégué. Identification of stiffness and damping properties of plates by using the local equation of motion. *Journal of Sound and Vibration*, 333(9):2454–2468, 2014.

[2] F. Ablitzer, C. Pézerat, B. Lascoup, and J. Brocail. Identification of the flexural stiffness parameters of an orthotropic plate from the local dynamic equilibrium without a priori knowledge of the principal directions. *Journal of Sound and Vibration*, 2017.

[3] J. Antoni. A Bayesian approach to sound source reconstruction: Optimal basis, regularization, and focusing. *The Journal of the Acoustical Society of America*, 131(4):2873–2890, 2012.

[4] N. Atalla and F. Sgard. *Finite Element and Boundary Methods in Structural Acoustics and Vibration*. CRC Press, 2015.

[5] A. Berry, O. Robin, and F. Pierron. Identification of dynamic loading on a bending plate using the virtual fields method. *Journal of Sound and Vibration*, 333(26):7151–7164, 2014.

[6] J. Berthaut. *Contribution à l'identification large bande des structures anisotropes : Application aux tables d'harmonie des pianos*. PhD thesis, Ecole Centrale Lyon, 2004.

[7] J. Berthaut, M. N. Ichchou, and L. Jezequel. K-space identification of apparent structural behaviour. *Journal of Sound and Vibration*, 280(3-5):1125–1131, 2005.

[8] A. Berthet, E. Perrey-Debain, and J.-D. Chazot. The balanced proper orthogonal decomposition applied to a class of frequency-dependent damped structures. *Mechanical Systems and Signal Processing*, 185(August 2022):109746, 2023.

[9] D. A. Bies and S. Hamid. In situ determination of loss and coupling loss factors by the power injection method. *Journal of Sound and Vibration*, 70(2):187–204, 1980.

[10] M. N. Bin Fazail, J.-D. Chazot, G. Lefebvre, and N. Atalla. Identifcation of the dispersion curves and the damping loss factor using green's function-based model of non-isotropic structures. *Proceedings of the 28th International Congress on Sound and Vibration, Singapore*, pages 1–8, 2022.

[11] B. Bloss and M. D. Rao. Measurement of damping in structures by the power input method. *Experimental Techniques*, 26(3):30–32, 2002.

[12] M. Bolduc. *Acquiring statistical energy analysis damping loss factor for complex structures with low to high damping characteristics*. PhD thesis, Université de Sherbrooke, 2007.

[13] M. Bolduc and N. Atalla. Measurement of sea damping loss factor for complex structures. *The Journal of the Acoustical Society of America*, 123(5):3060–3060, 2008.

[14] P. Butaud. *Contribution à l'utilisation des polymères à mémoire de forme pour les structures à amortissement contrôlé*. PhD thesis, Université de Franche-Comté, France, 2015.

[15] P. Butaud, E. Foltête, and M. Ouisse. Sandwich structures with tunable damping properties: On the use of Shape Memory Polymer as viscoelastic core. *Composite Structures*, 153:401–408, 2016.

[16] J.-D. Chazot, B. Nennig, and A. Chettah. Harmonic response computation of viscoelastic multilayered structures using a zpst shell element. *Computers & Structures*, 89:2522–2530, 12 2011.

[17] J.-D. Chazot, B. Nennig, and E. Perrey-Debain. Harmonic response computation of poroelastic multilayered structures using ZPST shell elements. *Computers and Structures*, 121:99–107, 2013.

[18] G. Chen, P. C. Matthew, and J. Zhou. Analysis of vibration eigen frequencies of a thin plate by the keller-rubinow wave method i: Clamped boundary conditions with rectangular or circular geometry. *SIAM Journal on Applied Mathematics*, 51(4):967–983, 1991.

[19] R. Cherif. *Caractérisation expérimentale et numérique de la transmission acoustique de structures aéronautiqe effets du couplage et de léxcitation*. PhD thesis, Université de Sherbrooke, 2015.

[20] R. Cherif and N. Atalla. Experimental investigation of the accuracy of a vibroacoustic model for sandwich-composite panels. *The Journal of the Acoustical Society of America*, 137(3):1541–1550, 2015.

[21] R. Cherif, J.-D. Chazot, and N. Atalla. Damping loss factor estimation of two-dimensional orthotropic structures from a displacement field measurement. *Journal of Sound and Vibration*, 356:61–71, 2015.

[22] R. Cherif, A. Wareing, and N. Atalla. Evaluation of a hybrid TMM-SEA method for prediction of sound transmission loss through mechanically coupled aircraft double-walls. *Applied Acoustics*, 117:132–140, 2017.

[23] S. H. Crandall. The role of damping in vibration theory. *Journal of Sound and Vibration*, 11(1):3–IN1, 1970.

[24] L. Cremer, M. Heckl, and B.A.T. Petersson. *Structure-Borne Sound*. Springer Berlin Heidelberg, 1973.

[25] J. Cuenca. *Wave models for the flexural vibrations of thin plates - Model of the vibrations of polygonal plates by the image source method - Vibration damping using the acoustic black hole effect*. PhD thesis, Université du Maine, 2009.

[26] J. Cuenca, F. Gautier, and L. Simon. Measurement of the complex bending stiffness of a flat panel covered with a viscoelastic layer using the image source method. *8th European Conference on Noise Control 2009, EURONOISE 2009 - Proceedings of the Institute of Acoustics*, 31(PART 3), 2009.

[27] J. Cuenca, F. Gautier, and L. Simon. The image source method for calculating the vibrations of simply supported convex polygonal plates. *Journal of Sound and Vibration*, 322(4-5):1048–1069, 2009.

[28] J. Cuenca, F. Gautier, and L. Simon. Harmonic Green's functions for flexural waves in semi-infinite plates with arbitrary boundary conditions and high-frequency approximation for convex polygonal plates. *Journal of Sound and Vibration*, 331(6):1426–1440, 2012.

[29] W. d. S. Clarence. *Vibration Fundamentals and Practice*. CRC Press LLC, Boca Raton, FL, USA, 1999.

[30] K. Ege, N. B. Roozen, Q. Leclère, and R. G. Rinaldi. Assessment of the apparent bending stiffness and damping of multilayer plates; modelling and experiment. *Journal of Sound and Vibration*, 426:129–149, 2018.

[31] T. Égreateau. Développement numérique et implémentation expérimentale d'une méthodologie d'identification de l'équation de dispersion dans les structures aéronautiques. Mémoire de maitrise, Université de Sherbrooke, Sherbrooke, Québec, Canada, 2011.

[32] Z. Fang and L. Zheng. Topology optimization for minimizing the resonant response of plates with constrained layer damping treatment. *Shock and Vibration*, 2015, 2015.

[33] N. Ferguson, C.R. Halkyard, Brian Mace, and K.H. Heron. The estimation of wavenumbers in two-dimensional structures. *Proceedings of the 2002 International Conference on Noise and Vibration Engineering, ISMA*, pages 799–806, 01 2002.

[34] G. Y. Gao, Jian Song, and Jun Yang. Identifying boundary between near field and far field in ground vibration caused by surface loading. *Journal of Central South University*, 21(8):3284–3294, 2014.

[35] E. J. Garesser and C. R. Wong. The relationship of traditional damping measures for materials with high damping capacity: a review. *M3D: Mechanics and Mechanisms of Material Damping, ASTM STP 1169*, pages 316– 343, 1992.

[36] S. Ghinet and N. Atalla. Modeling thick composite laminate and sandwich structures with linear viscoelastic damping. *Computers & Structures*, 89(15-16):1547–1561, 2011.

[37] R. Gunda, S. M. Vijayakar, and R. Singh. Method of images for the harmonic response of beams and rectangular plates. *Journal of Sound and Vibration*, 185(5):791–808, 1995.

[38] R. Gunda, S. M. Vijayakar, R. Singh, and J. E. Farstad. Harmonic Green's functions of a semi-infinite plate with clamped or free edges. *The Journal of the Acoustical Society of America*, 103(2):888–899, 1998.

[39] J.-L. Guyader. *Vibrations des milieux continus*. Hermès sciences publications, Paris, France, 2002.

[40] S. A. Hambric and A. R. Barnard. Tutorial on wavenumber transforms of structural vibration fields. *INTER-NOISE 2018 - 47th International Congress and Exposition on Noise Control Engineering: Impact of Noise Control Engineering*, 2018.

[41] M. N. Ichchou, O. Bareille, and J. Berthaut. Identification of effective sandwich structural properties via an inverse wave approach. *Engineering Structures*, 30(10):2591–2604, 2008.

[42] M. N. Ichchou, J. Berthaut, and M. Collet. Multi-mode wave propagation in ribbed plates: Part I, wavenumber-space characteristics. *International Journal of Solids and Structures*, 45(5):1179–1195, 2008.

[43] M. N. Ichchou, J. Berthaut, and M. Collet. Multi-mode wave propagation in ribbed plates. Part II: Predictions and comparisons. *International Journal of Solids and Structures*, 45(5):1196–1216, 2008.

[44] B.S. Kukreja and J. Löfström. Composites in the aircraft industry. https://www.appropedia.org/Composites_in_the_Aircraft_Industry, August 2022.

[45] R. Lajili, O. Bareille, M. L. Bouazizi, M. Ichchou, and N. Bouhaddi. Composite beam identification using a variant of the inhomogeneous wave correlation method in presence of uncertainties. *Engineering Computations*, 35(6):2126–2164, 2018.

[46] P. Langer, M. Maeder, C. Guist, M. Krause, and S. Marburg. More Than Six Elements per Wavelength: The Practical Use of Structural Finite Element Models and Their Accuracy in Comparison with Experimental Results. *Journal of Computational Acoustics*, 25(4), 2017.

[47] A. Le Bot. *Foundation of Statistical Energy Analysis in Vibroacoustics*. Oxford University Press, 05 2015.

[48] Q. Leclère, F. Ablitzer, and C. Pézerat. Practical implementation of the corrected force analysis technique to identify the structural parameter and load distributions. *Journal of Sound and Vibration*, 2015.

[49] Q. Leclère and C. Pézerat. Vibration source identification using corrected finite difference schemes. *Journal of Sound and Vibration*, 2012.

[50] G Lefebvre, X Boutillon, and M Filoche. Spatial spectra of the eigenmodes of ribbed plates projected on dispersion branches. *MEDYNA 2017: 2nd Euro-Mediterranean Conference on Structural Dynamics and Vibroacoustics*, pages 1–6, 2017.

[51] L. Lei, J.-D. Chazot, and N. Dauchez. Inverse method for elastic properties estimation of a poroelastic material within a multilayered structure. *Applied Acoustics*, 148:133–140, 2019.

[52] S.X. Liao and M. Pawlak. On the accuracy of zernike moments for image analysis. *IEEE Transactions on Pattern Analysis and Machine Intelligence*, 20(12):1358–1364, 1998.

[53] R. H. Lyon and R. G. DeJong. *Theory and Application of Statistical Energy Analysis*. Elsevier Inc., Englewood Cliffs, NJ, USA, 1994.

[54] E. Manconi and B. R. Mace. Estimation of the loss factor of viscoelastic laminated panels from finite element analysis. *Journal of Sound and Vibration*, 329(19):3928–3939, 2010.

[55] F. Marchetti. *Modélisation et caractérisation large bande de plaques multicouches anisotropes*. PhD thesis, Institut National des Sciences Appliquées de Lyon, 2019.

[56] F. Marchetti, K. Ege, Q. Leclère, and N. B. Roozen. On the structural dynamics of laminated composite plates and sandwich structures; a new perspective on damping identification. *Journal of Sound and Vibration*, 474, 2020.

[57] F. Marchetti, N. B. Roozen, J. Segers, K. Ege, M. Kersemans, and Q. Leclère. Experimental methodology to assess the dynamic equivalent stiffness properties of elliptical orthotropic plates. *Journal of Sound and Vibration*, 495:115897, 2021.

[58] Fabien Marchetti, Kerem Ege, and Quentin Leclère. Development of the corrected force analysis technique for laminated composite panels. *Journal of Sound and Vibration*, 490:115692, 2021.

[59] P. Margerit, A. Lebée, J. F. Caron, and X. Boutillon. High Resolution Wavenumber Analysis (HRWA) for the mechanical characterisation of viscoelastic beams. *Journal of Sound and Vibration*, 433:198–211, 2018.

[60] P. Margerit, A. Lebée, J. F. Caron, K. Ege, and X. Boutillon. The High-Resolution Wavevector Analysis for the characterization of the dynamic response of composite plates. *Journal of Sound and Vibration*, 458:177–196, 2019.

[61] J. G. McDaniel, P. Dupont, and L. Salvino. A wave approach to estimating frequency-dependent damping under transient loading. *Journal of Sound and Vibration*, 231(2):433–449, 2000.

[62] J. G. McDaniel and W. S. Shepard. Estimation of structural wave numbers from spatially sparse response measurements. *The Journal of the Acoustical Society of America*, 108(4):1674–1682, 2000.

[63] D. J. McTavish and P. C. Hughes. Modeling of linear viscoelastic space structures. *Journal of Vibration and Acoustics, Transactions of the ASME*, 115(1):103–110, 1993.

[64] K. Mekki, W. Derigent, E. Rondeau, and A. Thomas. Wireless sensors networks as black-box recorder for fast flight data recovery during aircraft crash investigation. *IFAC-PapersOnLine*, 50:814–819, 07 2017.

[65] A. C. Nilsson. Wave propagation in and sound transmission through sandwich plates. *Journal of Sound and Vibration*, 138(1):73–94, 1990.

[66] E. Nilsson and A. C. Nilsson. Prediction and measurement of some dynamic properties of sandwich structures with honeycomb and foam cores. *Journal of Sound and Vibration*, 251(3):409–430, 2002.

[67] G. A. Papagiannopoulos and G. D. Hatzigeorgiou. On the use of the half-power bandwidth method to estimate damping in building structures. *Soil Dynamics and Earthquake Engineering*, 31(7):1075–1079, 2011.

[68] A. Pereira, J. Antoni, and Q. Leclère. Empirical Bayesian regularization of the inverse acoustic problem. *Applied Acoustics*, 97:11–29, 2015.

[69] M. Petyt. *Introduction to Finite Element Vibration Analysis*. Cambridge University Press, Cambridge, 1990.

[70] C. Pézerat, Q. Leclère, N. Totaro, and M. Pachebat. Identification of vibration excitations from acoustic measurements using near field acoustic holography and the force analysis technique. *Journal of Sound and Vibration*, 326(3-5):540–556, 2009.

[71] C. Pézerat and J. L. Guyader. Two inverse methods for localization of external sources exciting a beam. *Acta acustica*, 3(1):1–10, 1995.

[72] C. Pézerat and J. L. Guyader. Identification of vibration sources. *Applied Acoustics*, 61(3):309–324, 2000.

[73] M. Rak, M. Ichchou, and J. Holnicki-Szulc. Identification of structural loss factor from spatially distributed measurements on beams with viscoelastic layer. *Journal of Sound and Vibration*, 310(4-5):801–811, 2008.

[74] O. Robin, J.-D. Chazot, R. Boulandet, M. Michau, A. Berry, and N. Atalla. A plane and thin panel with representative simply supported boundary conditions for laboratory vibroacoustic tests. *Acta Acustica united with Acustica*, 102(1):170–182, 2016.

[75] N. B. Roozen, Q. Leclère, K. Ege, and Y. Gerges. Estimation of plate material properties by means of a complex wavenumber fit using Hankel's functions and the image source method. *Journal of Sound and Vibration*, 390:257–271, 2017.

[76] J. Sanchez and H. Benaroya. Review of force reconstruction techniques. *Journal of Sound and Vibration*, 333(14):2999–3018, 2014.

[77] P. J. Shorter. Wave propagation and damping in linear viscoelastic laminates. *The Journal of the Acoustical Society of America*, 115(5):1917–1925, 2004.

[78] Siemens. How to calculate damping from a frf? https://community.sw.siemens.com/s/article/how-to-calculate-damping-from-a-frf, 2020.

[79] W. Soedel. *Vibration of Shells and Plates*. Marcel Dekker, New York, USA, 2004.

[80] M. Sulmoni, T. Gmür, J. Cugnoni, and M. Matter. Modal validation of sandwich shell finite elements based on ap-order shear deformation theory including zigzag terms. *International Journal for Numerical Methods in Engineering*, 75(11):1301–1319, Sep 2008.

[81] M. Tamura. Spatial Fourier transform method of measuring reflection coefficients at oblique incidence. I: Theory and numerical examples. *Journal of the Acoustical Society of America*, 88(5):2259–2264, 1990.

[82] M. Tamura, Jean F. Allard, and D. Lafarge. Spatial Fourier-transform method for measuring reflection coefficients at oblique incidence. II. Experimental results. *Journal of the Acoustical Society of America*, 97(4):2255–2262, 1995.

[83] G. Tufano. *K-space analysis of complex large-scale periodic structures.* PhD thesis, Ecole Centrale Lyon & KU Leuven, 2020.

[84] G. Tufano, C. Droz, M. Ichchou, O. Bareille, A. M. Zine, W. Desmet, and B. Pluymers. On the structural characterization through K-space methods: Assessments and validations. *9th ECCOMAS Thematic Conference on Smart Structures and Materials, SMART 2019*, pages 1136–1145, 2019.

[85] G. Tufano, C. Droz, M. Ichchou, O. Bareille, A. M. Zine, W. Desmet, and B. Pluymers. On the structural characterization through k-space methods: Assessments and validations. *9th ECCOMAS Thematic Conference on Smart Structures and Materials, SMART 2019*, pages 1136–1145, 2019.

[86] G. Tufano, F. Errico, O. Robin, C. Droz, M. Ichchou, B. Pluymers, W. Desmet, and N. Atalla. K-space analysis of complex large-scale meta-structures using the Inhomogeneous Wave Correlation method. *Mechanical Systems and Signal Processing*, 135:106407, 2020.

[87] L. Van Belle, C. Claeys, E. Deckers, and W. Desmet. On the impact of damping on the dispersion curves of a locally resonant metamaterial: Modelling and experimental validation. *Journal of Sound and Vibration*, 409:1–23, 2017.

[88] B. Van Damme and A. Zemp. Measuring dispersion curves for bending waves in beams: A comparison of spatial fourier transform and inhomogeneous wave correlation. *Acta Acustica united with Acustica*, 104(2):228–234, 2018.

[89] K. Viverge, C. Boutin, and F. Sallet. Model of highly contrasted plates versus experiments on laminated glass. *International Journal of Solids and Structures*, 102-103:238–258, 2016.

[90] T. Wassereau, F. Ablitzer, C. Pézerat, and Jean Louis Guyader. Experimental identification of flexural and shear complex moduli by inverting the Timoshenko beam problem. *Journal of Sound and Vibration*, 399:86–103, 2017.

[91] K. Watanabe. *Green's Functions for Beam and Plate*, pages 93–106. Springer International Publishing, Cham, 2014.

[92] E. Zhang, J.D. Chazot, J. Antoni, and M. Hamdi. Bayesian characterization of young's modulus of viscoelastic materials in laminated structures. *Journal of Sound and Vibration*, 332(16):3654–3666, 2013.